ANTARCTIC CIRCUMPOLAR CURRENT SYSTEM AND ITS RESPONSE TO ATMOSPHERIC VARIABILITY

A Dissertation

by

YONG SUN KIM

Submitted to the Office of Graduate Studies of
Texas A&M University
in partial fulfillment of the requirements for the degree of

DOCTOR OF PHILOSOPHY

Approved by:

Chair of Committee,	Alejandro H. Orsi
Committee Members,	Achim Stössel
	Shari Yvon-Lewis
	Kenneth P. Bowman
Head of Department,	Piers Chapman

December 2012

Major Subject: Oceanography

ABSTRACT

The Antarctic Circumpolar Current (ACC) is well known for its multiple bands with large meridional property gradients in the upper waters, each associated with a deep-reaching current core. A revised nineteen-year time series (1992−2011) of altimeter data from the CNES/CLS AVISO is analyzed to identify and trace the spatial distribution of ACC fronts. Specific contours of sea surface height (SSH) are selected within narrow continuous bands of relative maxima SSH slope in the Southwest Atlantic Ocean sector, where they closely follow the distribution of ACC fronts derived from inspection of concurrent high-resolution profile data at hydrographic stations. When applied to the full circumpolar belt, the frontal distribution derived from these new altimeter-based indicators also agrees well with the traces of current jets and in-situ dynamic height fields calculated from concurrent Argo profile data.

The temporal variability of ACC fronts is analyzed in relation to dominant modes of atmospheric forcing variability in the Southern Ocean. All three ACC fronts have experienced large seasonal to decadal variability throughout the satellite altimetry era. The general seasonal tendency for each of these jets, with respect to long-term mean positions, is to be located farther to the south during the austral summer and to north in the winter. Circumpolar-mean annual frontal locations show a consistent linear trend of southward migration. However, the estimated decadal variability of the frontal distributions is highly localized, and due to selective response mechanisms to atmospheric variability. A persistent poleward drift of ACC fronts is observed in the

Indian sector consistent with increasing sea surface temperature trends. In contrast, a vacillation in the meridional location of ACC fronts is observed in the Pacific sector in association to minor sea surface cooling trends. Therefore, unlike in the Indian sector, the regional Pacific Ocean response is significantly sensitive to dominant atmospheric forcing indices.

Mesoscale eddies derived from instabilities at strong current cores are successfully identified with specific SSH gradient criteria. The new estimates of rings population in the Southern Ocean are tightly linked to interannual to decadal atmospheric variability. Increased number of mesoscale eddies correlate with positive SAM forcing about two years earlier, or negative ENSO forcing two to three months earlier. These cross-correlations might explain a prominent peak in rings abundance estimated during 2000 and 2001, and the short-lived maximum that appeared in 2010.

There are no persistent trends in the estimated sea surface slope across Drake Passage, and therefore neither in the transport of the ACC. High cross-correlation between the abundance of mesoscale eddies and atmospheric forcing suggests that the overall ACC system is in an eddy-saturated state. However, Drake Passage positive sea level slope anomalies were two-year lagged with negative SAM forcing and with positive ENSO events. These regional responses are characteristic of eastward-propagating signals from a buoyancy-dominated Pacific sector of the Southern Ocean.

DEDICATION

In honor of the love of my life, my inspiration, and my best friend, Suyoun

ACKNOWLEDGEMENTS

Dr. Alejandro H. Orsi, my advisor, has been a source of strength and encouragement throughout this whole process, and I would like to thank him, especially for his financial support and kind advise in the work presented here. I would not have been able to complete graduate school without his cordial support. I would like to thank other committee members: Dr. Achim Stössel, Dr. Shari Yvon-Lewis, and also Dr. Kenneth P. Bowman for taking the time and giving novel advice to make this Dissertation what it is. Friends around the 6th floor (Chrissy Wiederwohl, Benjamin Morgan, Kelly Cole, Who Myung Kim, and Dr. Chan Joo Jang) have also been a blessing beyond measure.

Personally, I would like to thank to my parents for their love and my little treasures Lydia and Joshua for their being. Moreover, my wife Suyoun, who has been incredibly patient and loving in all of the struggles associated with completing this dissertation, has been my inspiration, and therefore I dedicate this work to her. Above all, I give glory and honor to God and Jesus Christ, who daily give me strength and blessing in life.

NOMENCLATURE

AABW	Antarctic Bottom Water
AAIW	Antarctic Intermediate Water
AASW	Antarctic Surface Water
ACC	Antarctic Circumpolar Current
ADT	Absolute Dynamic Topography
ARC	Agulhas Return Current
ASC	Antarctic Slope Current
AVHRR	Advanced Very High Resolution Radiometer
AZ	Antarctic Zone
BEST	Bivariate ENSO Time Series
Bdy	Southern Boundary of the ACC
BMC	Brazil and Malvinas Confluence
BZ	Boundary Zone
EKE	Eddy Kinetic Energy
ENSO	El Niño-Southern Oscillation
EOF	Empirical Orthogonal Function
FFT	Fast-Fourier Transformation
KE	Kinetic Energy
KP	Kerguelen Plateau
MEB	Maurice Ewing Bank

MDT	Mean Dynamic Topography
MOC	Meridional Overturning Circulation
MSLA	Mean Sea Level Anomaly
PF	Polar Front
PFZ	Polar Frontal Zone
SAF	Subantarctic Front
SAZ	Subantarctic Zone
SAM	Southern Annular Mode
SAMW	Subantarctic Mode Water
SASW	Subantarctic Surface Water
sACCf	Southern ACC Front
SFZ	Shackleton Fracture Zone
SGI	South Georgia Island
SODB	Southern Ocean database
SOI	Southern Oscillation Index
SPZ	Subpolar Zone
SSA	South Scotia Arc
SSH	Sea Surface Height
SSHa	Sea Surface Height Anomaly
SSS	Sea Surface Salinity
SST	Sea Surface Temperature
SSTa	Sea Surface Temperature Anomaly

SSL	Sea Surface Level
STF	Subtropical Front
UCDW	Upper Circumpolar Deep Water
WOCE	World Ocean Circulation Experiment
WBC	Western Boundary Currents

TABLE OF CONTENTS

Page

Page

LIST OF FIGURES

Page

Page

Page

Page

Page

LIST OF TABLES

Page

CHAPTER I

INTRODUCTION

1.1 Antarctic Circumpolar Current System

The Antarctic Circumpolar Current (ACC) is primarily driven by predominant westerly winds and is able to encircle Antarctica unconstrained by continents, therefore its flow represents an efficient zonal channel for seawater property. The ACC also rapidly conveys regional climate signals to the adjacent ocean basins to the north. The prominent downward tilt of isopycnal surfaces within the ACC facilitates the transfer of high latitude surface signals to mid-depths of low latitude regimes. In this sense, the ACC system constitutes a key component of the global Meridional Overturning Circulation (MOC) [*Sloyan and Rintoul*, 2001; *Toggweiler and Russell*, 2008].

Upper waters carried eastward by the ACC are separated from relatively warmer subtropical regime waters by the Subtropical Front (STF) and from relatively colder subpolar regime waters by the Southern Boundary of the ACC (Bdy). The ACC consists of three circumpolar jets [*Orsi et al.,* 1995], from north to south: the Subantarctic Front (SAF), Polar Front (PF), and southern ACC front (sACCf). Each of the ACC fronts separates narrow bands of relatively uniform water masses, and therefore the spatial distribution of the fronts correspond to sharp meridional gradients of water properties and steep isopycnals [*Deacon*, 1937; *Nowlin and Clifford*, 1982; *Orsi et al*., 1995; *Belkin and Gordon*, 1996; *Cunningham et al., 2003*]. In turn, this leads to jet-like deep-reaching geostrophic current cores and large volume transport: 134 Sv (1 Sv = 10^6 m^3s^{-1})

are carried by the ACC through Drake Passage, and mainly by the SAF (53 ± 10 Sv) and the PF (57.5 ± 5.7 Sv) [*Cunningham et al., 2003*].

Frontal paths are mainly steered by prominent features in the ocean floor, in some places causing sharp meridional fluctuations to conserve potential vorticity [*McCartney,* 1976; *Gille*, 1994; *Dong et al*., 2006; *Sallée et al.,* 2008], and they are also seemingly fixed along large-scale topographic features such as ridges, plateaus, and fracture zones. However, recent studies [*Sokolov and Rintoul*, 2002, 2009a, 2009b; *Dong et al*, 2006; *Sallée et al*., 2008; *Swart et al*., 2010] have suggested that more intricate spatial distributions owing to selectively interact with the underlying topography: robust and persistent fronts are commonly observed over steep topography, whereas splitting of fronts into multiple filaments and substantial fluctuations are more evident over abyssal plains. Over such plains, ACC fronts have undergone significant variability at a range of time scales, from less than three months to longer than a decadal [*Sallée et al.,* 2008; *Thompson et al.,* 2011]. Mechanism explaining these intricate frontal interactions and temporal variability are still unclear [*Sokolov and Rintoul,* 2009b]. Teleconnection of tropical buoyancy forcing like ENSO to the Southern Ocean [*L'Heureux and Thompson,* 2006; *Fogt et al.*, 2011; *Ding et al.*, 2012] makes understanding the observed variability of the ACC system even more difficult.

Small changes in the meridional location of ACC fronts not only directly have an impact on the net heat flux across the sea surface, but also indirectly affect the northward export of ventilated surface waters with Antarctic origin, feeding both the deep and bottom waters of the world ocean [*Meredith et al.*, 2008; *Gordon et al.*, 2011]. E.g.,

compared to its climatological position [*Orsi et al.*, *1995*], fieldwork conducted in the austral summer of 2009 revealed a prominent poleward (2° of latitude) deflection of the sACCf path just east of the Shackleton Fracture Zone (Figure 1.1). Similar southward migration of the Bdy was observed in the eastern Scotia Sea in response to low atmospheric pressure anomalies over the Weddell Sea [*Meredith et al*., 2008]. Steeper tilt of isopycnals within the Weddell Sea could prevent the coldest and densest outflows of Weddell Sea Deep Water (WSDW), but at the same time favor the overflow of lighter waters over the South Scotia Ridge [*Meredith et al.*, 2008; *Gordon et al.*, 2010]. Oceanic responses to atmospheric variability like these affect the characteristics of bottom waters exported northward along deep western Boundary Currents in the Southern Hemisphere.

By suppressing lateral (isopycnal) mixing in the top kilometer of the water column, the existence of a well-organized series of narrow and sharp density gradients around Antarctica acts as a dynamic bumper between the subtropical and subpolar gyres [*Bower et al.,* 1985*; Garabato et al.,* 2011]. Mesoscale eddies, however, play an important role in meridional exchange of waters across the ACC. A frontal path deflected over rough topography tends to become unstable and to generate intensive rings on its wake. The turbulent flow regime downstream of where ACC fronts interact with mayor topographic features constitutes an effective oceanic conduit for rings to cross from one climate region to another, thus carrying out significant meridional property transports.

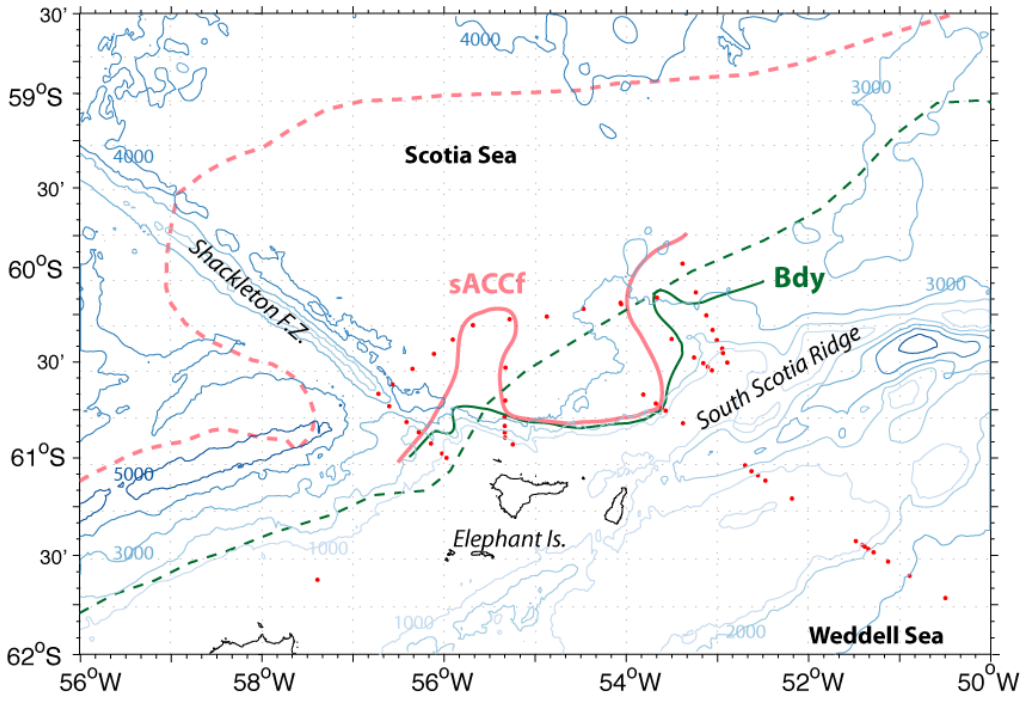

Figure 1.1. Observed frontal shift during the austral summer of 2009. Colored strait lines show the paths of the southern ACC front (red) and boundary (green) during the Antarctic Cross-Road Of Slope Streams (ACROSS) cruise in February−March 2009 (red dots), whereas the climatological frontal paths in *Orsi et al.* [1995] are shown as dashed lines.

1.2 General Background

1.2.1 Mapping of ACC fronts

After *Deacon* [1937] tracked the northern limit of ACC waters by noticing a band (his Subtropical Convergence) enhanced surface temperature and salinity gradients, studies of ACC frontal distribution and their relationships to upper water masses followed more naturally based on modern hydrographic data [*Nowlin and Clifford,* 1982*; Orsi et al.,* 1995*; Peterson and Whitworth,* 1989*; Trathan et al.,* 2000*; Garabato et al.,*

2002*; Sokolov and Rintoul,* 2002*; Sprintall,* 2003*; Garabato et al.,* 2009]. For the first time, *Orsi et al.* [1995] mapped three continuous deep fronts within the domain of circumpolar streamlines, and provided a series of specific property indicators of each of them. Note, however, that their climatological frontal distribution were based on a limited number of sections with coarsely spaced summer stations, and thus with a seasonal biased from the source historical hydrographic data. Drake Passage is the location of the Southern Ocean with the most heavily repeated transects of high-density Acoustic Doppler Current Profilers (ADCP) and Expandable Bathy Thermograph (XBT) data. By using these observed data, but *Lenn et al*. [2007] still found that subsurface criteria given in *Orsi et al.* [1995] are in general in accordance with the location of current jets.

Following *Orsi et al.* [1995], the canonical location of the SAF is marked by the rapid diving of cold, fresh Antarctic Surface Water (AASW) to the north, feeding the salinity minimum layer of the Antarctic Intermediate Water (AAIW). In certain areas just north of the SAF winter subduction of Subantarctic Surface Water (SASW) forms Subantarctic Mode Water (SAMW), which is characterized by oxygen maximum and potential vorticity minimum cores right above the AAIW. The steep plunge of surface properties to depths greater than 400 m is a robust indicator of the SAF. The PF is frequently identified as the northern limit to a subsurface tongue of temperature minimum from the AASW; specifically the PF location is indicated by the trace of the 2°C isotherm at 200 m. While the SAF and PF separate distinct surface water masses, the sACCf is indicated by a narrow property gradient at relatively deep levels. It is

generally associated with the southernmost extension of the 1.8 °C isotherm along the deep temperature maximum of Upper Circumpolar Deep Water (UCDW). The transitional band where the shoaling UCDW oxygen minimum signal crosses 200 m and enters the much colder, well-mixed and ventilated surface waters of the Subpolar regime, is used to mark the location of the southern Bdy. Although sometime found adjacent to or even merged with the sACCf, the Bdy is not a current core with enhanced kinetic energy nor a peak in the sea surface height gradient. In some places the southern Bdy of the ACC is located very close to the continental margins and within a narrow band of sluggish flow, with the strong westward-flowing Antarctic Slope Current (ASC) immediately to the south.

To overcome the spatial and temporal restrictions inherent to in-situ hydrographic data, remotely sensed sea surface temperature (SST) [*Moore et al.*, 1999; *Dong et al.*, 2006], chlorophyll [*Sokolov and Rintoul*, 2007b], and height (SSH) [*Gille* 1994, *Sallée et al.*, 2008; *Sokolov and Rintoul*, 2002; 2007a; 2009a; 2009b; *Swart et al.*, 2008b; *Billany et al.*, 2010] are used to trace bands with enhanced property gradients associated to particular ACC fronts, e.g. a maximum SST gradient tracks the PF location [*Moore et al.*, 1997; 1999*; Dong et al*., 2006]. However, these remote sensing based methods do not resolve the characteristic subsurface property gradients of the PF, normally located farther to the south of their surface expression, and much larger discrepancies are found over the vast abyssal plains [*Dong et al.*, 2006]. From the analysis of satellite data it is also technically difficult to distinguish ACC fronts from the mesoscale rings frequently generated from their interaction with bottom topography.

Studies of altimeter SSH data have found that ACC fronts are tightly aligned with a nearly consistent set of SSH values, even though exhibiting complex temporal and spatial variability. In general, their results agree well with the climatological frontal distributions from *Orsi et al.* [1995]. In their global synthesis of fifteen years of SSH gradients, *Sokolov and Rintoul* [2009a] identified nine filaments to represent the ACC, and reported that detecting the Bdy is not feasible due to relatively low kinetic energy and large errors in SSH data near the Antarctic margins [*Sura and Gille*, 2010].

Sallée et al. [2008] used SSH and available hydrographic data, including Argo and the World Ocean Circulation Experiment (WOCE) Southern Ocean database (SODB), to track the SAF and PF. However, not derived was the mean path of the SAF as it turns sharply to the northward and forms the Brazil-Falkland Confluence Zone, presumably due to increased statistical error, and therefore excluded the western South Atlantic in assessing frontal responses to atmospheric forcing variability.

1.2.2 Oceanic variability due to atmospheric forcing

The ACC system exhibits significant long-term trends and interannual fluctuations in its volume transport, mesoscale eddy field, and meridional distribution of fronts [*Cunningham et al.,* 2003*; Hogg and Blundell,* 2006*; Böning et al.,* 2008*; Gille,* 2008*; Sprintall,* 2008*; Sallée et al.,* 2008*; Swart et al.,* 2008b*; Sokolov and Rintoul,* 2009b; *Billany et al.,* 2010]. These oceanic changes have been explained in relation to the two most dominant climate modes of atmospheric variability: changes in the symmetric global winds system, known as Southern Annular Mode (SAM) [*Thompson*

and Wallace, 2000; *Marshall et al.*, 2009], and in the Pacific sector perturbations of sea-level pressure, temperature, and sea ice remotely triggered by the El Niño-Southern Oscillation (ENSO) [*Smith and Sardeshmukh,* 2000].

a. Wind-driven variability

A positive SAM index anomaly indicates that the southern subpolar westerly winds intensify and contract toward the pole relative to their long-term mean position. The characteristic changes in atmospheric and oceanic circulation during positive SAM are displayed in Figure 1.2. The most noticeable change is enhanced meridional temperature gradients both in the atmosphere and within the ocean interior. Among the expected changes in an ACC system due to the gradient are more vigorous currents due to increased wind energy input and a concurrent poleward drift in all frontal positions. Such direct oceanic responses are supported by simulations from numerical climate models [*Hall and Visbeck,* 2002*; Sen Gupta and England,* 2006] and Drake Passage transport estimates from direct subsurface pressure measurements [*Meredith et al.,* 2004]. Overall they imply that the Southern Ocean is a buoyancy-dominated regime, and that ACC transport is linearly related to wind stress.

Simulations from eddy-resolving models [*Hallberg and Gnanadesikan*, 2006; *Meredith and Hogg,* 2006*; Hogg et al.,* 2008*; Screen et al.,* 2009; *Farneti and Delworth* 2010] and eddy kinetic energy (EKE) fields derived from satellite altimetry data [*Morrow et al.,* 2010] conclude that mesoscale rings, as a delayed response, release the additional momentum from changing winds. They showed a peak in EKE about two-

three years after a positive peak in the SAM index, with minimal change in transport and frontal locations, implying that the Southern Ocean is an eddy-saturated regime.

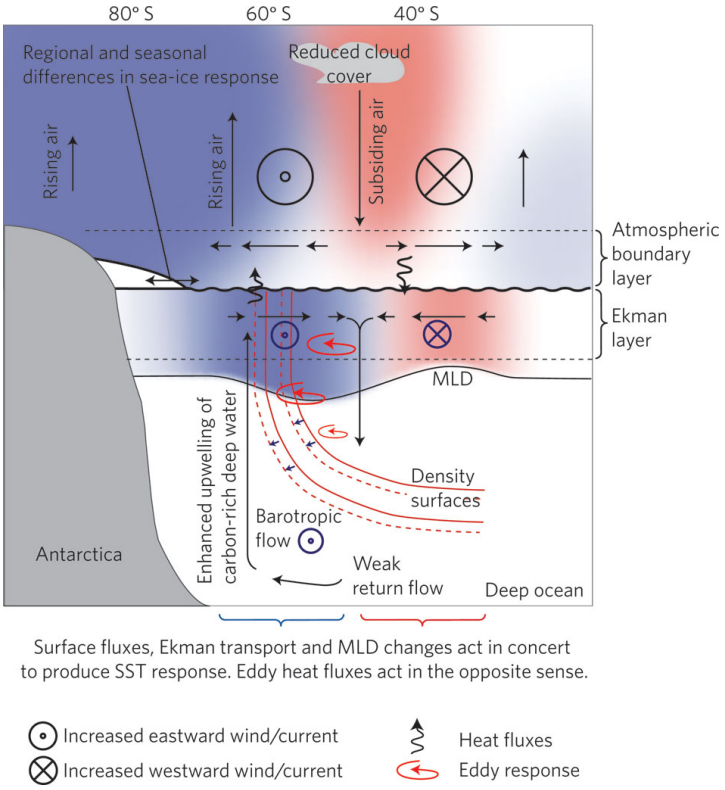

Figure 1.2. Schematic atmospheric changes and oceanic responses during positive Southern Annular Mode months from *Thompson et al.* [2011]. Red (blue) shading indicates warming (cooling). Solid arrows mean meridional or vertical motions.

Temporal variability in ACC frontal locations has been explained by two conflicting arguments, i.e. by overall symmetric poleward drifts, and by regional asymmetric responses to intensified westerly winds. *Sokolov and Rintoul* [2009b] estimated that the mean position of all the ACC fronts experienced a concurrent poleward migration of about 60 km, consistent with the pronounced hemispheric

warming and freshening of waters at surface to mid-depth levels since the 1950s [*Aoki et al.,* 2003; *Gille,* 2008]. Based on reconstructed hydrographic data fields, *Böning et al*. [2008] determined a significant warming and freshening at 800 m – 1,000 m within the Polar Front Zone (PFZ), which they attributed to the ~50 m subsidence of isopycnals induced by the ~50 km–80 km poleward shift of the SAF and PF.

In contrast, *Sallée et al*. [2008] revealed an asymmetric frontal response to the same symmetric variability in the wind systems, especially for a high frequency domain (less than three months). During positive SAM anomalies, even though a poleward frontal migration is also shown in the Indian-Atlantic sector, an opposite equatorward migration was found in the central Pacific, and a stationary scenario (no apparent response) was apparent in the area between the Indian and Pacific sectors. They explained this asymmetric oceanic response by means of the Ekman transport induced by the wind anomalies. According to the Ekman theory, as depicted in Figure 1.2, stronger westerlies (i.e. during +SAM) generate an anomalously large northward Ekman transport sustained by enhanced upwelling at high latitudes, which results in the further uplifting of isopycnals and a negative sea level anomaly (SLA). At low latitudes, an intensified Ekman convergence causes anomalous downwelling, further deepening of isopycnals and elevating sea level. Along their paths around Antarctica, ACC streamlines are subject to different Ekman regimes. On their transit through the Pacific (Indian−Atlantic) sector, where northward (southward) Ekman transport is predominant, a northward (southward) migration of the ACC may result. However, relatively low correlations between the SAM index and the inferred frontal positions [*Sokolov and*

Rintoul, 2009b*; Boehme et al.,* 2008], as well as the unresolved higher frequency responses (with periods shorter than three months), indicate a more hardwired frontal response to changes in wind types.

b. ENSO-driven variability

ENSO is a tropical phenomenon due to ocean-atmospheric interactions with a main frequency of two to seven years. ENSO signals are transferred to the Southern Ocean by Rossby wave-trains. They trigger a positive SLP anomaly (+SLPa) over the southwest Pacific during an El Niño period (+ ENSO) [*Turner,* 2004]. Winds rotating around the +SLPa enter bring relatively warm (cold) air from low (high) latitudes toward the area west (east) of the anomaly center. Warmer (colder) air enhances (decreases) the heat flux across the sea surface, and results in a +SSTa (−SSTa) and a sea-ice retreat (advance) in the Pacific (Atlantic) sector [*Kwok and Comiso,* 2002] of the Southern Ocean. The out-of-phase relationship in sea ice extent and SST between the Pacific and Atlantic sectors has been termed the Antarctic Dipole [*Yuan,* 2004]. These localized ENSO signals travel within the ACC domain and seem to dissipate after two to three years [*Verdy et al.*, 2006].

The ENSO index quantifies the strength of ENSO events, and has experienced substantial variability on interannual-to-decadal time scales. Between the 1920s and 1960s, there were very few El Niño and La Niña events, except for a strong El Niño event between 1939 and 1941. Since 1960 the ENSO index shows a tendency toward

more frequent and stronger events, and consequently similar changes in the frequency and amplitude of the Antarctic Dipole.

Sallée et al. [2008] indicate that low frequency variability in frontal positions has a much higher correlation with the ENSO index than with the SAM index. This is particularly true in the Pacific sector of the Southern Ocean, where the ENSO response appears to be strongest.

1.3 Overview

This study investigates how the ACC system responds to atmospheric variability by looking at changes in the SST, SSH, frontal distributions, and mesoscale eddy fields. Data analyzed to address these questions are described in Chapter 2. Characteristics of two main climate modes of atmospheric variability, and the SST responses are described in Chapter 3. Chapter 4 introduces practical SSH indicators for the location of ACC fronts, validated against traditional water property indicators using concurrent high-resolution in-situ hydrographic and Argo profile data. The empirical relationship between variability in the ACC fronts and streamlines distribution derived from the analysis of altimetry data are also investigated. A new climatological frontal path, inferred spatial and temporal variability are discussed in Chapter 5. Chapter 6 describes the role of atmospheric variability on the observed frontal fluctuations, the spatial distribution and temporal evolution of mesoscale rings, and their responses to atmospheric change. A summary of concluding remarks presented in Chapter 7.

CHAPTER II

DATA AND METHOD

2.1 Test Area

ACC streamlines extend continuously around Antarctica but upon entering the Atlantic through Drake Passage, a chokepoint only about 7° of latitude wide (Figure 2.1), the Current's hydrographic structure is squeezed and leads to intense frontal jets. The paths are then more spread out in the south Atlantic, but still showing high topographic control. Classic definitions of ACC fronts were based on water properties criteria first developed at Drake Passage [*Nowlin and Clifford,* 1982], and recently supported by current cores detected using subsurface current observations [*Lenn et al.,* 2008]. In fact validation of Drake Passage frontal definitions has been confirmed almost everywhere in the Southern Ocean [*Orsi et al.,* 1995]. In this study, I will seek empirical relationship between ACC fronts and sea surface streamlines in the southwest Atlantic area shown in Figure 2.1, and then apply them to the whole Southern Ocean. This study take advantage of the large number of meridional hydrographic sections available in this area to test the accuracy of altimetry data while tracking ACC fronts (Figures 2.3).

Test regions mainly consist of the Argentine Basin and the Scotia Sea, the latter showing several prominent topographic features and significant overall roughness (Figure 2.1). Meridionally aligned ridges, i.e. Shachkleton Fracture Zone (SFZ), West Scotia Ridge (WSR), and South Scotia Arc (SSA), act as obstacles and steer the ACC northward to compensate for its loss of potential vorticity. The zonally aligned

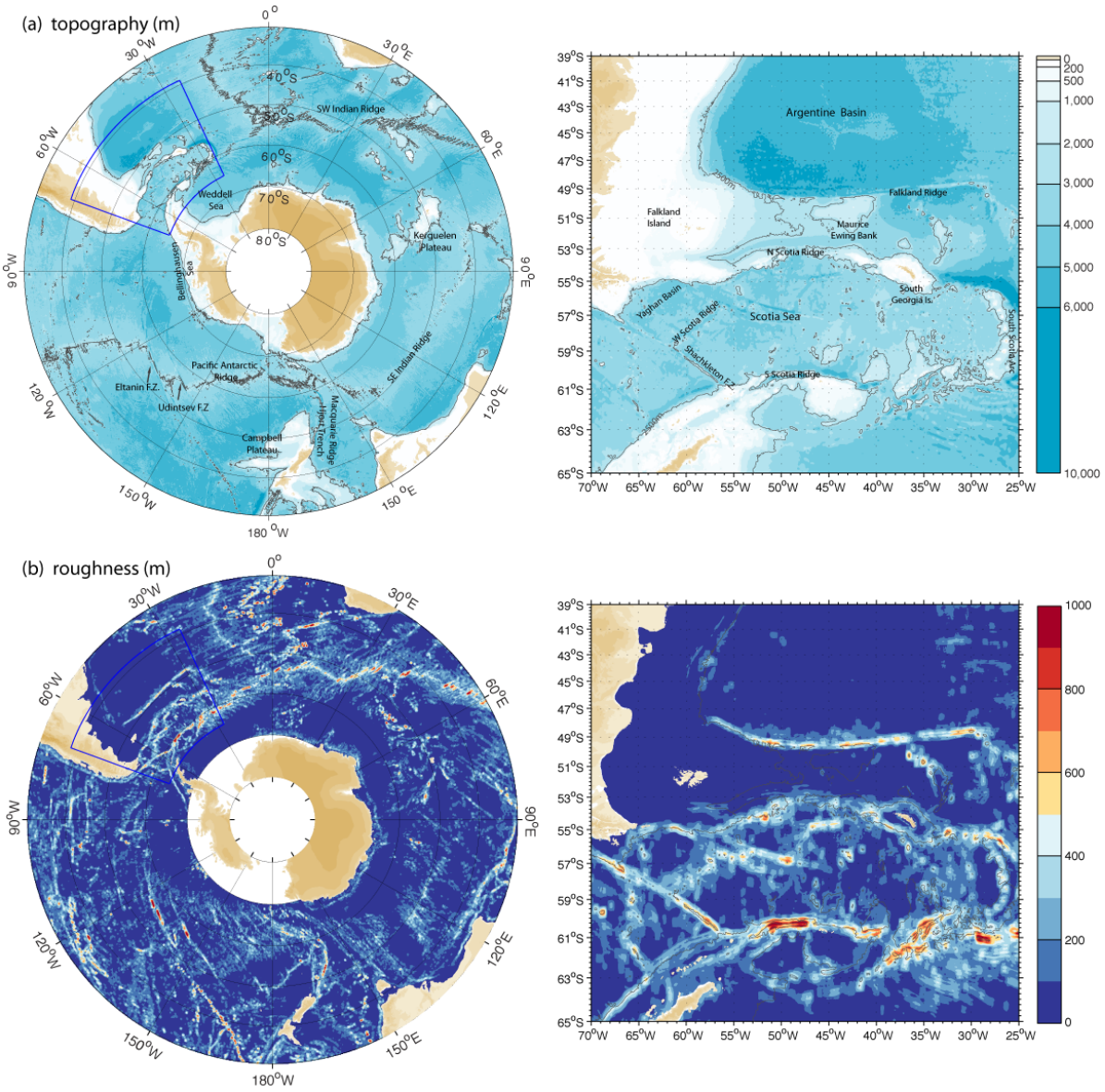

Figure 2.1. (a) Bottom topography (m) and (b) roughness (m) using 1-minute dataset [*Smith and Sandwell,* 1997]. Right panels show the detailed features within the test area (the blue box in the left panel). The thin black line in the upper panel indicates the 2,500 m isobath.

South Scotia Ridge (SSR) prevents newly ventilated deep and bottom waters from getting into the Scotia Sea directly from the Weddell Sea. Maurice Ewing Bank (MEB) and South Georgia Island (SGI) are also important topographic obstacles to ACC streamlines, whose interaction generates frequent mesoscale rings [*Meredith et al.,* 2003*; Thorpe et al.,* 2002]. Also the large-scale and steep continental slope off Argentina effectively constrains the path and reduces the variability of the SAF [*Gordon et al.,* 1978*; Dong et al.,* 2006*; Sallée et al.,* 2008*; Sokolov and Rintoul,* 2009a]. In contrast, the test area south of Australia in *Sokolov and Rintoul* [2003; 2007a] is a rather wide gateway characterized by a relatively flat ocean floor, therefore the weak and multiple current filaments found in that region, as opposed to a robust and persistent frontal structure.

The Argentine Basin is characterized by the confluence of waters carried northward along the SAF and southward by the Brazil Current, and I will investigate the influence of Atlantic tropical waters on the ACC system variability. Contours of SSH are reliable indicators of sea surface streamlines, i.e. water parcels tend to follow the path of specific streamlines unless influenced by different source waters [*Swart et al.,* 2010].

2.2 Data

2.2.1 SSH

Absolute SSH is calculated by adding the Mean Dynamic Topography (MDT) to SLA fields obtained from CNES/CLS AVISO (http://www.aviso.oceanobs.com, [*Ducet*

and Le Traon, 2001]). A weekly time series of SSH between 14 October 1992 and 19 January 2011 was analyzed on a Mercator grid with zonal (meridional) resolution of 1/3° (1/6°, 18.5 km) at the Equator (60°S). There is an up-to-dated (UTD) SLA product produced by merging all available missions from the TOPEX/Poseidon, the European Remote Sensing (ERS) satellite, Geosat, Jason-1, and Environmental Satellite (Envisat) [*AVISO*, 2009]. *Lenn et al.*, [2008] noted that geostrophic current anomalies calculated from the recently revised UTD was more consistent with ADCP observations than the AVISO's previous data set, which significantly underestimates the total variance, and only represents 3*%* of the variability at the wavelengths less than 100 km, which is a characteristic length for mesoscale eddies dominant in this study region. Thus, this study uses the recently revised UTD data sets generated though an upgraded parameterization and editing process, which results in accuracy an improvement in accuracy, particularly along the coastal area [*AVISO*, 2009].

This study takes advantage of recently released MDT_CNES_CLS09 [*Rio et al.,* 2009] from CNES/CLS AVISO for MDT data. This data set was calculated based on 4.5 years of GRACE data combined with fifteen years of altimetry and in-situ data (from hydrographic and Argo floats) relative to a seven-year (1993−1999) mean profile on a ¼° grid resolution. *Sokolov and Rintoul* [2007a] suggested that the location of fronts is insensitive to the choice of climatological MDT maps. However, climatological frontal positions chiefly depend on the MDT field because the long-term average of SLA approaches to zero. Therefore, *Lenn et al*. [2008] emphasized that large discrepancies among climatological paths are likely due to the choice of MDT fields (see their figure

7). According to the thermal wind balance, SST and SSH fields should resemble each other, and the MDT_CNES_CLS09 fields show higher coherence with the mean SST in our study area than MDTs used in the previous studies [*Sallée et al.,* 2008*; Sokolov and Rintoul,* 2009a]. Here, the area-averaged root mean square (RMS) of objective-mapping error in the SLA is 1.84 dyn cm (Figure 2.2b), and most remarkable is just south and north of the ACC. Errors increase up to 5 dyn cm along the Antarctic Peninsula due to inadequate data points for the mapping; and the maximum (8 dyn cm) around the Zapiola Anticyclone is likely the localized complex mesoscale eddy activity. Also, the objective interpolation assuming a Gaussian type of data distribution for the probability distribution function (PDF) is a large source of these error fields [*Sura and Gille*, 2010], since it can wipe out extreme events, e.g. mesoscale eddies near the continental margin, thus, skewing the sea level distribution. However, the overall RMS errors within the ACC are less than 1 dyn cm, i.e. minimal compared to the total surface change of about 110 dyn cm, thus supporting the satellite altimetry use to reliably indicate ACC frontal positions.

2.2.2 CTD profiles

To validate whether a single value of SSH matches a particular ACC front, as identified based on in-situ properties [*Orsi et al.,* 1995], this study examines all the available high-quality hydrographic data during the span of the SSH time series in the study area (Table 1, Figure 2.3). It provides good spatial coverage and consists of 614 CTD stations from 16 cruises by the US, Chile, and the UK extracted from the Southern

Ocean Data Base (available online at http://woceatlas.tamu.edu). Although most cruises were conducted during the austral summer, more than a third of the total CTD stations (DOVETAIL, ALBATROSS, and A23) were from the fall or winter seasons, thus giving us confidence that the observed relationship between SSH and ACC fronts are not seasonally biased.

2.2.3 Argo floats and drifters

In addition to horizontal current maps, a total of 9,912 Argo profiles (Figure 2.3) from February 2002 to May 2010 were investigated (available at http://www.coriolis.eu.org) to study the spatial correspondence in remote sensing

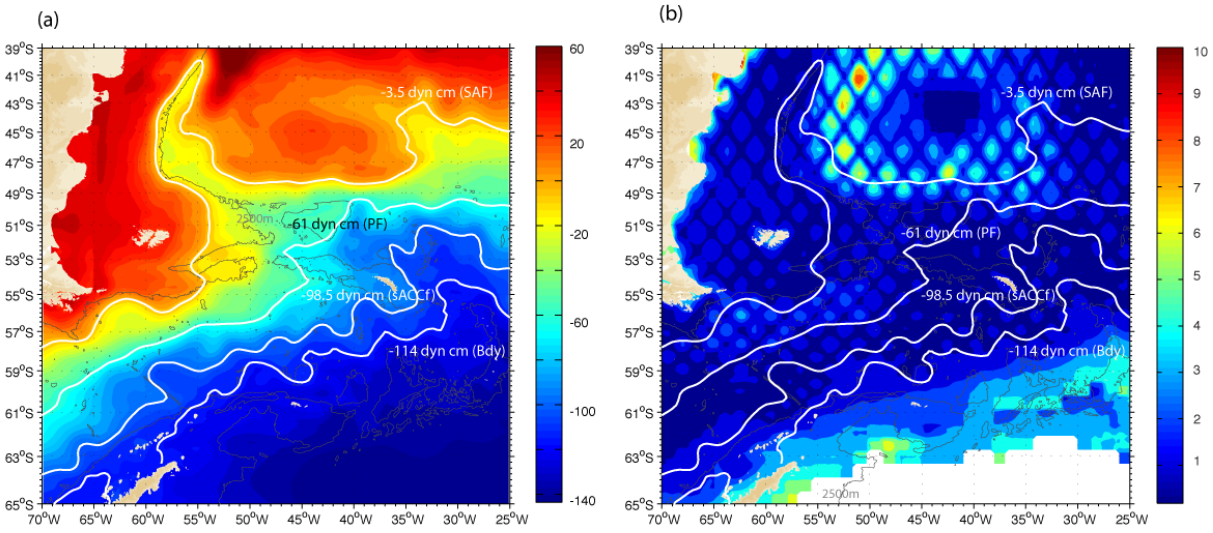

Figure 2.2. (a) The time-averaged map of absolute dynamic topography (dyn cm) and (b) its root mean square errors (dyn cm). The overlaid white lines are the −3.5, −61, −98.5, and −114 dyn cm SSH contours, which represent the SAF, PF, sACCf, and Bdy respectively in this study (see text).

Table 1. Summary of the Cruises Used in This Study

Cruises	Nation	Vessel	Date	# of Stations
A11	UK	Discovery	Dec. 1992 – Feb. 1993	41
SR1a 1993	Chile	Vidal Gormaz	Nov. 1993	17
SR1b 1993	UK	James Clark Ross	Nov.1993	30
SR1a 1994	Chile	Vidal Gormaz	Nov. 1994	18
SR1b 1994	UK	James Clark Ross	Nov. 1994	28
A23	UK	James Clark Ross	Mar. – May 1995	50
SR1a 1995	Chile	Vidal Gormaz	Dec. 1995	17
SR1b 1996	UK	James Clark Ross	Nov. 1996	29
SR1a 1996	Chile	Vidal Gormaz	Nov. – Dec. 1996	15
SR1b 1998	UK	James Clark Ross	Dec. 1997– Jan. 1998	38
DOVETAIL	UK	N. B. Palmer	Aug. – Sep. 1997	45
SR1a 1998	Chile	Vidal Gormaz	Dec. 1998	14
ALBATROSS	UK	James Clark Ross	Mar. – Apr. 1999	170
SR1b 2000	UK	James Clark Ross	Feb. 2000	29
SR1b 2002	UK	James Clark Ross	Dec. 2002 – Jan. 2003	30
A16S	USA	Ronald H. Brown	Jan. – Feb. 2005	47

dynamic height and in-situ observations. Argo profiles cover almost the whole area without seasonal bias, thus providing unique in-situ observational information in space and time. Floats normally profile down to 2,000 m every 10.5 days, and drift at a parking level of 1,000 db. Errors in displacement, and hence, in the estimation of deep

current velocity are generally less than 0.5 cm/s [*Park et al.,* 2005], which is one or two orders smaller than the deep ACC currents in this study region (Figures 4.7, 4.8, and 5.1b). This study used profiles deeper than 400 m that passed the Argo real-time quality control. Remaining outliers and spikes were removed by checking the overall data ranges (126 data points; $T \geq 35°C$ and $T \leq -2°C$, $S \geq 37$ and $S \leq 10$, $P \geq 2{,}100$ db), standard deviations (7,621 data points; $\geq 3.5\ \sigma$), and neutral density instabilities (815 data points; $\Delta N < -0.01$ Kg/m^3). A final total of 8,147 Argo profiles were analyzed in this study.

Surface velocity data was derived from 466 satellite-tracked surface drifting buoys drifters (*Grodsky et al.* [2011]; available at http://www.coriolis.eu.org) passing through this region between 2002 and 2011. Drifter geographic position has an accuracy of 0.01° for a fixed time interval ranged between twenty-five minutes to twenty-four hours.

2.2.4 SST

SST data was analyzed to monitor sea surface variability due to atmospheric forcing. The SST data source is an objectively interpolated SST data generated mainly from the AVHRR infrared satellite corrected using available in-situ data, including shipboard observations and buoys, and is available from the National Oceanic and Atmospheric Administration (NOAA) [*Reynolds et al.,* 2007, http://www.ncdc.noaa.gov/oa/climate /research/sst/oi-daily.php]. Daily SST fields have

a spatial grid resolution of ¼° from September of 1981 to the present, thus spanning the SSH data period.

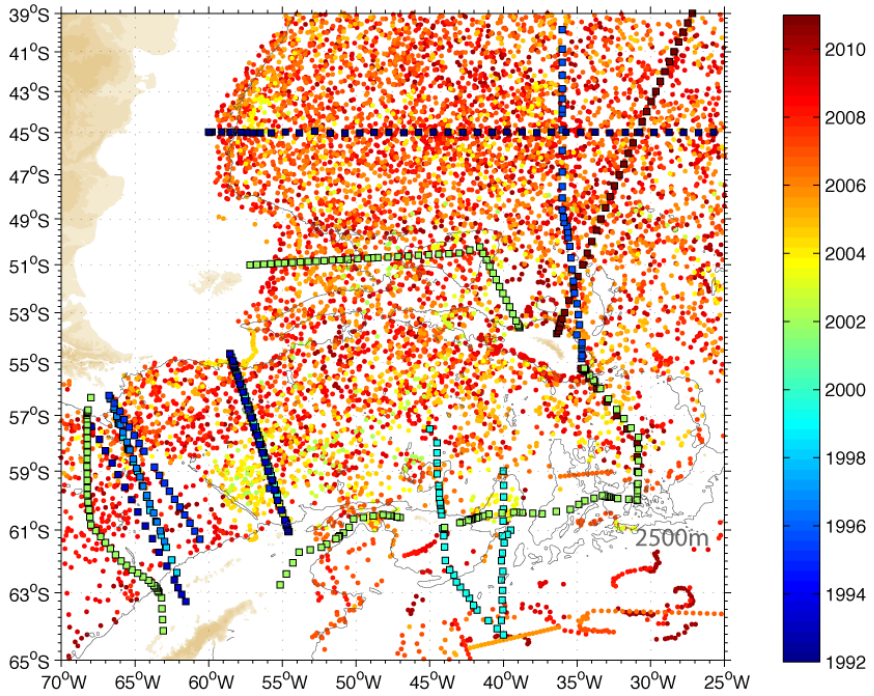

Figure 2.3. Temporal and spatial distribution of the hydrographic profiles. Squares show the location of analyzed a total of 610 CTD stations from 16 hydrographic cruises color-coded by time. Circles show the position of 9,912 profiles of ARGO floats passing through this region since 2002. The thin black lines indicate the 2,500 m isobath.

2.2.5 SAM and ENSO indices

This study analyzes indices of two dominant climate modes of atmospheric variability in the Southern Ocean: the SAM index [*Marshall,* 2003, downloaded from http://www.nerc-bas.ac.uk/icd/gjma/sam.html] and a bivariate ENSO index [*Smith and Sardeshmukh*, 2000; downloaded from

http://www.cdc.noaa.gov/people/cathy.smith/best], whose details are discussed in the next chapter.

2.3 Wavelet Analysis

To investigate the dominant and most consistent frequencies in the source time series, spectral analysis methods such as Fast-Fourier Transformation (FFT) has traditionally been used under the assumption of stationary phenomena. However, the observed geographic data sets often have significant time-dependent frequencies. E.g. a a non-stationary time series like Niño 3 SST [*Torrence and Compo,* 1998] has the most power within the 2−8 year band, but also a reduced power period 1920−1960 between the two enhanced power periods (1985−1920 and 1960−1990). This shows that wavelet spectral analysis is a useful tool in studying dominant frequencies and their time evolution. Time series data in this study are sampled (x_n , $n=1,2,\ldots N$; time index) at equal intervals (δt), e.g. atmospheric indices and frontal variability, and therefore suitable for examination following the practical wavelet analysis guide by *Torrence and Compo* [1998].

This method breaks down a time-series into time-frequency space through a mathematical function called a wavelet, which plays the role of a band pass filter in the time-series. The Morlet wavelet (ψ) is suggested in the Wavelet toolbox developer's manual, to capture general features of geophysical data sets [*Moore et al., 2005*]. ψ is complex, thus the wavelet transform ($W_n(s)$) returns real and imaginary parts as a function of a wavelet scale (s). The wavelet power spectrum is defined by multiplying

the real and imaginary parts of the wavelet transform: the square of the amplitude of the wavelet transform ($\left|W_n(s)\right|^2$). The smallest resolvable scale (s) of the wavelet (2 δt) is used to obtain the finest resolution. In this study, the common shortest temporal interval is a month, so 2 months is the resolvable wavelet scale. In order to reduce edge effects at the beginning and end of the power spectrum, zeros are padded to the data prior to the wavelet transformation, and then are removed after analysis. This technique introduces discontinuities at the start and end points, thus the amplitude near the edge is decreased. The cone of influence (COI) is defined as the region of the wavelet power spectrum where the edge effects are not negligible. Thus, a peak in the wavelet spectrum lying below the COI may be generated artificially due to the zero padding effect.

To examine the statistical significance in the wavelet power spectrum, time series are modeled assuming red-noise using the univariate lag-1 autoregressive process (AR1) $x_n = \alpha x_{n-1} + z_n$, where α is calculated with lag-1 and lag-2 autocorrelations of the data set, and z_n is a random variable from a Gaussian-type white noise. A background power spectrum is transformed with a modeled time-series. The 95% confidence levels are determined by multiplying the background red-noise modeled spectrum by the 95% value for chi-squared. The computed wavelet power spectra are simply averaged over the whole time period and defined as a global power spectrum, $\overline{W}^2(s) = \frac{1}{N}\sum\left|W_n(s)^2\right|$. Thus it can help to discern consistent spectrum peaks.

CHAPTER III

ATMOSPHERIC FORCING AND SEA SURFACE RESPONSE

3.1 Climate Indices

3.1.1 SAM

Changes in the Southern Hemisphere winds have been monitored over time by means of particular indexes. The SAM index indicates their general strength and is often calculated as the meridional difference of normalized mean sea level pressure (SLP) between mid (40°S) and high (65°S) latitudes [*Gong and Wang*, 1999]. Because it is the dominant atmospheric mode of variability, SAM index is also represented by the first principal component (PC) in the EOF of reanalysis SLP data south of 20°S, e.g. NCEP/NCAR and ERA-40 [*Thompson and Wallace,* 2000]. However, quality of reanalysis SLP data was low prior to 1979 and with relatively large errors due to scarcity of in-situ [*Bromwich and Fogt,* 2004]. To represent Southern Ocean wind forcing we adopt the more reliable SAM index in *Marshall* [2003] (Figure 3.1a), which is computed from differences in measured SLP at six station pairs [*Gong and Wang,* 1999] and still captures most of the variability in the PC-based index [*Jones et al.,* 2009].

The monthly SAM index shows high frequency variability, and even though the mean wavelet spectrum (Figure 3.1c) shows statistically significant peaks (>95% confidence level) at periods of six months and one year, there are no continuous bands in the modulus (Figure 3.1b) to indicate that they are not stationary over time. A decadal trend with increasing values from 1964 to 1999 is apparent in the 3-yr filtered time series

(green line of Figure 3.1a), with separate relative peaks in 1962/63 and 1939 (not shown) and also weaker trends [*Jones et al.,* 2009], implying that there is certain natural variability in the winds system [*Jones and Widmann,* 2004*; Arblaster and Meehl,* 2006]. The sharp downward spike in the SAM index in 1964 was associated to the eruption of tropical Mt. Agung in the previous year [*Marshall,* 2003], by decreasing mid-latitude temperature and sea level pressure. In contrast, the recent decadal positive trend (1964−1999) is attributed to an increase in anthropogenic greenhouse gases [*Marshall et al.,* 2004], the ozone depletion over Antarctica [*Thompson and Solomon*, 2002], or a combination of the two.

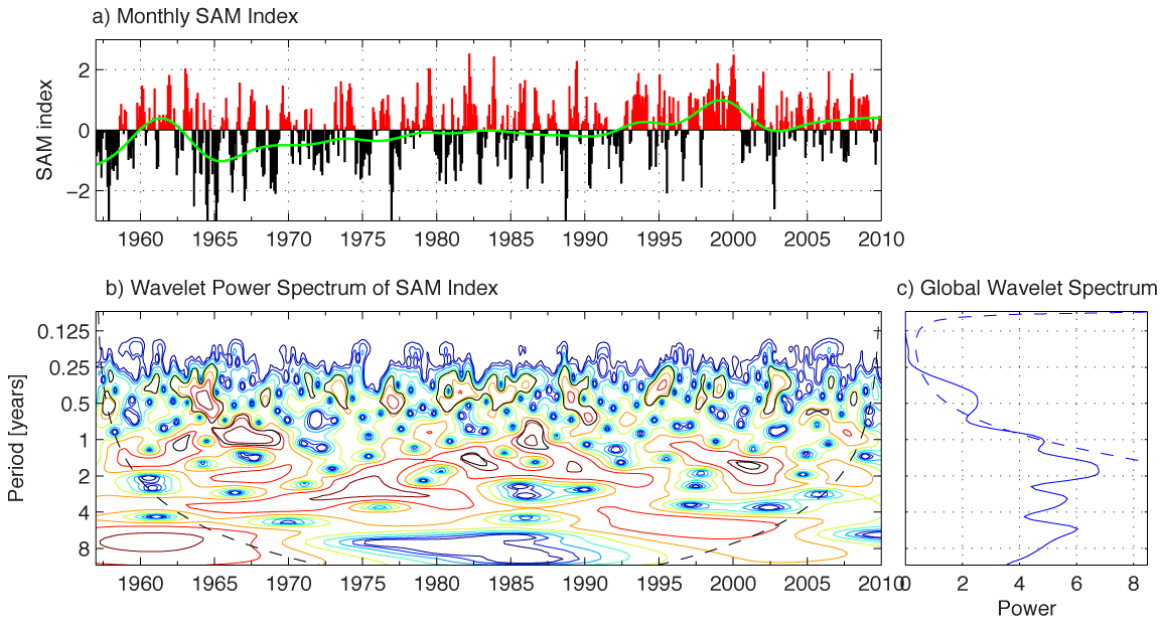

Figure 3.1. (a) Monthly time series with the three-year low-pass filtered curve (green); (b) power spectrum of the wavelet analysis using the Morlet wavelet; and (c) mean power of the global spectrum for the SAM index since 1957. The solid black (b) and dashed blue lines (c) indicate the 95% significance level. The dashed black line in (b) is the cone of influence.

3.1.2 ENSO

ENSO variability has traditionally been estimated based on two independent properties: the Niño 3.4 SST index for the oceanic component and the Southern Oscillation Index (SOI) for the atmospheric component. The Niño 3.4 SST index is calculated using an area-averaged monthly SST over the Niño 3.4 region (120°−170°W, 5°N−5°S), while the SOI index is calculated from the SLP difference between Tahiti and Darwin. Although there is a high coherency between the two indices, they do not fully represent the ocean-air coupled characteristics of the ENSO [*Torrence and Webster,* 1999]. To overcome such limits, *Smith and Sardeshmukh* [2000] introduced a Bivariate ENSO Time series (BEST) index (Figure 3.2a), calculated by averaging the separately standardized SST and SOI time series.

The BEST shows a statistically significant variability in the 2 – 6 year band, with clear peaks at 3.8 years and 5.5 years (Figure 3.2c). Also ENSO events have become more intense, frequent, and prolonged since the 1960s implying enhanced impact on the Southern Ocean in recent decades. Time segments for which relatively high power is estimated at 95% confidence level (within black contours in Figure 3.2b) are those before 1920 and after 1960 [*Torrence and Webster,* 1999], but separated by the low-power 1920−1960 period. This pattern indicates decadal variability in the ENSO, as shown for the Niño3 SST index by *Torrence and Compo* [1998].

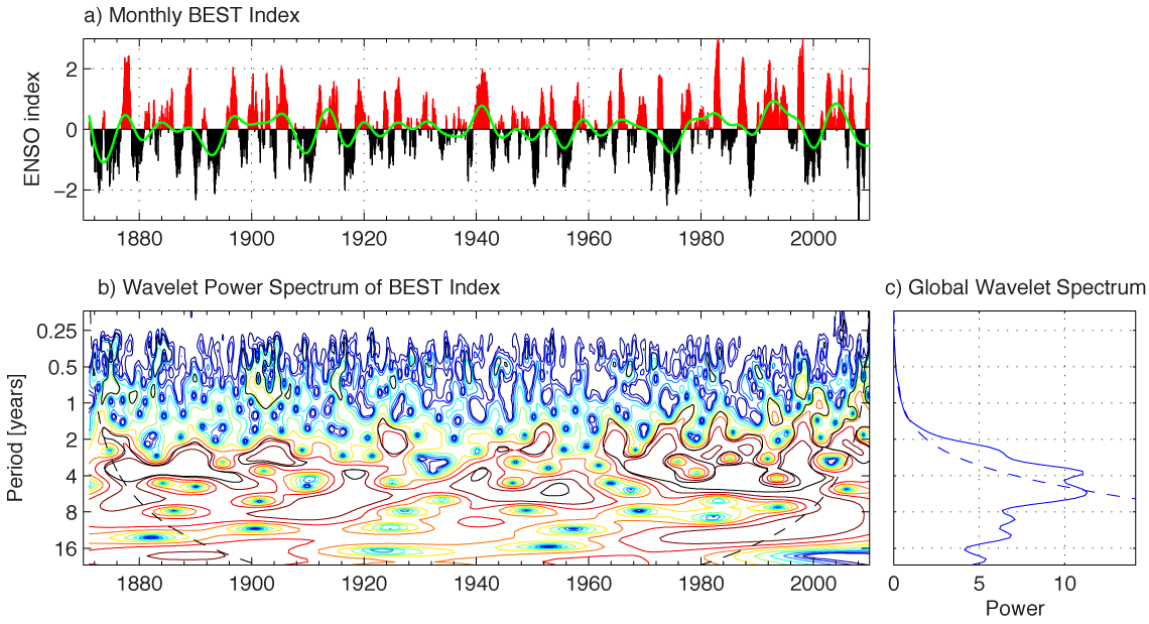

Figure 3.2. Same as Figure 3.1 but for ENSO index since 1871 with a one year low pass filtered line (green).

3.2 Index Interactions

Relatively strong cross-correlation between ENSO and SAM indexes has been reported in recent studies. *L'Heureux and Thompson* [*2006*] found that 25% of SAM variability has a significant linear relationship with fluctuations in the ENSO index, especially during the austral summer. The strong 1999 La Niña (2002 El Niño) was concurrent with the positive (negative) SAM peak during 1998−1999 (2002−2003). Even though the processes represented by the SAM and ENSO indexes are independent, the apparent resemblance in the out-of-phase patterns of SST responses (see Figure 3.5) may imply a cause and effect relationship between the two main modes of atmospheric variability. We explore potential relationships and statistical significance between these two indices by plotting their joint probability distribution ($P(\chi^2)$) in Figure 3.3,

following *Fogt et al.* [2011], and chi-squared values for the observed and expected number of events in a specific region. The expected number is simply calculated with a marginal probability assuming the null distribution, which is reasonable with more than 5 events for each region. E.g. large χ^2 with $P(\chi^2)$ smaller than 0.05 means there are substantial differences between the observed and expected events. Each region is separated by ± 0.5 standard deviation of index values. Events inside of the ± 0.5 of each index imply weak and neutral cases, and an event outside means strong and anomalous cases. In general, Figure 3.3a reproduces well-known features [*Fogt et al.,* 2011*; L'Heureux and Thompson,* 2006*; Fogt and Bromwich,* 2006]. Most notable is a preference for positive SAM events (+SAM) during La Niña, which means that the combination of +SAM/La Niña occurs more times than expected. For this combination, instead of the 53.4 expected events, 65 actually happened over the last fifty years. On the other hand, for both of the −SAM/La Niña and La Niña only combinations there were less observed than expected event.

Fogt et al. [2011] found the highest correlation between atmospheric indices during the austral summer season (December−February, DJF). Although we find a similar summer −SAM preference for El Niño (Figure 3.3b), it is with no statistical significance since our calculated chi-squared probabilities (0.17 for four seasons, 0.15 for the austral summer, and 0.51 for the other three seasons, all since 1957) are much higher than in their study and the threshold for statistical significance (e.g. 0.05). This indicates that any cause and effect relationship between SAM and ENSO would only be weak or with no statistical significance.

ENSO events may influence the SAM index as follows. An ENSO-induced SLP anomaly in the south Pacific may lead to a change in the meridional SLP gradient, which in turn modifies the zonal westerly winds. However, such effect is likely only local in extent, thus not strong enough to induce hemispheric-scale wind anomalies. It is likely that the difference in source index alone, i.e. Nino 3.4 SST rather than BEST, may have limited the ability to represent the atmospheric component of ENSO in *Fogt et al.* [2011].

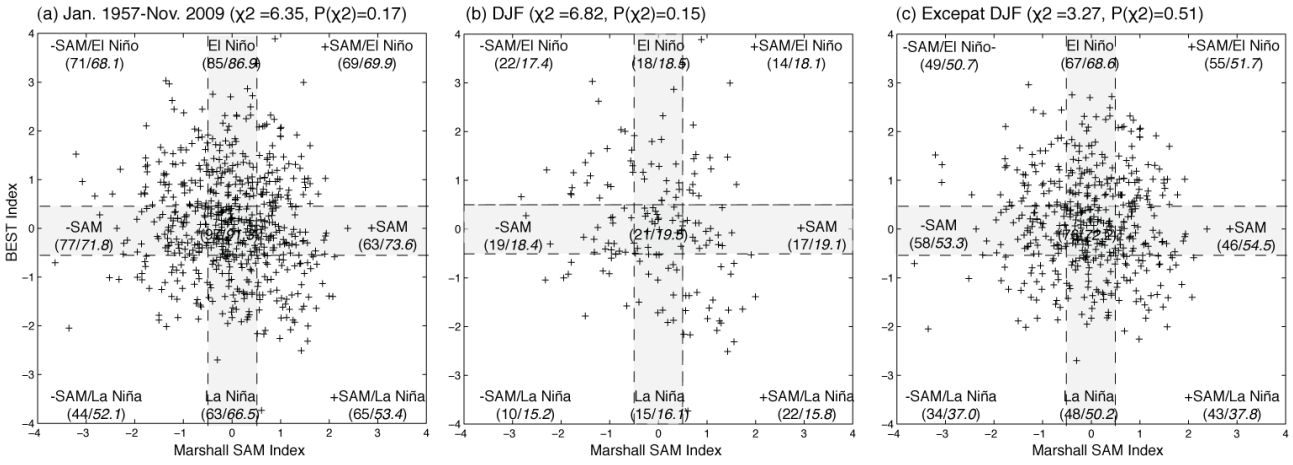

Figure 3.3. The distribution of monthly SAM and ENSO indices (a) during four seasons, (b) the austral winter, and (c) the other seasons since January 1957 with nine distinct regions. The gray shaded region represents ± 0.5 of each index. The first (second italicized) number within brackets is the total number of observed (expected) count of events for each region. The expected numbers of events are calculated based on the marginal probabilities.

Table 2 summarizes the temporal evolution of SAM and ENSO indices. More frequent +SAM anomalies and strong ENSO (either El Niño or La Niña) events are seen after October 1992, whereas at the same time the cases of neutral ENSO and −SAM

Table 2. Number Of Months Based On the Joint ENSO−SAM Distribution Over January 1957−September 1992 And October 1992−November 2009; Each Percentage Within the Brackets Represents a Fraction Of the Total Events For Easy Comparison Between Different Time Periods.

Regions	Definitions	Jan. 1957 – Sep. 1992	Oct. 1992 – Nov. 2009
+SAM	SAM > 0.5	113 (28.3%)	84 (41.0%)
Neutral	|SAM|<0.5	133 (33.3%)	82 (40.0%)
−SAM	SAM < 0.5	153 (38.4%)	39 (19.0%)
El Niño	ENSO >0.5	139 (34.8%)	86 (42.0%)
Neutral	|ENSO|<0.5	152 (38.1%)	55 (26.8%)
La Nina	ENSO <0.5	108 (27.1%)	64 (31.2%)
−SAM/El Niño	ENSO >0.5 SAM<−0.5	53 (13.3%)	18 (8.8%)
El Niño only	ENSO >0.5 |SAM|<0.5	50 (12.5%)	35 (17.1%)
+SAM/El Niño	ENSO>0.5 SAM>0.5	36 (9.0%)	33 (16.1%)
−SAM only	|ENSO|<0.5 SAM<−0.5	65 (16.3%)	12 (5.9%)
Neutral	|ENSO|<0.5 |SAM|<0.5	43 (10.8%)	24 (11.7%)
+SAM only	|ENSO|<0.5 SAM>+0.5	44 (11.0%)	19 (9.3%)
−SAM/La Niña	ENSO<−0.5 SAM<−0.5	35 (8.8%)	9 (4.3%)
La Niña only	ENSO<−0.5 |SAM|<0.5	40 (10.0%)	23 (11.2%)
+SAM/La Niña	ENSO<−0.5 SAM>0.5	33 (8.3%)	32 (15.6%)

have significantly decreased. Consequently, there were also more (less) months with +SAM/+ENSO and **+SAM/−ENSO** (**−SAM/+ENSO**, −SAM/−ENSO, and −SAM only) combinations during the past two decades. Therefore, it is not clear if there is recent

preference for **events with opposite signs** as suggested by *Fogt et al.* [2011], in which case it likely would have happened by chance or biased by the more recent +SAM anomalies due to ozone depletion and anthropogenic warming.

3.3 SST Response

To infer the spatial distribution of the total temperature change at the sea surface in the past three decades, Figure 3.4a shows the overall linear change in SST anomaly (SSTa), after removing both the record-length mean and its seasonal cycle from SST data between 1981 and 2010. It clearly shows that (a) the Subtropical regime (mid-latitudes) has warmed on average by about 0.5°C, at a pace about three times larger than the global mean trend (0.62°C/100yr) in *Wu et al.* [2012], (b) the largest warming of up to 1.5°C is found east of New Zealand, as noted by *Chambers et al.* [1997], (c) there is warming exceeding 1°C at all the subtropical Western Boundary Current (WBC) systems, and (d) the high-latitude band reveals a net cooling trend.

Significant surface warming along WBCs has been inferred from various reconstructed and reanalysis SST products [*Wu et al.*, 2012], but at rates two to three times lower than shown here. Similar to our estimated net warming along the Agulhas System are those reported warming rates (for 0° and 35°E and the past 30−40 years) in recent syntheses of model simulations, satellite and in-situ hydrographic data [*Alory et al.*, 2007; *Biastoch et al.*, 2009; *Rouault et al.*, 2009]. It is likely that the wind system changed in recent decades, causing an intensification of the wind stress curl over the Indian subtropical gyre and a poleward drift of the maximum westerly winds. Such

anomalous wind stress curl pattern would accelerate the Agulhas Current, thus carrying more heat available to leak, in the form of warm core rings, into the South Atlantic and into the ACC. The latter is by eddies shed at the Agulhas Return Current (ARC), so that the warm anomaly signal could reach to as far east as the Kerguelen Plateau (66°E – 70°E), where the distinct core of the ARC has already faded away [*Lutjeharms and Ansorge*, 2001]. Concurrent southward displacement of the zero wind stress curl line [*Biastoch et al.*, 2009; *Beal et al.*, 2011] is the effective expansion of an Agulhas Retroflection and ARC more prone to leak warm Indian waters. In turn, such induced warming of the South Atlantic interior intensifies the Brazil Current, and eventually the entire Atlantic Meridional Overturning Circulation (AMOC) [*Lee et al.*, 2011]. This interaction, also called the Indian-Atlantic supergyre [*de Ruijter et al.*, 1999; *Ridgway et al.*, 2007], constitutes a positive feedback to further warming within the mid-latitudes. Another likely consequence of an expanded supergyre is the poleward contraction of the ACC frontal system.

A clear overall cooling trend is observed at high latitudes, and even more pronounced when the SSTa time series is divided as illustrated in Figure 3.4c. In 2011, mid-latitude waters were on average 0.5°C warmer than in 1981 (r=0.78), whereas the cooling of high-latitude waters was negligible (−0.03°C) and poorly correlated (r=0.06) to the linear regression line. This implies substantial interannual variability in the ACC regime, likely modulated by a repeat pattern of gradual cooling followed by abrupt warming. The first decade (1981−1990) cooling rate was rather gradual (−0.12°C/10yr) and interrupted by the abrupt warming of about 0.6°C in less than two years (January

1991 to December 1992). The second cooling period was relatively shorter (~8 years) but stronger (−0.7°C/10yr), reaching a minimum in January 2000, before switching again to an abrupt warming of 0.8°C in just half a year. By June 2000, any renewed cooling period thereafter was nevertheless negligible.

The question arises as to whether the out-of-phase trends between mid- and high-latitudes might be related to the dominant atmospheric forcing represented by the SAM and ENSO indices. To examine these effects independently, the monthly SSTa is regressed to each spontaneous index as shown in Figure 3.5. These regression maps clearly show the significant inverse correlation (r=−0.72) computed between SAM and ENSO. Therefore, the concurrence of opposite-sign index combinations (e.g. +SAM/−ENSO and −SAM/+ENSO) would reinforce the SSTa oceanic response, whereas same-sign combinations (e.g. +SAM/+ENSO, −SAM/−ENSO) would counter each other or even cancel out any potential SSTa. Strong −ENSO during +SAM periods in 1999 and 2000 resulted in a record-high La Niña event simultaneous to a positive peak in the SAM index, and significant cooling of surface waters at high latitudes with a record-low SSTa in 2000 (Figure 3.4c). Similarly, a strong El Niño (+ENSO) event during −SAM periods in 1991−1992 seem to have rendered the abrupt warming observed during the same period. We conclude that the interaction between these two climate modes of variability modulates the observed interannual fluctuations in SSTa overriding the step-wise decade-long cooling trends observed at high latitudes.

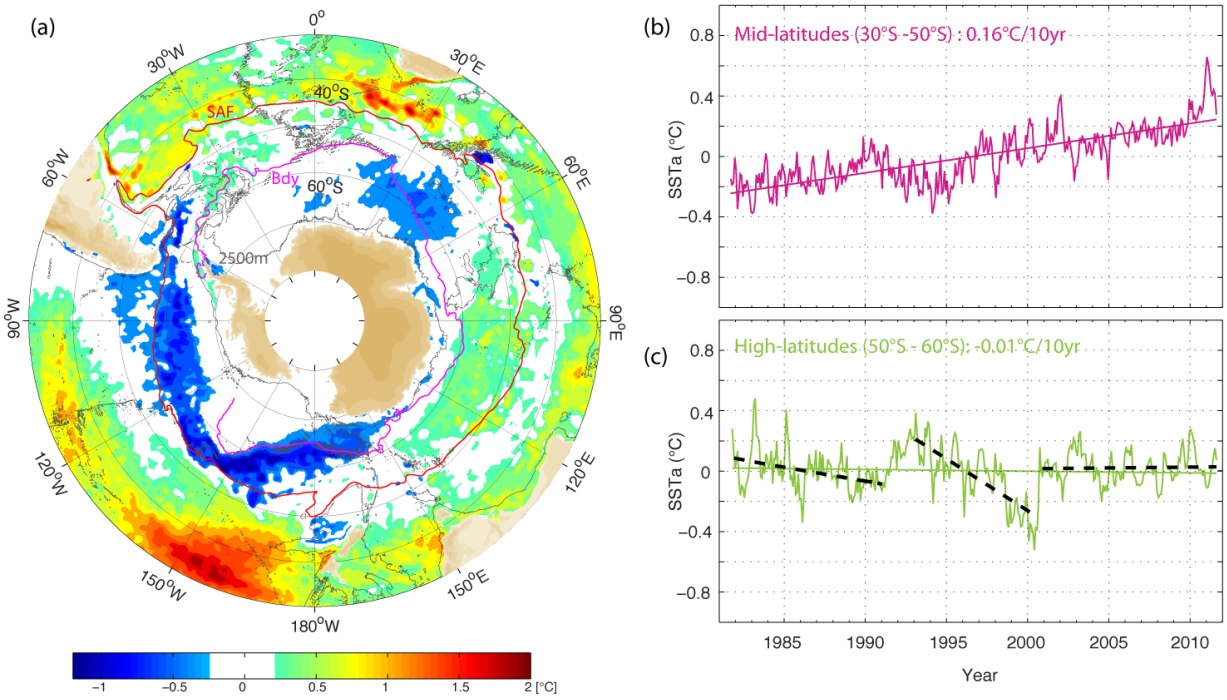

Figure 3.4. Observations of the recent sea surface temperature anomaly change between 1981 and 2010. (a) Spatial map of the linear change (°C). The overlaid red and magenta lines are the −3.5 and −114.0 dyn cm SSH contour, which are the position of the SAF and Bdy representing the northern and southern limit of the ACC (see next chapter for more information). Zonally averaged monthly time series for (b) the mid-latitudes between 30°S and 50°S, and (c) the high latitudes between 50°S and 60°S. Regression lines represent the linear trends for entire time periods (solid), and for the high-latitude region the periods between September 1981 and December 1990, January 1993 and June 2000, and January 2001 and September 2011 (dashed).

In need of further study is the surprisingly steady warming trend observed in the Indian sector (60°E−150°E) between Kerguelen Plateau (KP) and Macquarie Ridge-Hjort Trench. Even though *Aoki et al.* [2005] reported such warming, it is somewhat unexpected because this analysis show negative SSTa regressed on +SAM in that location. This suggests that a different oceanic process might be causing the observed regional warming. One possibility is through eddy diffusion of increasingly warmer waters from the Subantarctic Zone crossing southward into the Polar Frontal Zone (PFZ) between 60°E and 70°E, where the STF and SAF tend to converge and generate the most energetic mesoscale rings [*Sallée et al.,* 2006]. This localized input of extra heat to the PFZ can efficiently raise SST farther downstream, and eventually the Indian sector of the ACC regime.

The signature of the Antarctic Dipole is also evident in Figure 3.5, i.e. the highly asymmetric SSTa response described in *Yuan* [2004]. During +SAM or −ENSO, negative SSTa extend to mid-latitudes in the central South Pacific sector, while positive SSTa enters the high-latitudes of the western South Atlantic. It appears that these are the compounded effects of anomalous surface heat flux and ocean heat transport. A negative SLP anomaly (−SLPa) extends to low latitudes in the Pacific sector during +SAM/−ENSO, and the anomalous cyclonic circulation induced in that area leads to additional transport of warm air into the Bellingshausen/Weddell seas with a retreat in sea-ice cover; whereas the additional transport of cold continental air into the Ross/Amundsen seas show an advance in sea-ice extent. In addition, there is anomalous Ekman transport induced by the enhanced meridional gradient of SLP [*Verdy et al*.,

2006], which selectively push cold waters farther to the north only in the Pacific sector. The lack of a pronounced STF in this sector, unlike along the Indian-Atlantic supergyre, facilitates the 'unexpected' expansion of the cold SSTa in the South Pacific. Also the STF deflects prominently northward just downstream of the Campbell Plateau, which may induce more localized variability in response to atmospheric forcing than in other sectors where it runs parallel and closer to the SAF.

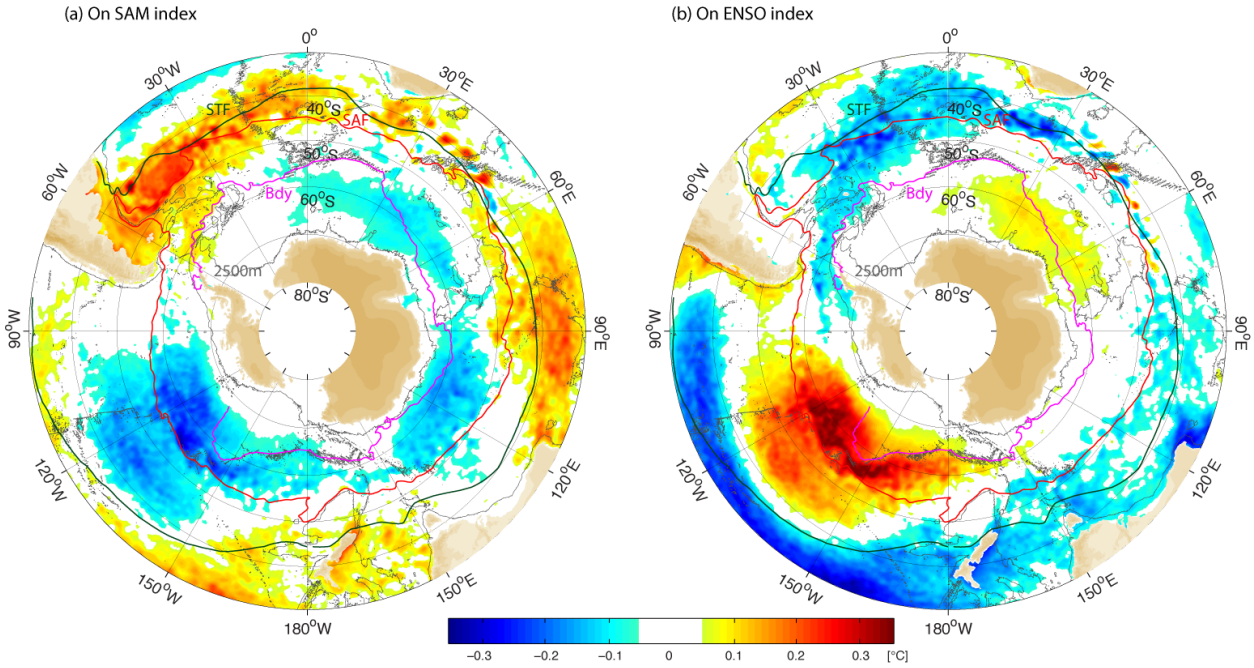

Figure 3.5. Sea surface temperature anomaly regressed maps onto the (a) SAM, and (b) ENSO indices. Regressed values indicate changes in °C corresponding to one standard deviation change in the indices. The overlaid red and magenta circumpolar contours represent the climatological altimetry-based distribution of northern and southern limit of the ACC from this study, and the green line is the STF trace from *Orsi et al.* [1995].

Figure 3.6 shows regression maps with multiple lags to describe the downstream propagation and fading of oceanic perturbations within the ACC domain: a SSTa in response to atmospheric forcing is initially imprinted to the central South Pacific and gradually dissipates farther downstream. The perturbation induced by ENSO arrives at Drake Passage (65°W) about two years later with an average propagation speed of 7.3 cm/s, almost identical (8 cm/s) to that suggested by *Verdy et al.* [2006].

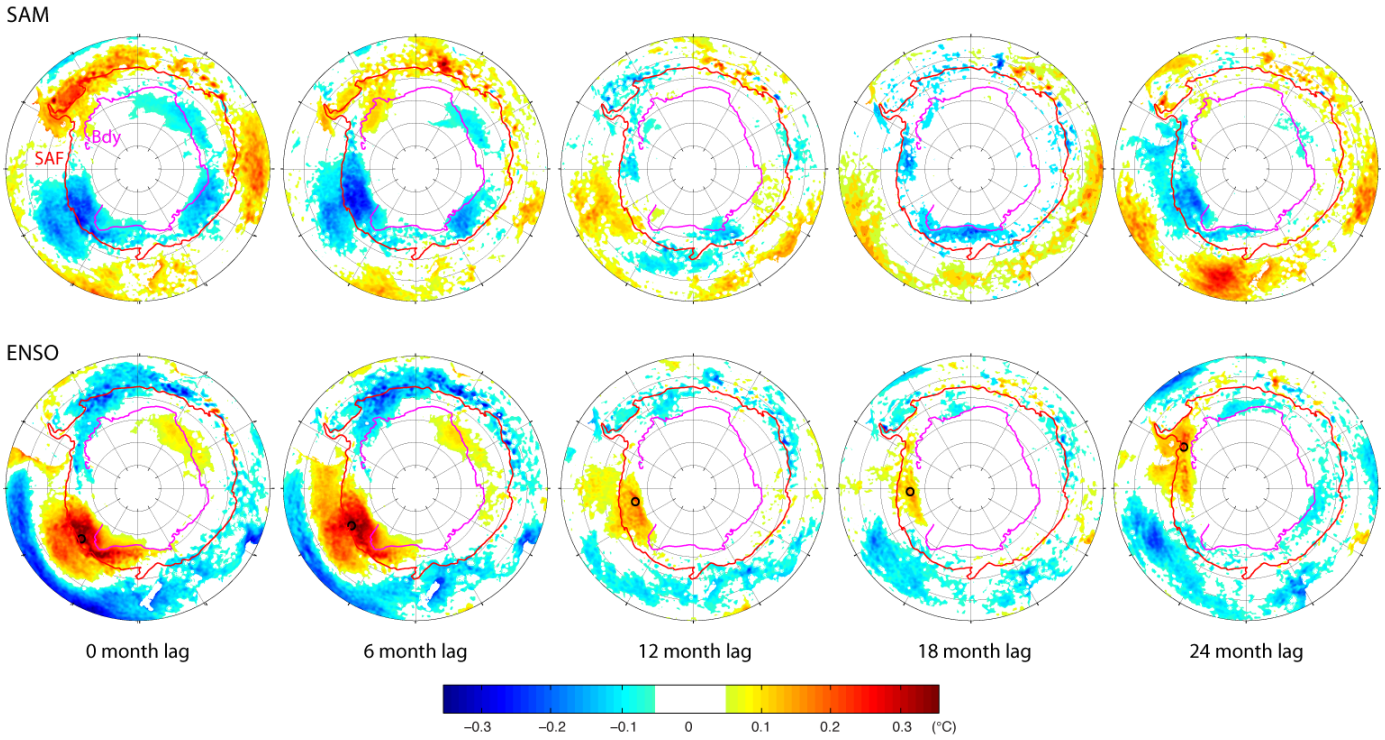

Figure 3.6. Sea surface temperature anomaly regressed maps onto the SAM (upper panel), and ENSO indices (bottom panel) with multiple lags (0 to 24 months; lags imply that the atmospheric forcing are leading). Note that the leftmost maps are the same as Figure 3.5. Black circles in the lower panel represent the maxima of the SSTa to calculate its propagation speed. The overlaid red and magenta lines represent the northern and southern limit of the ACC.

An overall linear change in SSH between 1992 and 2011 is also estimated to investigate the SSTa contribution (Figure 3.7). Unfortunately, sea surface salinity (SSS) data are not yet available at similar spatial and temporal resolutions to SST, thus its contribution to SSH change cannot be estimated. However, SSS trends are generally inferred from SST trends, since e.g. cooling (warming) is generally associated to enhanced surface freshening (salinity) from increased precipitation (evaporation). The estimated Southern Ocean average sea level rise is about 3.1 mm/year, which adds up to an expected total SSHa of up to 6 cm in the past two decades.

However, as shown in Figure 3.7, the SSHa trend is also highly localized. Comparison of the spatial distributions of SSHa and SSTa (Figure 3.4a) trends reveals that the subtropical warming trend must be the main driving mechanism for the observed SSH rise. However, the net effect of the high-latitude cooling trend seems to be either compensated or dominated by the SSSa contribution. Freshening due to increase precipitation [*Sen Gupta and England,* 2006*; Morrow et al.,* 2008] might outstrip cooling in the region between 150°E and 175°W, thus resulting in the observed regional rising trend, but it is almost compensated in both the Pacific sector (175°W−70°W) and upstream of the KP (30°E−60°E), therefore explaining the lack or weak falling trend in those areas.

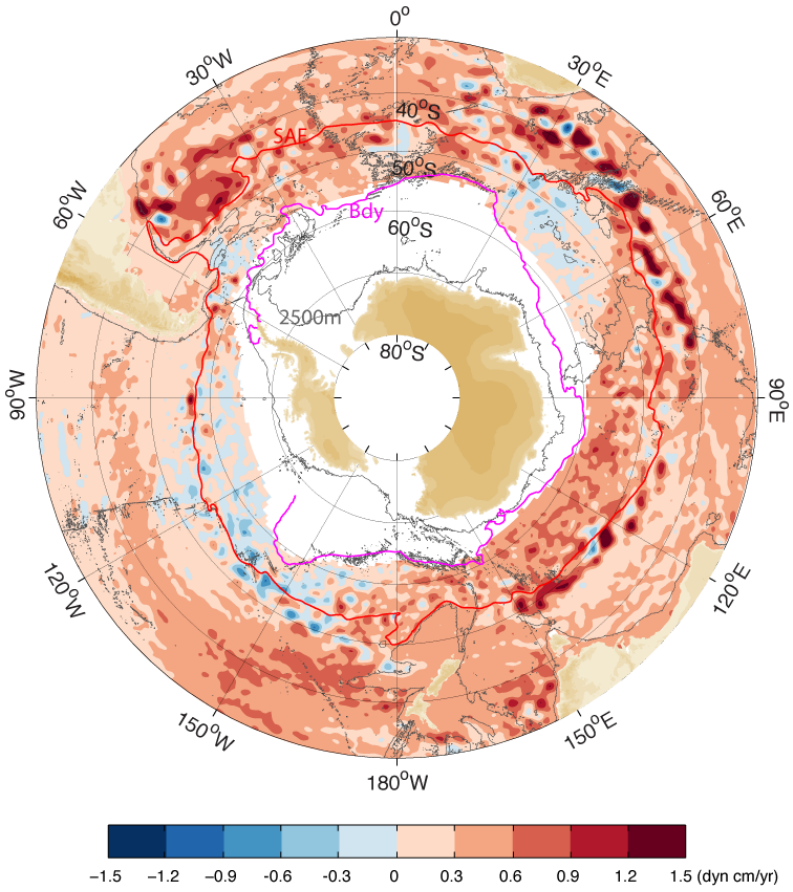

Figure 3.7. Spatial map of linear trends in sea surface height anomaly during 1992 and 2011. The overlaid red and magenta lines represent the northern and southern limit of the ACC.

CHAPTER IV

FRONTAL DISTRIBUTION IN THE SOUTHWEST ATLANTIC

4.1 Altimetry-Based Frontal Indicators

The principal indicators of ACC fronts are the relatively large tilt of isopycnals dynamically associated with geostrophic current cores, and the strong horizontal property gradients corresponding to upper water mass boundaries [*Nowlin et al.,* 1977]. Specific property values are commonly used to indicate the meridional extent of certain water mass characteristic (see table 3 in *Orsi et al.* [1995] for further details). Traditional tracing methods, however, particularly suffer from inadequate sampling, both spatial and temporal, in regions of large frontal variability [*Park et al.,* 2009*; Belkin and Gordon,* 1996].

With the launch of satellite altimeters, descriptive oceanographers gained access to global sustained measurements of SSH to study geostrophic currents and their relationship with the internal density field. Sites with large SSH slope correspond to surface current cores and steep tilting of isopycnals at depths [*Gille,* 1994]. In the Australian sector of the Southern Ocean *Sokolov and Rintoul* [2002; 2007a] identified several bands with relatively large horizontal gradients of SSH (ΔSSH) that persistently aligned with the same SSH contours, albeit showing significant variability. The latter is to be expected if those particular streamlines were in fact representative of ACC frontal locations, which are known to fluctuate in space. Therefore, the adoption of frontal

indicators based on readily available SSH data has become common practice in recent years [*Sallée et al.,* 2008*; Swart et al.,* 2010*; Billany et al.,* 2010].

To find frontal indicators for the southwestern Atlantic Ocean (Figure 2.1), sorted time-averaged SSH and ΔSSH at all (11,582,178) grid point locations within that domain are plotted against each other (red line) and the frequency distribution of grid point vs. SSH (green line) are shown in Figure 4.1. Four distinct peaks in ΔSSH correspond to frequency minima, at the specific SSH contours of −3.5, −38, −61, and −98.5 dyn cm. They indicate four well-documented current cores in this area, while the wider and relatively higher plateaus in Figure 4.1 correspond to the vast less tilted (sluggish flow) areas adjacent to the ACC as well as the zones between its characteristic fronts. Each peak in ΔSSH is lower than 2.5 m/1,000 km, the threshold used to track current filaments in *Sokolov and Rintoul* [2007a; 2009a], since this study includes only the temporally and spatially averaged gradient of SSH, thus filtering out much of the complexity and variability in this region's frontal distribution. Note also that a single SSH streamline does not necessarily need to match exactly the ACC frontal distributions derived from traditional in-situ indicators, since these frontal jets are turbulent motions known to also merge and split around the Southern Ocean.

To validate the new altimetry-based frontal indicators with traditional water mass property criteria, all available high-quality hydrographic profiles (see Table 1, Figure 2.3) occupied during the span of the SSH time-series were examined and assigned to a particular Southern Ocean zone. This zonation of CTD profiles is based on traditional property indicators and characteristic T-S diagrams [*Orsi et al.,* 1995], and named from

north to south, the Subantarctic Zone (SAZ), Polar Frontal Zone (PFZ), Antarctic Zone (AZ), Boundary Zone (BZ), and Subpolar Zone (SPZ).

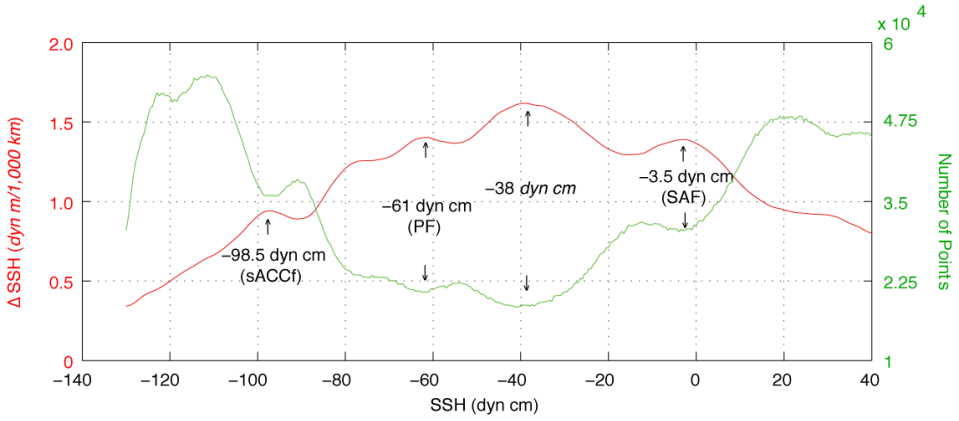

Figure 4.1. Relationship between time-averaged SSH values and its horizontal gradient (red line), and total number of grid points (green line) in the southwestern Atlantic Ocean.

SSH values were assigned to individual profiles by applying a cubic spline (linear) interpolation for the spatial (temporal) domain. Figure 4.2 shows a tight agreement between the two zonation criteria; almost all CTD profiles in the SAZ (92.6%), PFZ (90.9%), AZ (80.1%) assigned using traditional water mass criteria is resolved with the new SSH indicators. The relatively low percentage for the AZ may be the result of frequently observed cold (warm) rings originated at the sACCf (PF). Because the Bdy is not associated with a surface current jet, there is not SSH indicator (peak in Figure 4.1) of its location. For completeness only, the −114 dyn cm value was selected because it maximizes the percentage of the CTD profiles assigned to the BZ

(91.5%) and SPZ (86.6%). That particular SSH contour does track the climatological distribution of the Bdy [*Orsi et al.*, 1995] in the test region very well (see Figure 4.9).

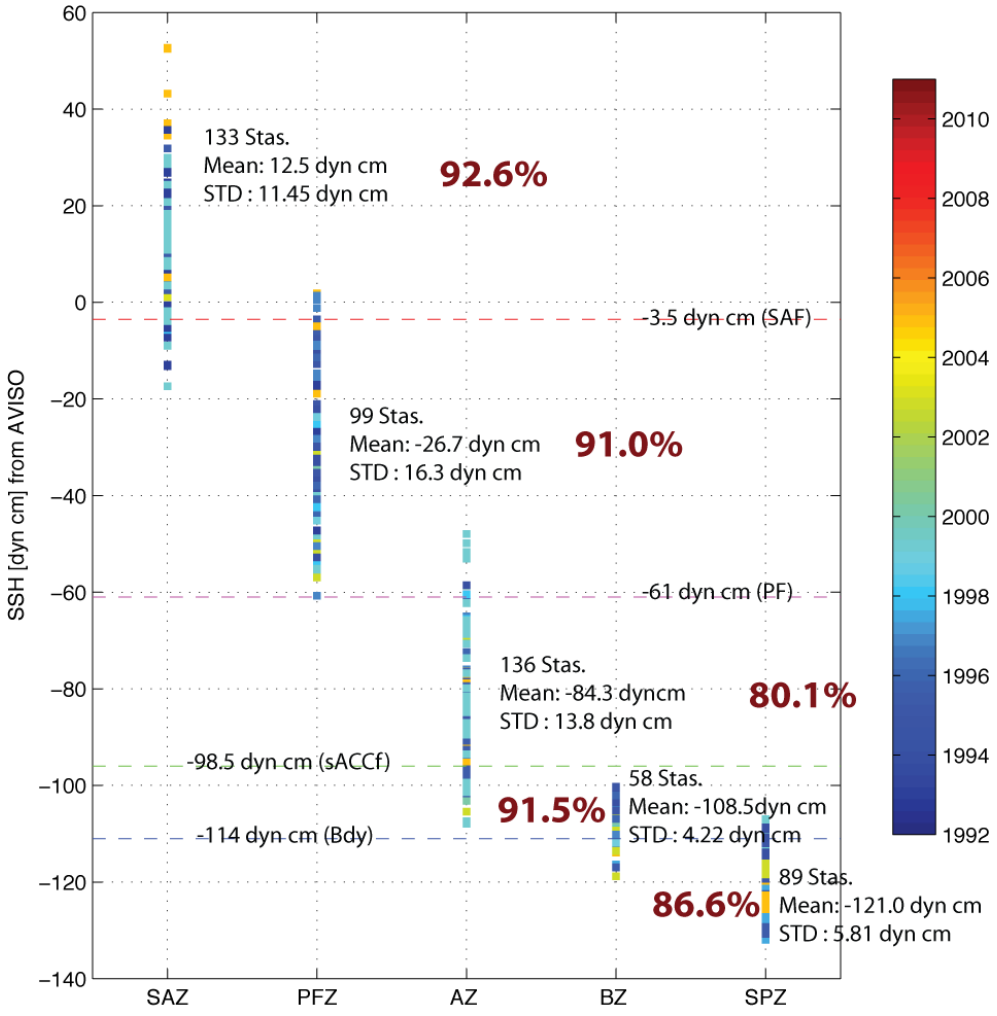

Figure 4.2. Relationship between sea surface height and frontal zones with the 610 CTD casts shown in Figure 2.3.

The −38 dyn cm peak in ΔSSH is not likely associated with the 'permanent' location of the PF, but nevertheless suggests a fairly persistent 'local current filament' located between the SAF and the PF as indicated by the path of that streamline (−38 dyn cm) along the northern flank of the Falkland Ridge. There is no enhanced KE associated with the −38 dyn cm streamline in any of the three sections shown in (Figure 4.4).

4.2 Validation

4.2.1 Kinetic Energy

Before studying spatial-temporal frontal variability based on the new altimetry criteria, it is important to explore their likely signals in climatological (KE) and eddy Kinetic Energy (EKE) fields (Figure 4.3), and in weekly time series at key locations within the study area (Figure 4.4). Overlaid in Figure 4.3 are the four frontal traces extracted from 19-year averaged Absolute Dynamic Topography (ADT), to note that multiple narrow cores of enhanced of KE are closely distributed to frontal streamlines. In areas of active frontal interactions either with underlying topography, adjacent filaments or eddies, the intensity and width of these cores is expected to vary considerably more than elsewhere. Intensified fronts tend to concentrate over very steep topography, like it is seen along the band exceeding 1,500 $cm^2\ s^{-2}$ of KE and aligned to the SAF indicator (−3.5 dyn cm) streamline where it is likely 'locked' to the 1,500 m isobath off Argentina's continental slope. The lack of frontal interactions over abyssal plains is reflected by much lower KE values, e.g. KE levels over the Argentine and Yaghan basins are only about one half of those at the 'locked' SAF.

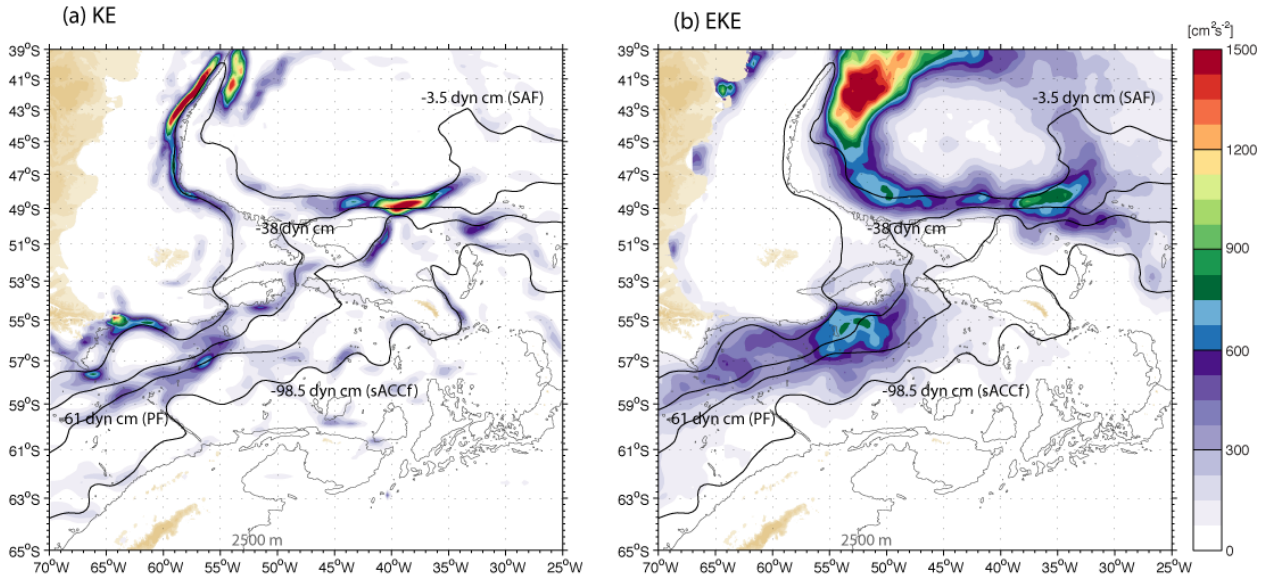

Figure 4.3. Averaged (a) kinetic energy, (b) and eddy kinetic energy field calculated from the absolute dynamic topography field. The overlaid lines are SSH contours with −3.5, −38, −61, and −98.5, which are associated with enhanced gradient of sea surface height.

More complex front-to-front interactions are the merging and splitting of jets into multiple filaments, and the shedding of mesoscale rings [*Sokolov and Rintoul,* 2002*; Dong et al.,* 2006*; Sallée et al.,* 2008]. The Drake Passage 'squeeze' and its rough underlying topography prompt ACC fronts to interact more readily. The two streamlines associated with the PF converge near 56.5°W, where shedding of eddies is the most frequent within the PFZ, at the region immediately downstream centered at 52.5°W (EKE ≥ 600 cm^2s^{-2} Figure 4.3b). Much farther east at the southern Argentine Basin, all the high KE filaments merge into a single very intense current core, roughly centered

along the −38 dyn cm contour and right in front of the Falkland Gap near 39°W [*Peterson and Whitworth,* 1989*; Whitworth et al.,* 1991; *Orsi et al,* 1995].

On the eastern flank of the SAF retroflection there is a narrow high KE strip (Figure 4.3a) tracing the path of the STF right at the Malvinas/Brazil Currents Confluence [*Peterson and Whitworth,* 1989]. The wider south-protruding tongue of high EKE (>1,500 cm^2s^{-2}) and lower KE farther offshore results from large unconstrained meandering of the Brazil Current Retroflection in the interior of the Argentine Basin (see Figure 4.7a). Enhanced EKE is also common immediately downstream of frontal divergences (Figure 4.3b) and of large-scale topographic features: within the PFZ, just east of 55°W in the eastern Scotia Sea and of 39°W in southeastern corner of the Argentine Basin. Here the EKE peak bifurcates with one branch turning counter-clockwise with the SAF, while the other to the southeast within the PF and sACCf.

The PF streamline (−61 dyn cm) reaches the Falkland Ridge and continues into the Argentine Basin around the eastern flank of the MEB. The sACCf streamline (−98.5 dyn cm) shows the weakest levels of KE and in most areas is not clearly distinguished from background energy levels, except where the sACCf interacts with steep topography like the SFZ and the SGI.

4.2.2 Temporal

The dominant physical mechanism driving temporal variability in Southern Ocean SSH is still under debate [*Morrow et al.,* 2008], but certainly the oceanic responses vary with regions: upward trend (10 mm/yr) in the southern Argentine Basin,

downward trend (-5 mm/yr) in the Yaghan Basin, where *Chereskin et al.* [2009] also reported abyssal cyclogenesis of energetic rings. The Southern Ocean has an average trend of 3.3 mm/year (Figure 3.7), thus there was about 6 cm of mean SL in the past two decades. Next we test the robustness of SSH frontal indicators over time.

Figure 4.4 shows the temporal evolution of KE and frontal indicators at three fixed locations. The fluctuating nature of KE peaks over these nineteen years implies a more complicated variability in the ACC system than the monotonic drifts suggested in previous studies. In spite of its complexity, the three SSH frontal indicators track the current cores (maxima in KE) rather well since 1992. Three distinct KE maxima remained aligned with the frontal streamlines at Drake Passage (30°S, Figure 4.4a). We also note that the mean SAF latitude (57°S) shows 2° latitude fluctuations, thus often times the SAF and the PF have 'merged' into an intensified jet, whereas other times individual ACC fronts weakened as they split. The central Scotia Sea section (47.5°S, Figure 4.4b) shows very similar features and a KE peak associated with the STF near 40°S. On the western section (30°W, Figure 4.4c) two distinct and persistent southernmost jets are revealed, but the northern branch is a lot more scattered suggesting larger and more often meandering or shedding of rings.

4.2.3 Hydrographic

Dynamic height (ϕ) based frontal indicators calculated from in-situ CTD profiles ought to mimic those based on satellite SSH. Table 3 summarizes specific ϕ values and integration ranges used to trace ACC fronts in previous studies. *Orsi et al.* [1995] also

selected the 0.9 dyn m (0.35 dyn m) to represent the northernmost (southernmost) continuous streamline within the ACC domain. Recent studies use deeper reference level due to the increased availability of hydrographic profiles from Argo floats and gridded data products like the WOCE climatology. A clear linear relationship

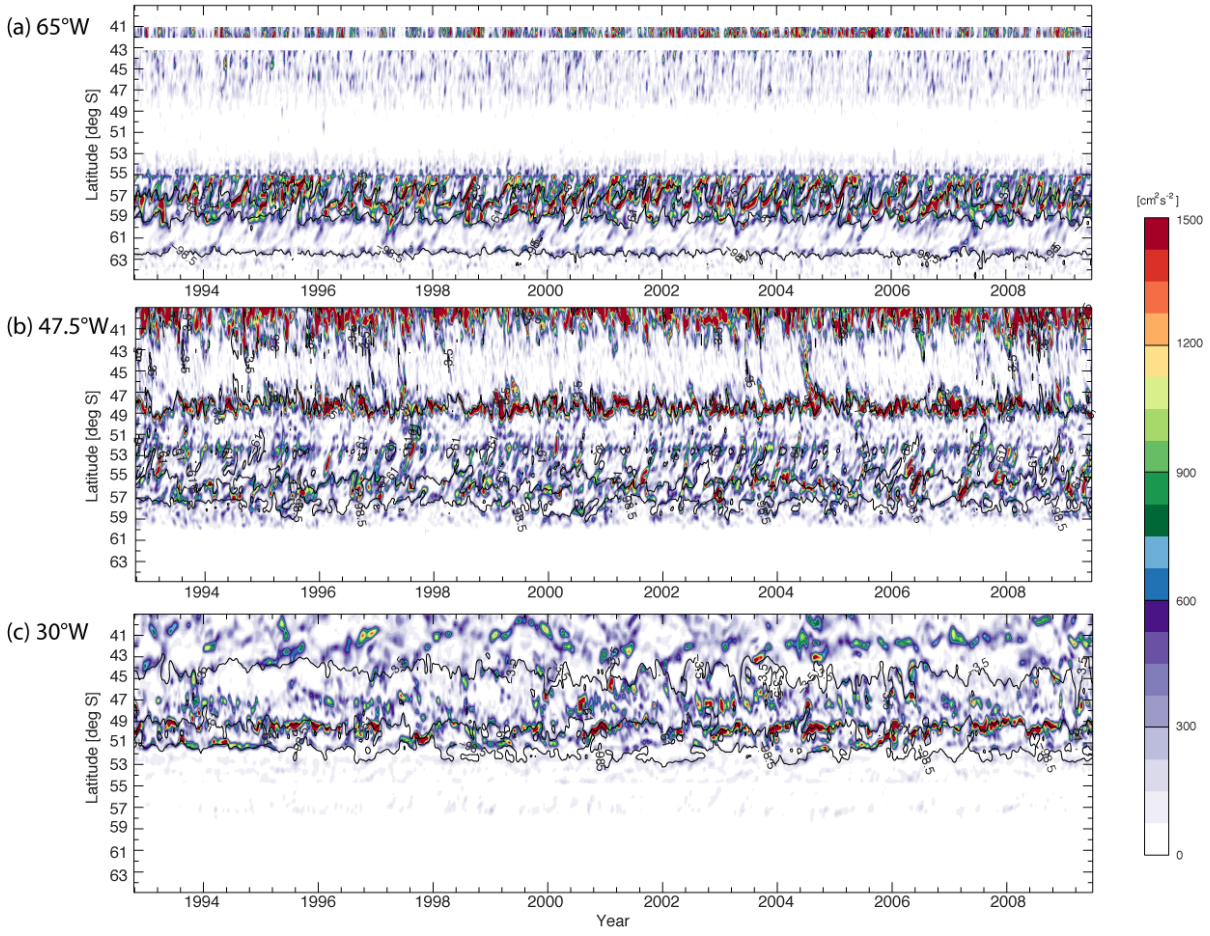

Figure 4.4. A Hovmöller representation of the kinetic energy (cm^2/s^2) and satellite streamlines of −3.5, −61, and −98.5 dyn cm in (a) Drake Passage (65°W), (b) the central South Scotia Sea (47.5°W), and (c) the South Scotia Arc (30°W) since October 1992.

exists between ϕ and SSH data is indicated by the first order empirical fits (thick lines) overlaid in Figure 4.5. The correlation is very high (r >= 0.98) and statistically significant at a 99% level using a student t-test.

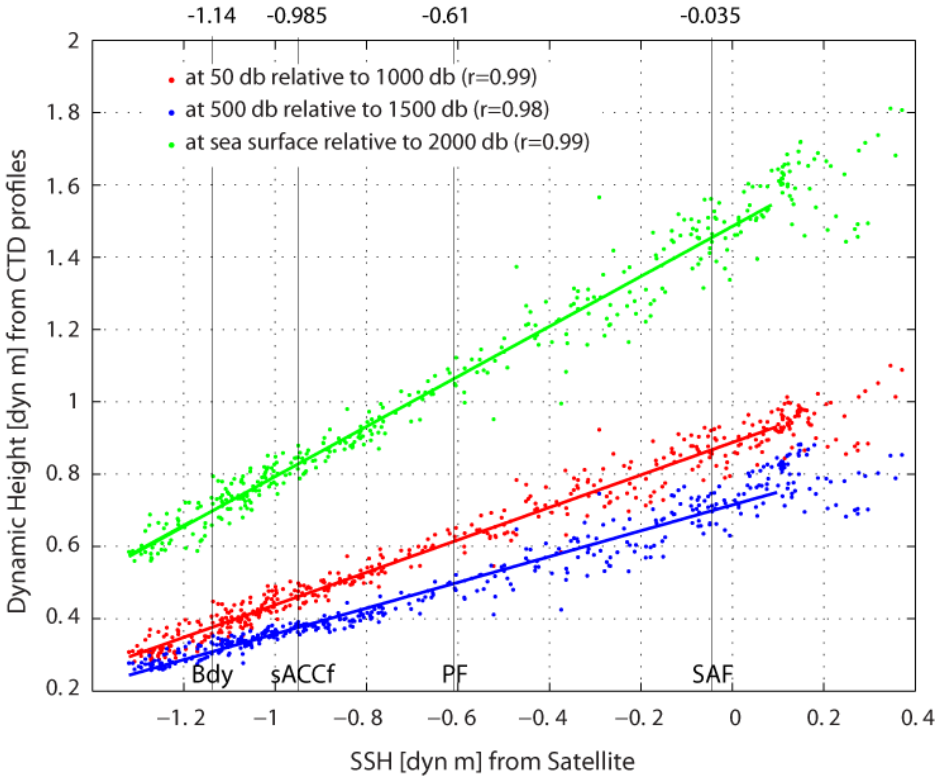

Figure 4.5. Scatter plot of dynamic height at the 50 db relative to 1,000 db (red dots), 500 db relative to 1,500 db (blue dots), and surface relative to 2,000 db (green dots) versus the streamlines from satellites for the CTD profiles shown in Figure 2.3. Thick colored straight lines represent the 1st order least square fit.

Table 3. Summary of ACC Frontal Indicators Based on Streamlines from Satellites and from CTD Stations Obtained from Figure 4.5 and Previous Studies.

Front	SSH (dyn cm)	$\phi_{1,000\,db}^{50\,db}$ (dyn m)	$\phi_{1,500\,db}^{500\,db}$ (dyn m)	$\phi_{2,000\,db}^{0\,db}$ (dyn m)
SAF	−3.5	0.87 (0.9[a])	0.70 (0.7[c])	1.46 (1.73[d])
PF	−61	0.62	0.50 (0.54[c])	1.06 (1.43[d])
sACCf	−98.5	0.45 (0.45[b])	0.36	0.81
Bdy	−114	0.38 (0.35[a])	0.31	0.70

[a] *Orsi et al.* [1995] to represent the ACC in the Southern Ocean.

b *Thorpe et al.* [2002] to identify the climatological location of the sACCf near the South Georgia Island.

[c] *Garabato et al.* [2009] to identify the SAF and PF in Drake Passage.

[d] *Böning et al.* [2008] to represent the climatological location of the ACC fronts using CARS gridded atlas in the Southern Ocean. The unit is converted from m to dyn m for comparison purpose by dividing by the gravitational coefficient.

Previously suggested contours for the tracing of ACC fronts match those corresponding to the SSH indicators determined in this study. The ϕ indicator for the sACCf matches *Thorpe et al.* [2002]; for the SAF and Bdy fall within 0.03 dyn m of *Orsi et al.* [1995]. The indicator for the SAF matches *Garabato et al.* [2009], but their 0.54 dyn m PF streamline is slightly slight different than in this study (0.50 dyn m). However, the climatological location of the 0.54 dyn m at Drake Passage is 57.7°S, thus likely associated with a northern expression of the PF [*Lenn et al.*, 2007], whereas that for the 0.50 dyn m at 60°W is 58.9°S, consistent also with the PF location at Drake Passage derived from temperature indicators on five years of XBT observations

[*Sprintall*, 2003] and from detecting enhanced velocity cores on Shipboard ADCP data [*Lenn et al.*, 2007]. There is only one striking discrepancy, between this study and *Böning et al.* [2008] for the indicators (Table 3). Their suggested SAF and PF values are significantly higher than in this study, implying that climatological positions extend farther north than in this study and in *Orsi et al.* [1995] (see also Figure 5.2 and Chapter 5 for details on circumpolar paths suggested in *Böning et al.* [2008]).

The dynamic height database is extended with about 10,000 Argo profiles to investigate the spatial distribution and temporal variability of ACC frontal indicators. The dynamic topography shown in Figure 4.6 is in remarkable agreement with the climatological SSH contours. The few noticeable differences are in the regions north of the SGI and in the middle of the Argentine Basin. Numerical simulations [*Thorpe et al*., 2002] show the western retroflection of the sACCf to the north of the SGI, as the climatological path in *Orsi et al.* [1995], only intermittently: two occurrences in six modeled years. The sACCf generally rounds the SGI counter-clockwise along the continental slope and the North Georgia Rise blocks its path. Thus, the observed low dynamic height in this region seems to be an episodic western extension of the sACCf. Open water areas with relatively low dynamic heights in the Argentine Basin seem to be traces cold rings detached from the confluence of the SAF and PF just downstream of the Falkland Gap (36°W), which in turn feed the eastern limb of the Zapiola Anticyclone [*Whitworth et al.*, 1991; *Miranda et al*., 1999; *Fu*, 2006; *Volkov and Fu,* 2008], with speeds up to 12.5 cm/sec at the intermediate depths (see Figure 4.8b). Through the northward export of these cold rings, waters from the PFZ are entrained into the

subtropical regime in the Argentine Basin and thus slightly lower the SSH along the anticyclone's perimeter (Figure 2.2a).

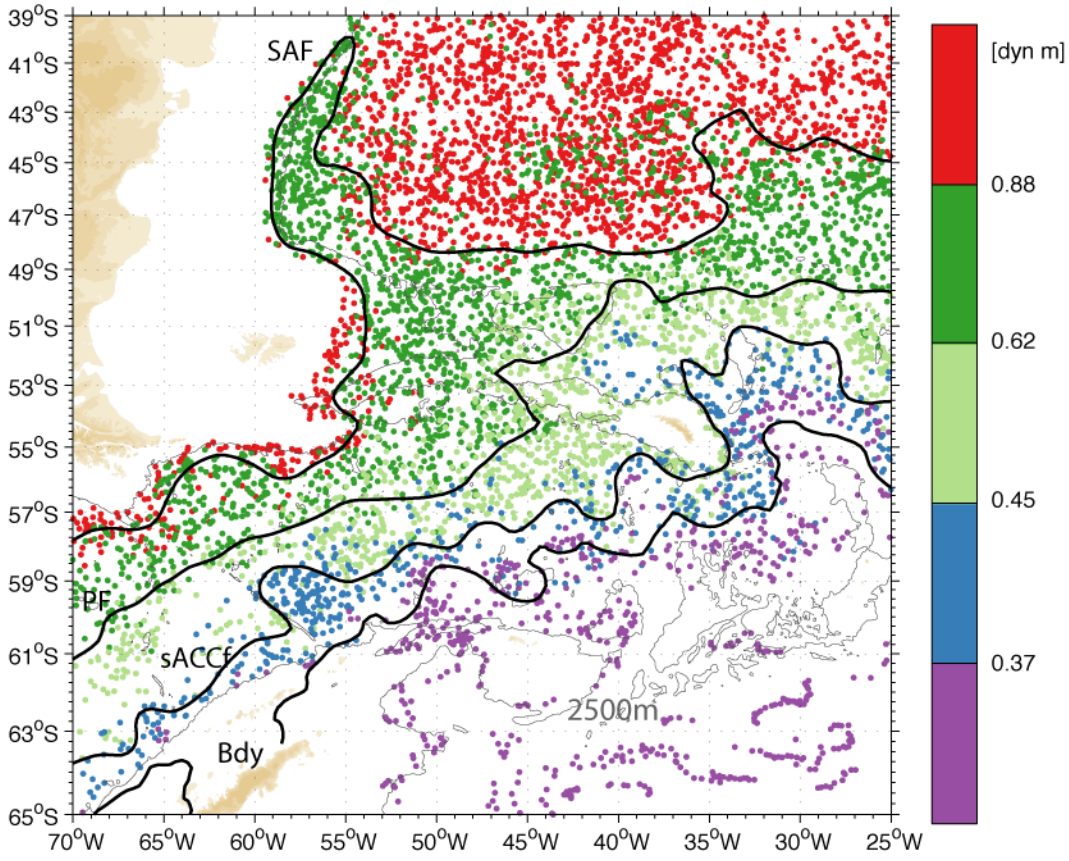

Figure 4.6. Dynamic height (dyn m) calculated from individual Argo profiles at 50 db with respect to 1,000 db with climatological locations of the ACC fronts (thick black contours) derived from satellite altimetry criteria.

4.2.4 Argo floats and surface drifters

Trajectories of Autonomous Lagrangian drifters and Argo floats provide velocity data to map currents at the sea surface and various parking levels with relatively high accuracy [*Park et al.,* 2005], and also test the SSH frontal indicators with adequate spatial and temporal coverage and no seasonal biases. Individual trajectories (Figure 4.7) have been objectively mapped onto a ¼° grid to generate climatological velocity and EKE fields at the sea surface and 1,000 db. These maps (Figure 4.8) reveal narrow, filament-like structures at the surface and broad, frontal structures within the ACC at intermediate depths. Overall the newly suggested frontal indicators in this study (thin black lines) trace some of the many surface filaments, but instead they follow very closely the observed intermediate current cores. *Sokolov and Rintoul* [2009a] postulate that multiple current cores are widespread within the ACC domain under the assumption that sea surface velocity fields are useful frontal indicators. Frontal distributions determined from direct current measurements at intermediate depths, however, indicate that traditional property based indicators are accurate and more reliable than transient-prone surface currents. In fact, as shown in Figure 4.8b, they can accurately depict the anticyclonic gyre around the Zapiola Rise and determine its mean velocity of about 12.5 cm/s, which is almost the same as the local bottom velocities estimated from SADCP adjusted CTD data [*Saunders and King,* 1995].

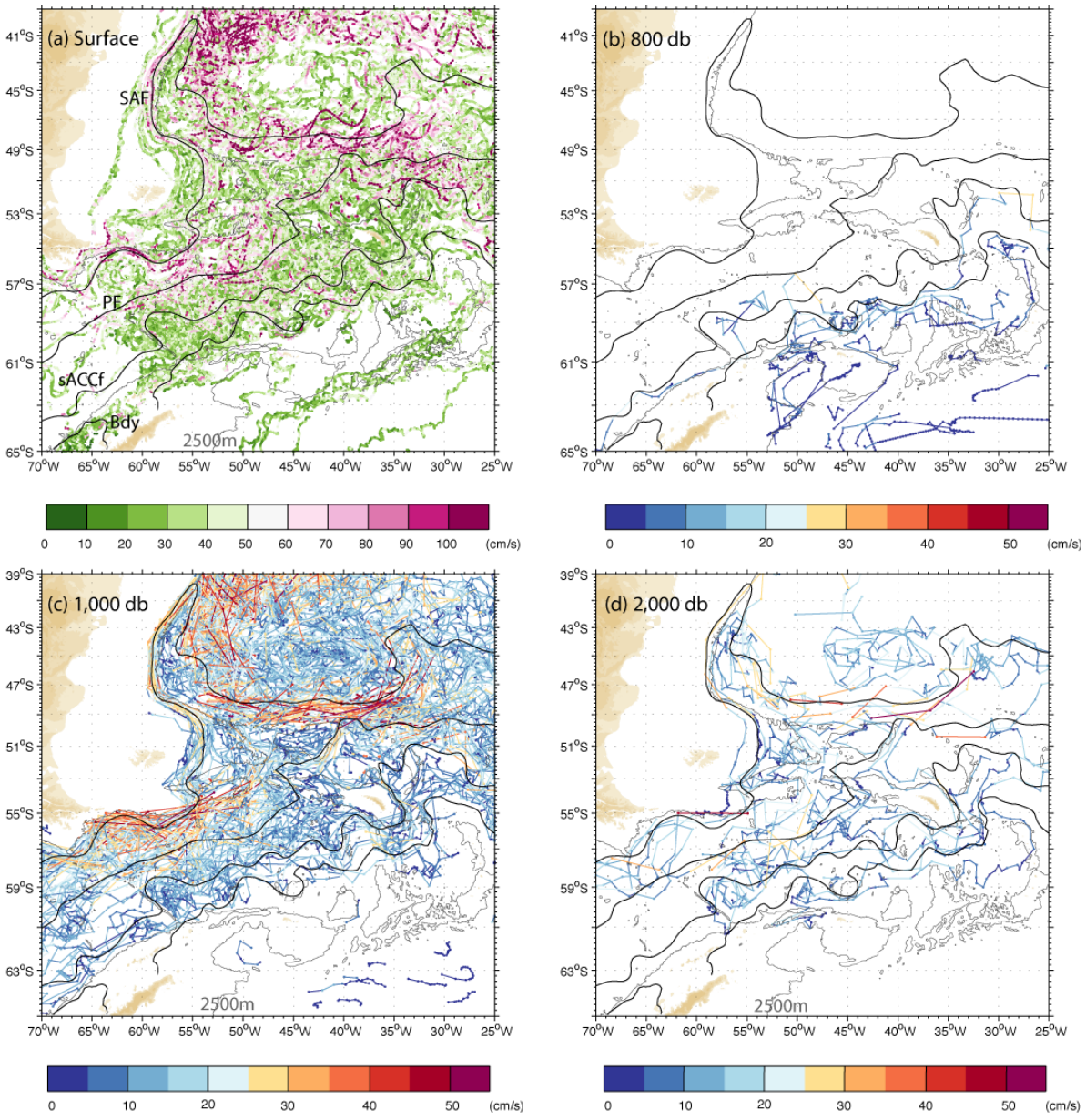

Figure 4.7. Trajectory maps, color-coded based on current speeds, of (a) surface drifters, and Argo floats at different parking levels, i.e., (b) 800 db, (c) 1,000 db, and (d) 2,000 db; the climatological locations of the ACC fronts as defined by satellite altimetry criteria are overlaid as black lines.

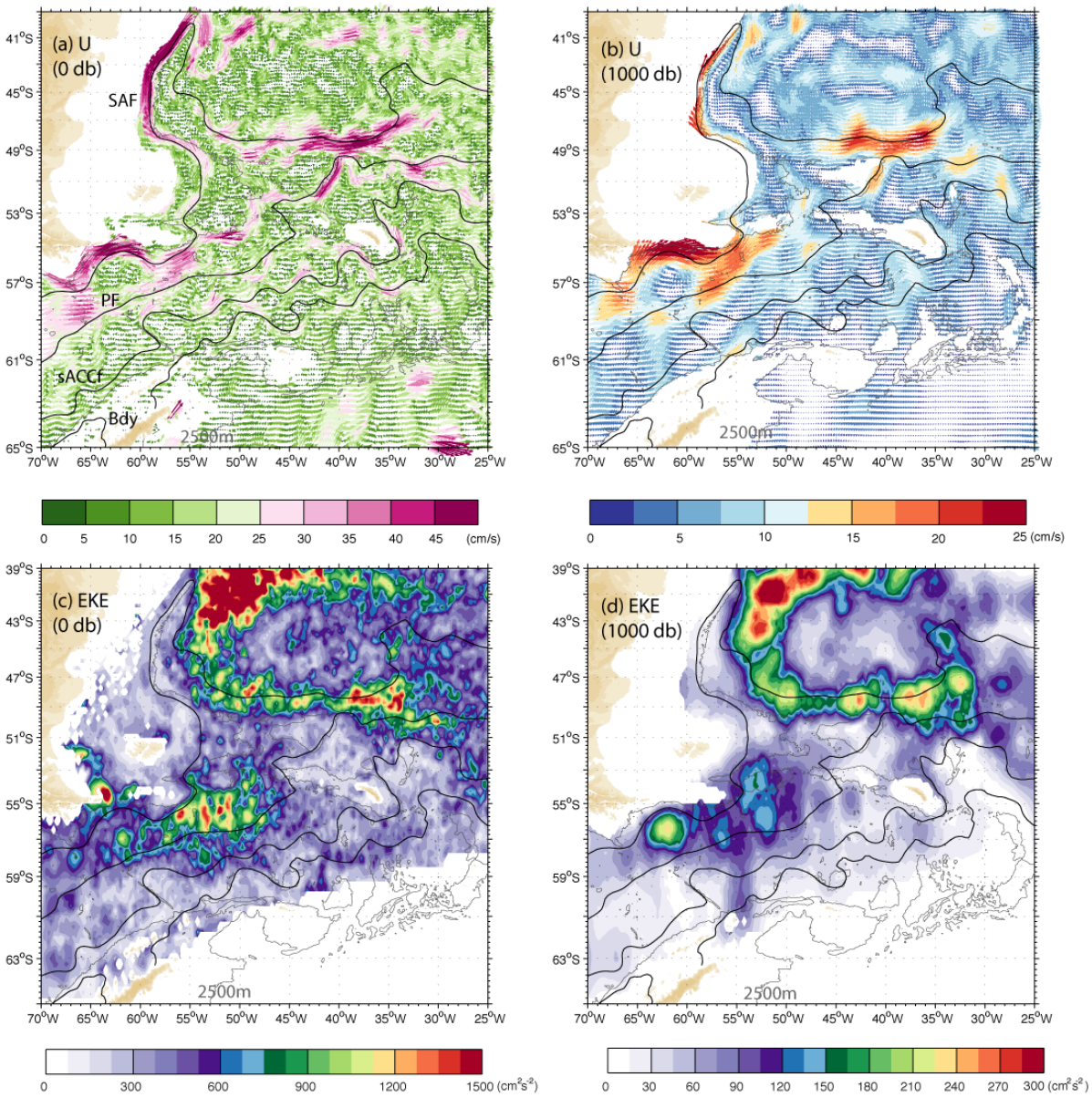

Figure 4.8. Objectively mapped (a−b) mean velocities, and (c−d) mean eddy kinetic energy (cm^2/s^2) at the surface level from surface drifters (left column) and at the 1,000 db from Argo floats (right column); the climatological locations of ACC fronts as defined by satellite altimetry criteria are overlaid as black lines.

4.3 Distribution

Drake Passage is one of the most studied areas in the Southern Ocean for tracking the locations of the ACC fronts and their variability. Mean frontal paths from different studies [*Orsi et al.,* 1995*; Sokolov and Rintoul,* 2009a*; Sallée et al.,* 2008] are shown in Figure 4.9. Using hydrographic data, *Orsi et al.* [1995] traced fronts based on specific values of water properties that represent distinct water mass changes across the fronts. *Sokolov and Rintoul* [2009a] used a 15-year time-series of the SLA with MDT relative to 2,500 db calculated from the WOCE hydrographic climatology [*Gouretski and Koltermann,* 2004]. They depict nine filaments for the ACC fronts (see their table 1). The middle branch of the SAF, northern branches of the PF and sACCf, and the Bdy among those 9 filaments are used to represent the traditional locations of the ACC fronts, (1.23 m for the SAF, 0.9 m for the PF, 0.64 m for the sACCf, and 0.51 m for the Bdy). *Sallée et al.* [2008] extend studies of *Sokolov and Rintoul* [2002; 2007a] based on a newly generated MDT field from combining the Argo data and the SODB data. To describe the SAF and PF they selected the 1.20 m and 0.95 m contours relative to a 1,500 db. Curiously, did not derive a mean position for the SAF where its turns north sharply toward the BMC Zone, presumably due to increased statistical error in their MDT field. Thus, they excluded the test area in this study while seeking the relationship between atmospheric forcing and its impact to the ACC frontal variability.

The climatological path of the SAF derived in this study reveals tight constraint imposed by the bottom topography. The −3.5 dyn cm contour (i.e., the northernmost

black line in Figure 4.9) flows over the northern shelf/slope in Drake Passage and then turns to the north at the Burdwood Bank, closely following the 1,500 m isobath on the western side of the Argentine Basin up to 40°S. Here the SAF encounters the Brazil Current and returns south all the way to northern flank of the Falkland Ridge. Farther downstream the SAF extends farther to the north than in previous studies [*Orsi et al.,* 1995*; Sokolov and Rintoul,* 2009a*; Sallée et al.,* 2008]. Beyond 35°W, it follows the abyssal slope of the Argentine Basin and turns back east at about 43°S; whereas in *Orsi et al.* [1995] the SAF shows two meander-like loops, first to the south and then to the north. Although they cannot be detected in this study, they may not be part of the climatological path either, but rather induced by transient meandering of the SAF captured during a particular hydrographic cruise. Within the Argentine Basin, a path for the SAF in *Sokolov and Rintoul* [2009a] shows a ring-like feature (Figure 4.9) in an area here determined as the least energetic within the test region, and likely not due to errors in the MDT fields calculated from the WOCE climatology.

Our climatological PF path corresponds well with the mean paths from pervious studies except near the Maureen Ewing Bank (MEB). *Orsi et al.* [1995] and *Sallée et al.* [2008] place the PF at the northern flank of the MEB; and *Peterson and Whitworth* [1989] also reported the merging of the SAF and PF at the northern side of the MEB in their analysis of the 1986 R/V Melville cruise hydrographic data. However, *Sokolov and Rintoul* [2009a] and this study locate mean paths of the PF at the southern side of this bank. The southern path of the PF is supported by recent intense hydrographic observations from ALBATROSS 1999 [*Garabato et al.,* 2002] and JR11 1996 [*Trathan*

et al., 2000] cruises. *Garabato et al.* [2002] suggested that the PF passes south of the Bank, and the remnants of a meander of the PF north of the Bank. The northern path of the PF suggested by *Orsi et al.* [1995] might be biased by poleward frontal drifts over long periods. The test-area averaged path of the PF shows a significant poleward drift with a rate of 40.5 km/10yr, and probably enough to force the PF to move onto the southern flank.

One of the major differences between *Orsi et al.* [1995] and this study is found south of the SGI, where their sACCf and Bdy extend farther south. Their sACCf turns southeastward at 45°W and seems to follow the −114 dyn cm contour before aligning again with the −98.5 dyn cm. The southward bias observed in climatological frontal locations can be explained by the coarse resolution of historical in-situ data as well as the strong seasonal bias in the vastly summer historical hydrography, when fronts tend to be displaced to the south. This is consistent with the observed seasonal fluctuations of the sACCf in the test region: the maximum seasonal fluctuation recorded in this area is about 150 km, with a record-length mean of 34 km. The climatological mean position of the Bdy from *Sokolov and Rintoul* [2009a] is located much farther south than both *Orsi et al.* [1995] and in this study, and up to 3° south of the SGI.

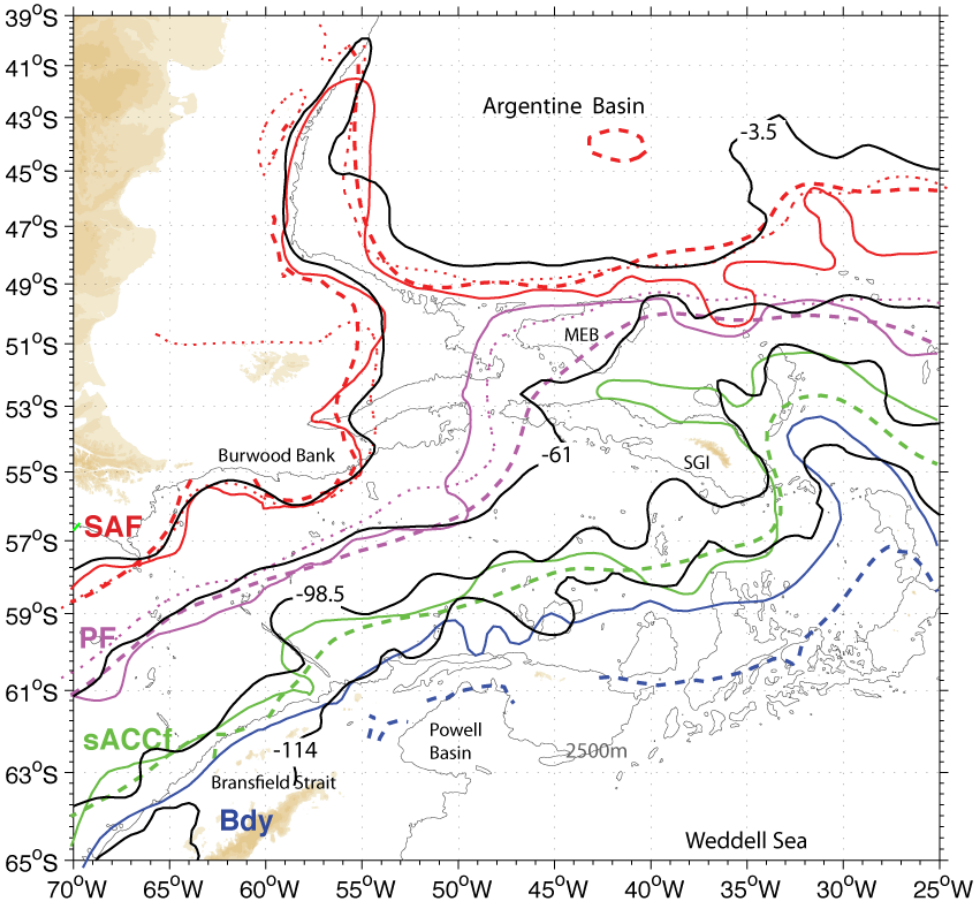

Figure 4.9. Mean distribution of ACC fronts derived from this study (black SSH contours). Color contours indicate mean paths of the ACC fronts from *Orsi et al*. [1995, solid], *Sokolov and Rintoul* [2009a; dashed], and *Sallée et al.* [2008, dotted].

CHAPTER V

GLOBAL DISTRIBUTION AND VARIABILITY OF FRONTS

5.1 Circumpolar Traces

Global applicability of frontal SSH streamlines was implied by *Swart et al.* [2010], unless water particles following these particular paths would have undergone different physical process or have mixed with waters with contrasting characteristics. We will derive frontal distributions based on SSH streamlines for the entire Southern Ocean using two independent approaches. First using in-situ dynamic height fields (Figure 5.1a), and then using objectively mapped velocity fields derived from the extended Argo floats database (Figure 5.1b).

A high linear correlation between altimetry-derived and hydrography-derived dynamic height fields is also found almost everywhere in Southern Ocean. E.g. the strong northward-flowing Bdy along the eastern flank of the KP is resolved by the Argo climatology with speeds > 15 cm/s at 1,000 db (Figure 5.1b). This is the Deep Western Boundary Current (DWBC) of a cyclonic circulation in the Australian-Antarctic Basin described in analyses of synoptic hydrographic observations [*Orsi et al.,* 1999; *Park et al.,* 2009], long-term direct current measurements [*Fukamachi et al.,* 2010], and instrumented elephant seals as well as climatological data sets [*Roquet et al.,* 2009]. *Fukamachi et al*. [2010] report a year-mean bottom intensified flow of about 20 cm/s at ~3,500 m and the associated northward transport of AABW as 10.3 ± 4.3 Sv.

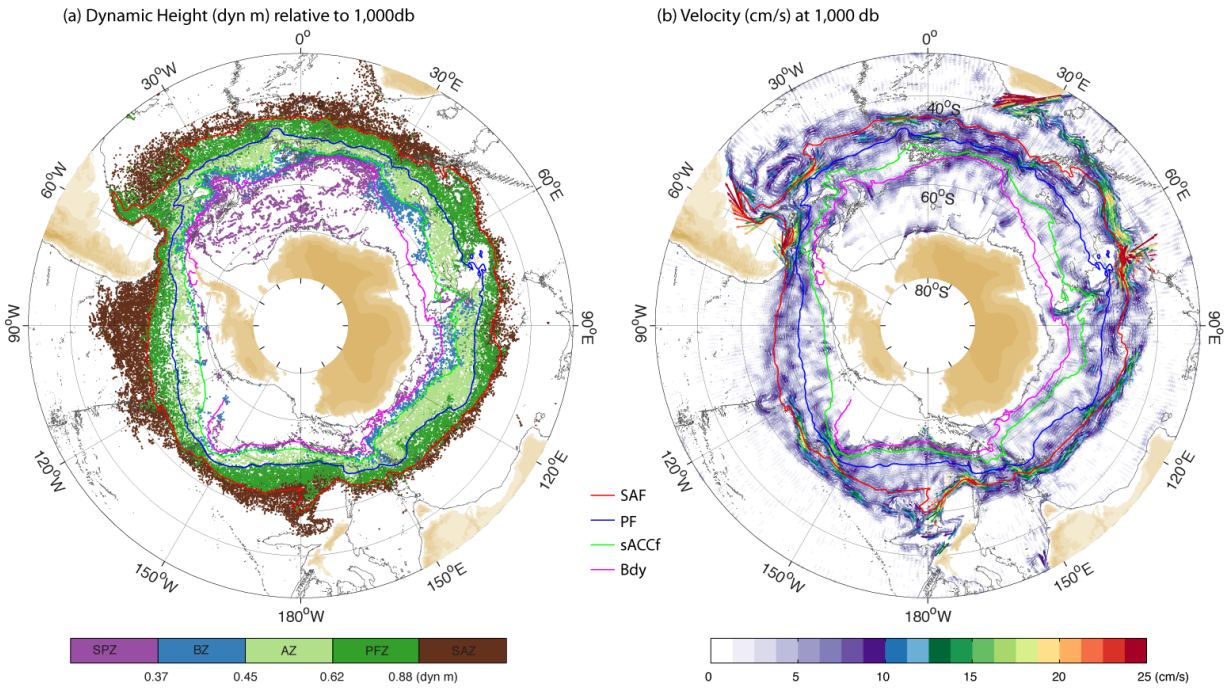

Figure 5.1. (a) Observed dynamic height at 50 db with respect to 1,000 db and (b) objectively mapped velocity at 1,000 db from Argo trajectories; the climatological location of ACC fronts (colored lines) are derived from satellite altimetry.

The mean frontal paths from previous studies [*Orsi et al.,* 1995*; Sokolov and Rintoul* 2009a*; Böning et al.,* 2008*; Sallée et al.,* 2008] are shown in Figure 5.2 and their indicators are summarized in Table 4. There is significant discrepancy between the frontal locations in *Böning et al.* [2008] and those appearing in most recent studies. Their anomalous northern circumpolar-mean latitudes for the SAF and PF (see their figure 3a, 4a, and 5a), i.e. up to 7° (SAF) and 17° (PF) farther to the north in the Argentine Basin compare to this study, seriously influenced their selection of geographic boundaries, and thus also their conclusions while quantifying variability of water mass properties in the ACC since the 1960s.

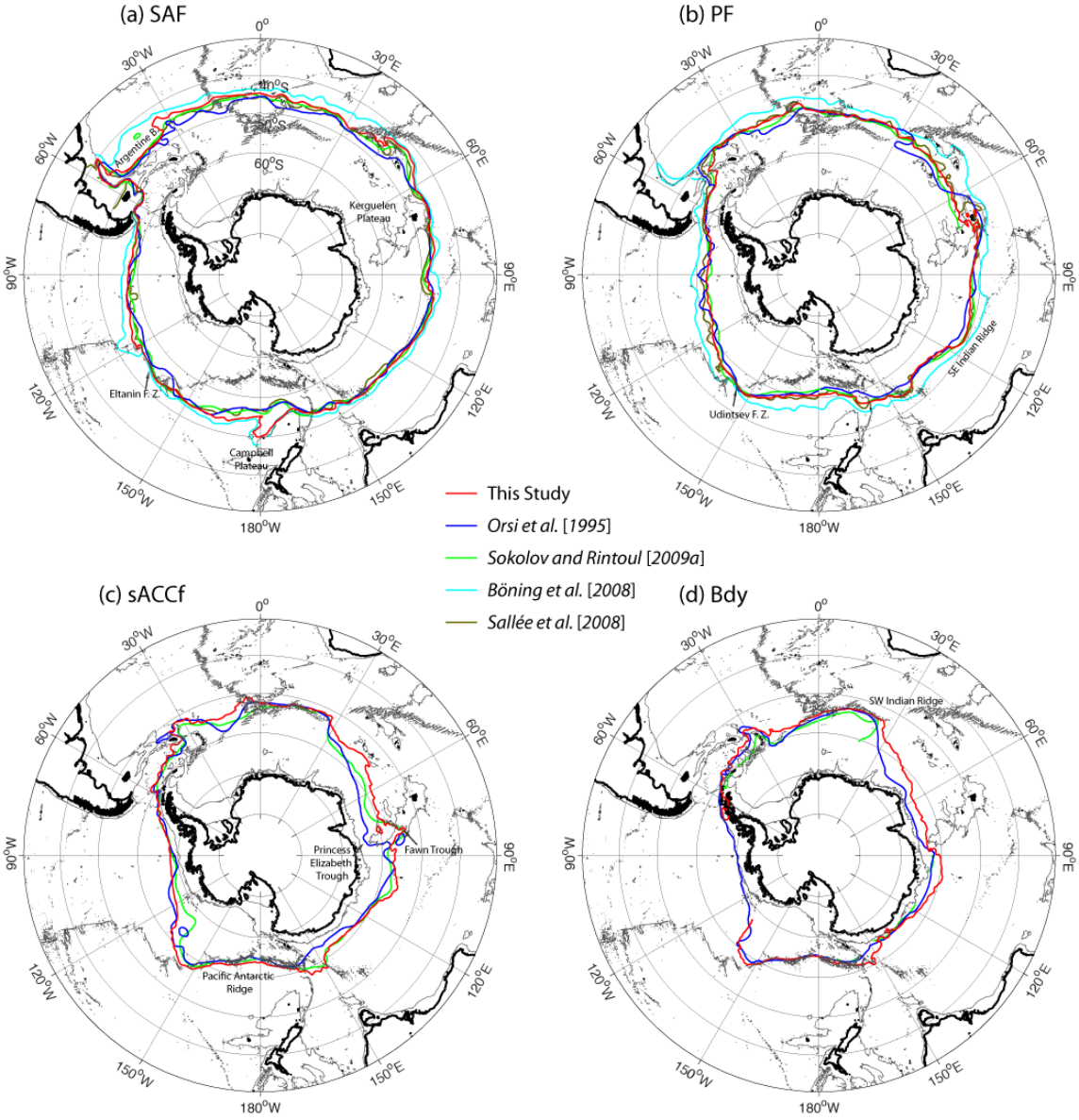

Figure 5.2. Climatological locations of the (a) SAF, (b) PF, (c) sACCf (c), and (d) Bdy of the ACC derived in recent studies. Thin black lines indicate the 2,500 m isobath.

Table 4. Circumpolar Mean Latitude (°S) for Fronts and Southern Boundary of the ACC from Different Studies.

	SAF	PF	sACCf	Bdy*
This Study	−50.05	−54.49	−58.92	−60.50
Gille [1994]	−49.76	−53.04	–	–
Orsi et al. [1995]	−51.28	−54.93	−59.23	−60.79
Sokolov and Rintoul [2009a]	−50.84	−55.07	−60.23	–
Böning et al., [2008]	−48.70	−51.51	–	–
Sallée et al. [2008]	−51.12	−54.22	–	–

* only for regions between 60°W−140°W.

The mean frontal locations from all other studies show relatively good agreement with ours, especially in the vicinity of large topographic features (Figure 5.2). All of them show the SAF (Figure 5.2a) extending along the northern side of the Southeast Indian Ridge (100°E−150°E) and crossing the Pacific-Antarctic Ridge through the Eltanin Fracture Zone; the PF (Figure 5.2b) passing through the Udintsev Fracture Zone (135°W−155°W); and the sACCf (Figure 5.2c) and Bdy (Figure 5.2d) extending together parallel to the northern flank of the Southwest Indian Ridge (10°E−30°E) and southern flank of the Pacific-Antarctic Ridge (160°E−150°W).

The new frontal paths from this study are also significantly distinct at several locations. Southeast of the Campbell Plateau (180°), and in agreement with *Böning et al.* [2008], the SAF extends northeastward along the steep continental slope before

returning south from about 50°S, and continuing eastward to the Eltanin Fracture Zone; whereas most other studies place its path farther south near 57°S. The strong topographic constraint on our SAF path is compatible with hydrographic observations from the Eltanin Cruise 50 along 170°E. Just south of the Campbell Plateau Escarpment *Gordon* [1975] depicts the start of the northward diving of the AAIW salinity minimum, i.e. the traditional indicator of the SAF location. Independent regional studies have traced the SAF path using SST indicators, e.g. the 8°C−8.5°C isotherms [*Uddstrom and Oien*, 1999], or following deep current jets in numerical simulations [*Tilburg et al.,* 2002], and they also show the SAF northward deflection steered by the Plateau. *Budillon and Rintoul* [2003] did not rule out the SAF having two branches in this particular region.

On the northern flank of the Kerguelen Plateau, the path of the SAF in the selected studies appears tightly constrained by such prominent topographic feature. Nonetheless, a few regional studies based on in-situ hydrographic observations have also shown different spatial distributions [*Sparrow et al.,* 1996*; Roquet et al.,* 2009*; Park et al.,* 2008]. To partly understand complex discrepancies in the climatological locations of the SAF one must also contemplate that ACC jets undergo substantial seasonal fluctuations, and likely also long-term spatial drifts.

Poleward (equatorward) excursions of ACC fronts are favored during the summer (winter) of recent (earlier) decades, with the PF showing the most remarkable temporal variability. Inspection of monthly-mean altimetry data (Figure 5.7a) reveals that the PF is located south of Kerguelen Island (70°E) during the austral summer

(December to May), but it switches to north of the Island during the austral winter (June to November). Yearly-mean traces (Figure 5.5a) indicate that the PF was located to the north of the Island until 1996, similar to the mean PF path in *Orsi et al*. [1995], but thereafter to the south of the Island (Figure 5.5). *Sokolov and Rintoul* [2009] also described the local bifurcation of the PF, although suggesting a much larger meridional drift than shown in this study.

The path of the sACCf through this KP region from previous studies shows a remarkable meridional discrepancy of about 10°. *Orsi et al.* [1995] show the sACCf passing through the Princess Elizabeth Trough based on the 1.8°C indicator of the temperature maximum layer. In this study, as in *Sokolov and Rintoul* [2009a] and studies of recent high-resolution hydrographic surveys [*Park et al.,* 2009], it is suggested that the sACCf extends through the Fawn Trough separating the Southern and Northern portions of the KP.

High correlation between SSH and in-situ based indicators of ACC frontal locations is found within the entire circumpolar belt, therefore warrantying the study of their spatial and temporal variability, as shown in the next section.

5.2 Spatial Variability

Figure 5.3 shows how often, at any give grid point location, the particular frontal SSH streamline pass through over time. It reveals that spatial and temporal variability of ACC fronts are primarily determined by the underlying bottom topography. Over prominent topographic features like mid-ocean ridges, arcs and plateaus, circumpolar

streamlines tend to be persistently aligned within narrow bands. The local expressions of ACC fronts are usually enhanced, i.e. showing relatively larger gradients and lower temporal variability. Fracture zones within the Pacific sector represent effective cross-ridge gateways and means of exchange between ocean basins. Sharp expressions of the SAF and the PF are observed to squeeze through the narrow Eltanin and Udintsev Fracture Zones. Similarly, the sACCf passes through the narrows of the Fawn Trough between the southern and northern banks of the KP. Along mid-ocean ridges frontal streamlines also display relatively fixed pathways. Along the northern flank of the Southwest Indian Ridge (0°−30°E) the sACCf is estimated to appear up to 50% of the time with currents of about 15 cm/s at 1,000 m, and similarly along the southern flank, the Bdy appears up to 40% of the time. Intensified currents associated to the sACCf and Bdy are also observed along the Pacific Antarctic Ridge (150°W−180°W). Prominent obstacles and barriers to eastward flow of the ACC are the South Scotia Arc, the Kerguelen Plateau, and the Campbell Plateau. Such topography disturbs and steers the path of the entire ACC sharply to the north to conserve potential vorticity. The tight SAF looping at the western rim of the Argentine Basin (60°W−54°W) appears as a jet with currents larger than 25 cm/s appears up to 80% of time, i.e. the most recurrent current core with also the lowest variability.

At the wake of large topographic features the spatial variability of ACC jets is larger over broader bands showing significantly lower reoccurrence rates. These regions are favorable to produce mesoscale eddies through eddy mean-flow interactions

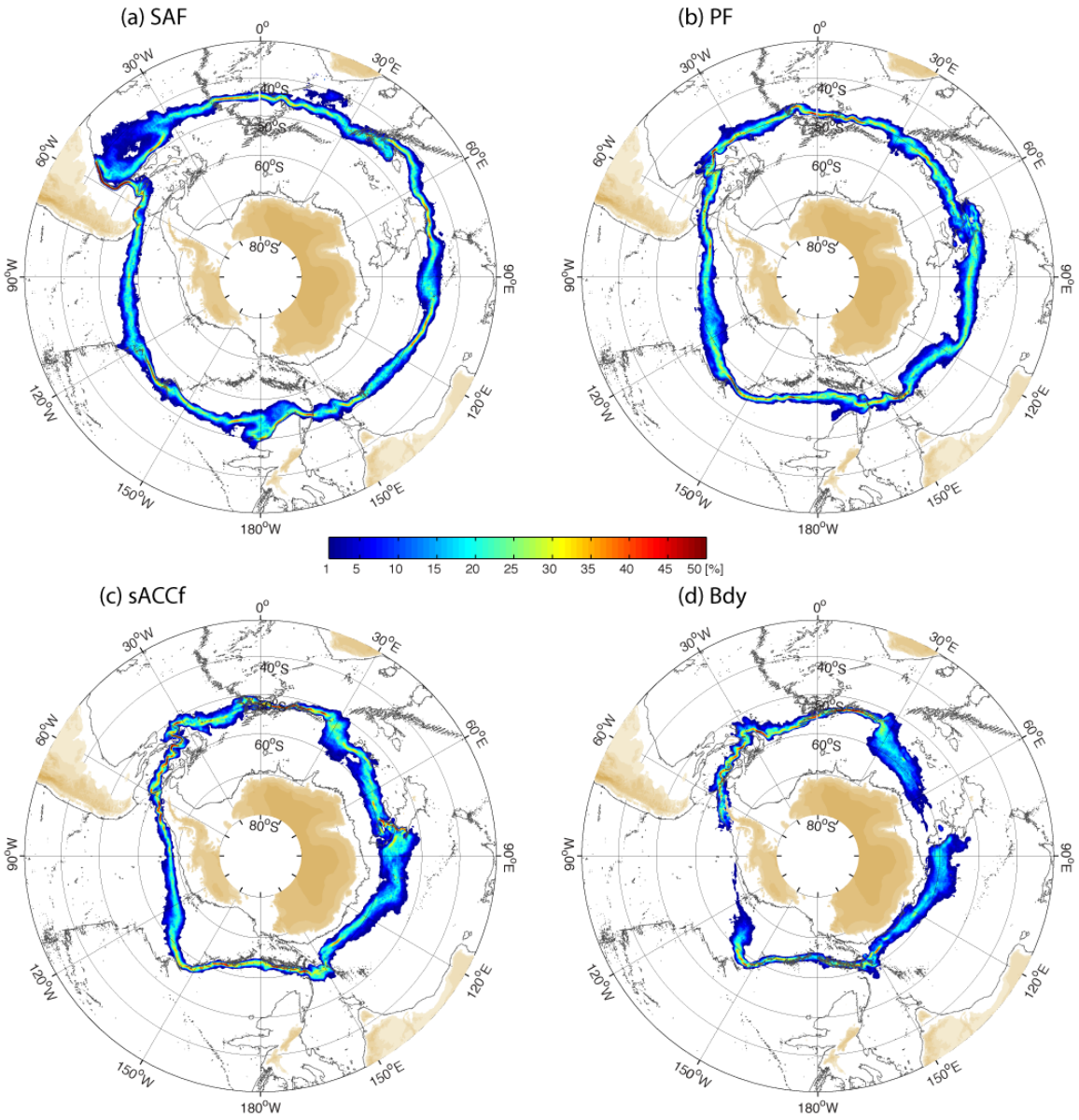

Figure 5.3. Reoccurrence in percentage of time for the (a) SAF, (b) PF, (c) sACCf, and (d) Bdy at each grid point. Thin black lines indicate the 2,500 m isobath.

[*Wilkin and Morrow,*1994*; Hogg and Blundell,* 2006]. Basically the baroclinic instability energy extracted from the mean flow is frequently released downstream through mesoscale rings, which in turn effectively control the meridional location of fronts. Over abyssal plains fronts are relatively free to meander and expected to have the largest spatial variability, as illustrated in Figure 5.3. Their meridional location may be the result of more complex and highly nonlinear interactions between external atmospheric variability, e.g. including wind stress, buoyancy forcing and sea ice extent.

5.3 Temporal Variability

5.3.1 Decadal trends

To infer temporal variability in the ACC frontal distribution, indicator SSH streamlines are traced on a weekly basis around the circumpolar belt, and their zonal average latitudes are subtracted to construct the weekly time series of meridional displacement shown in Figure 5.4.

Linear fits to weekly frontal displacement data, shown as green straight lines in Figure 5.4, reveal significant trends of poleward progression in the location of all ACC fronts during the past nineteen years. The estimated drift of the mean (circumpolar) position of the sACCf is 46 km to the south, whereas smaller drifts are inferred for the PF (28 km), and the SAF (30 km). All estimated poleward drifts in the ACC fronts are statistically significant ($p < 0.01$), based on student's t tests that incorporate the autocorrelation inherent to the time-series [*Bretherton et al*., 1999], and of magnitudes similar to suggested displacements in previous studies [*Aoki et al.,* 2005*; Gille,* 2008*;*

Sprintall, 2008]. *Böning et al.* [2008] determined that their anomalous distribution of the SAF and PF moved about 50 km−80 km toward the south during the past 40 years due to systematic warming and freshening within the ACC domain, which leads to a deepening of subsurface (800−1000 m) isopycnal surfaces by about 50 m. *Sokolov and Rintoul* [2009b] report a 60-km poleward displacement of all the ACC fronts between 1992 and 2007, i.e. about twice as large as the total migration estimated in this study. This large discrepancy is presumably due to higher variability in their source SSH field [*Sokolov and Rintoul,* 2009a]: the range of frontal reoccurrence in this study is 1% to 50% (Figure 5.3), whereas theirs is only 0.4% to 10% (see figure 7 of *Sokolov and Rintoul* [2009a]).

The one-year low-pass filtered distribution of ACC fronts, shown as blue lines in Figure 5.4, not only reveals interannual variability but also large fluctuations identifiable in certain years. In 1998 all three fronts experienced large and abrupt poleward shifts when the positive trend of the SAM index reached its maximum, but also coinciding with one of the strongest recorded La Niña events between 1998 and 1999. Although the inferred interaction between ENSO and SAM plays an important role in determining the meridional locations of the ACC fronts [*Sallée et al.,* 2008*; Morrow et al.,* 2008], the exact relationships between ACC fronts and atmospheric variability remains unclear.

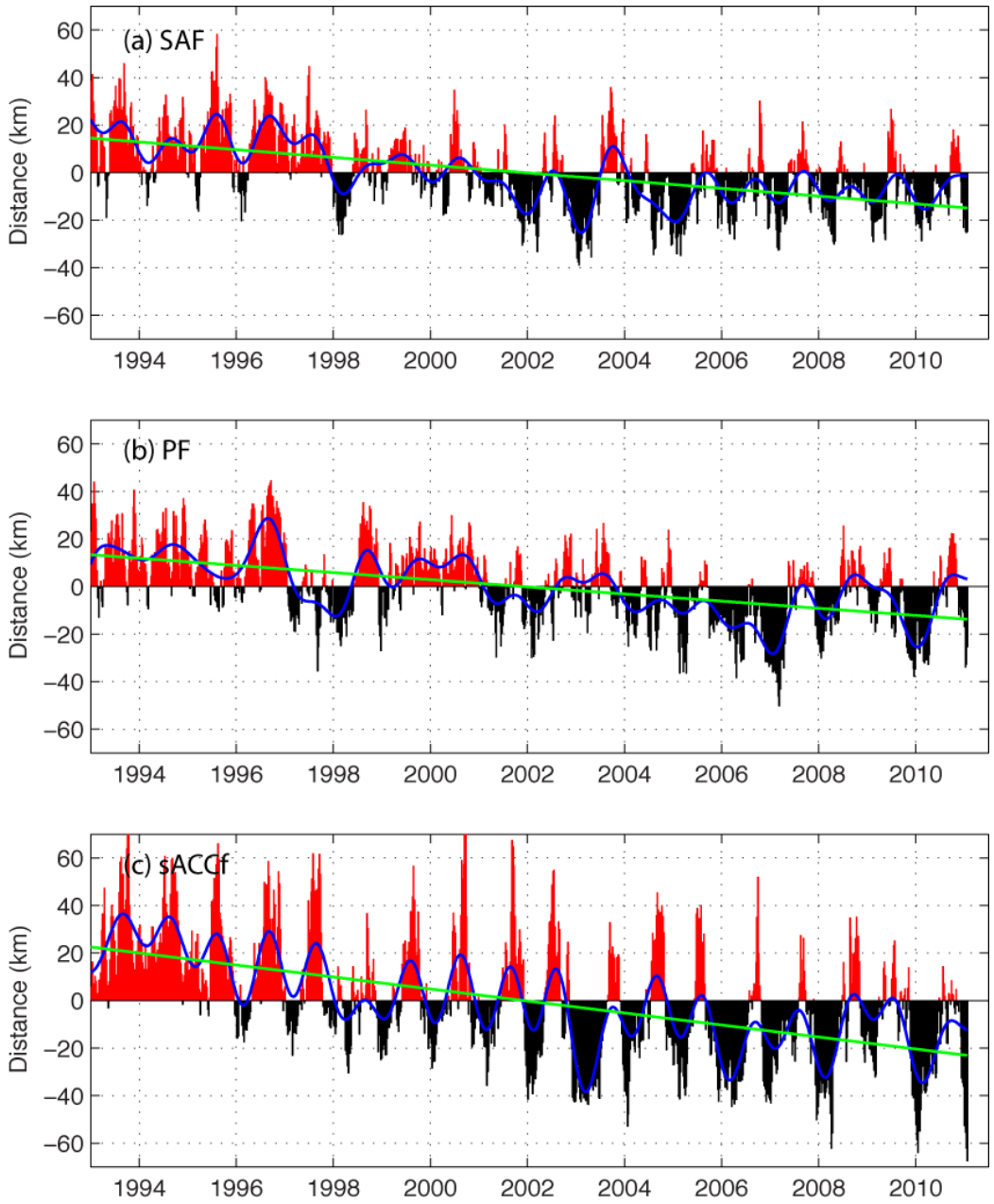

Figure 5.4. Weekly time series of the circumpolar averaged meridional distance (km) of the (a) SAF, (b) PF, and (c) sACCf from its mean position. Positive (red)/negative (black) means the frontal locations equatorward/poleward of mean path. The green lines show the linear trends, and blue lines show the data after 1-year low-pass filtering.

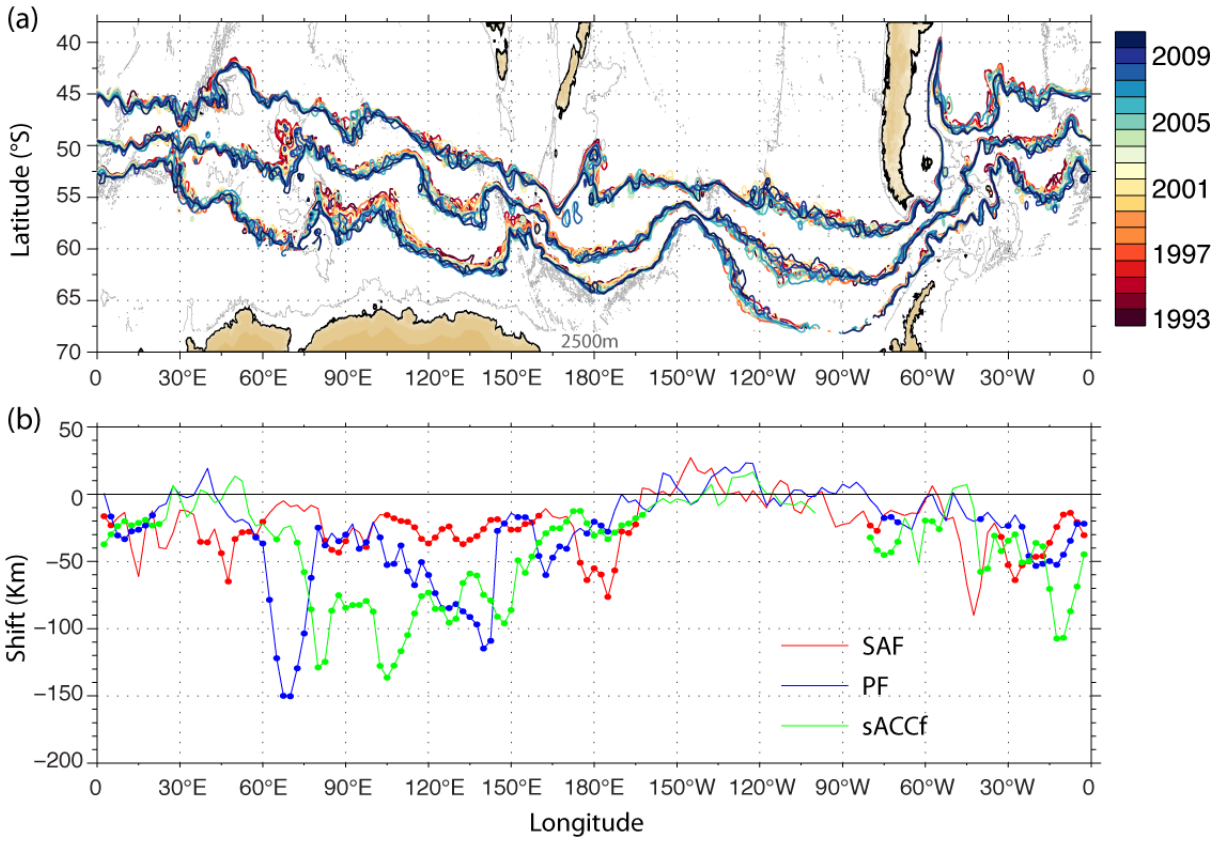

Figure 5.5. (a) Annual mean paths of the SAF, PF, and sACCf for each of the years 1993−2010, and (b) calculated total drift by assuming linear trend. Dots indicate statistically significant values above the 95% confidence level using a student t-test.

The total poleward drift of ACC fronts inferred from these estimates trends clearly shows some regional variability. Near 40°E for the PF, 50°E for the sACCf, and 150°W−120°W for the ACC fronts the annual-mean latitudes (Figure 5.5b) even migrated toward the Equator. In contrast, there is an isolated maximum (150 km) in the poleward drift of the PF over Kerguelen Plateau (70°E), even though a 7° latitude change is estimated based on annual mean frontal paths; thus frontal drifts calculated using linear fits may be largely underestimated. Such remarkable local shift in the PF

location suggests that even though frontal paths are highly constrained by the underlying topography, they may still abruptly adopt a different course over the years, even over large-scale topographic features. Another example of bimodal distributions is that estimated for the SAF along the southern flank of the Campbell Plateau, where it used to tightly follow the plateau's escarpment but in more recent years it is located much farther to the south than the mean position. A possible bifurcation of the PF path is indicated near the Maurice Ewing Bank. Analyses of synoptic hydrographic observations before 1990 placed the PF passing along the western flank of the Bank [*Orsi et al.,* 1995], but since 1992 the location of the PF has been inferred on the eastern side.

Over most of the eastern Indian sector (60°E−150°E) all fronts show substantial poleward drifts, ranging from about 100 km to 400 km. Somewhat smaller but still statistically significant, are the frontal drifts inferred downstream of the South Sandwich Trench in the Atlantic sector (45°W−20°E). In contrast, the vast eastern Pacific sector (150°W−75°W) shows a unique frontal behavior. Here, a considerable vacillation in the location of fronts is found, i.e. with no apparent linear trend, which is unexpected over abyssal plains. Everywhere else, however, the paths of ACC fronts are expected to have drifted to the south due to the sustained positive SAM index trend during the past couple of decades.

5.3.2 Seasonal variability

Seasonality in all the ACC frontal distributions is noticeable in Figure 5.4. To capture this apparent seasonal cycle more clearly, a one-year high-pass filter is applied to the circumpolar-averaged frontal locations, and the resulting time series are shown in Figure 5.6. The striking tendency is for all the ACC fronts to migrate south (north) during the austral summer (winter) months, as indicated by the red (back) meridional deflections in Figure 5.6.

The largest seasonal migration, of about 100 km, was undergone by the sACCf from the winter of 2000 to the summer of 2001, whereas a mean 42 km amplitude is derived using harmonic analysis. The SAF shows the smallest seasonal fluctuation, 18 km on average and with a seasonal maximum of 73 km, similar to the PF (20 km on average). Significant seasonality in all the ACC frontal locations may partly explain the summer bias of the distributions in *Orsi et al.* [1995], which are generally located farther to the south than those presented in this study (see Table 4).

The amplitude of this seasonal migration also varies regionally (Figure 5.7), but in most of the circumpolar regions is less than 10 km. Relatively large seasonal fluctuations in ACC fronts are indicated in the South Atlantic (55°W−25°E) and near the Kerguelen Plateau (60°E−120°E). The latter supports a local bifurcation of the PF path, where the PF passes north of the island during the summer and adopts a southern path during the longer winter months. High variability is also found in the northernmost reach of the sACCf to the east of the KP, where sea ice normally extends to as far north as the Fawn Trough [*Rintoul et al.,* 2008]. In the Atlantic sector, only the SAF shows

significant seasonal migrations, most likely induced by variability in the population of warm subtropical rings. *Matano et al.* [1998] found strong seasonality in the EKE of the South Atlantic (55°W−25°E), i.e. a summer maximum (winter minimum), with as much as 30% of the annual mean energy. Hypothetically, increased generation of northwestward-flowing warm-core rings at the Agulhas Retroflection rises SSH in the southwestern Atlantic, thus forcing the SAF to drift south in the summer.

5.3.3 Response of ACC frontal locations to SAM and ENSO indices

The cause and effect relationship between positive SAM anomalies and poleward migration of ACC fronts have been discussed in studies of historical hydrographic data [*Gille,* 2002; 2008; *Aoki et al.,* 2005; *Böning et al.,* 2008], satellite altimetry [*Morrow et al.,* 2008; *Sokolov and Rintoul,* 2009b], and numerical simulations [*Spence et al.,* 2010; *Hall and Visbeck,* 2002]. However, more complex response mechanisms are suggested by the zonal distributions of correlation coefficients between SAM and ENSO indices with the observed individual frontal displacements shown in Figure 5.8.

A prominent out-of-phase frontal response to interannual atmospheric variability is mainly found in the southeast Pacific sector (160°W–100°W). Here, the PF is consistently displaced northward (southward) during +SAM and –ENSO (−SAM and +ENSO). The similar regional and out-of-phase response was inferred from regression maps of SSTa (Figure 3.5), thus indicative of a common atmospheric forcing mechanism.

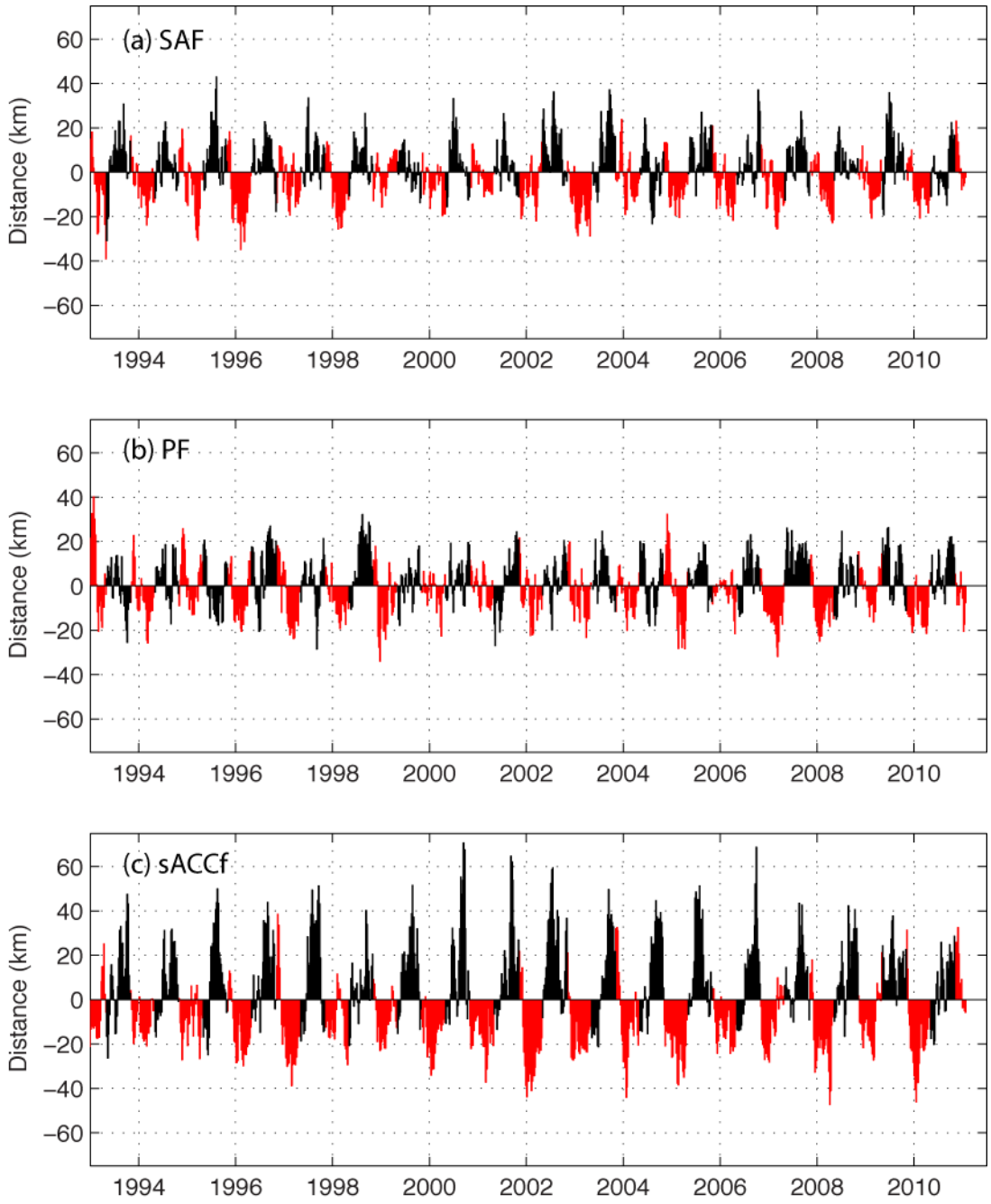

Figure 5.6. 1-year high-pass filtered time series of the circumpolar averaged meridional distance (km). Red/black indicates the austral summer (November−April)/winter (May−October).

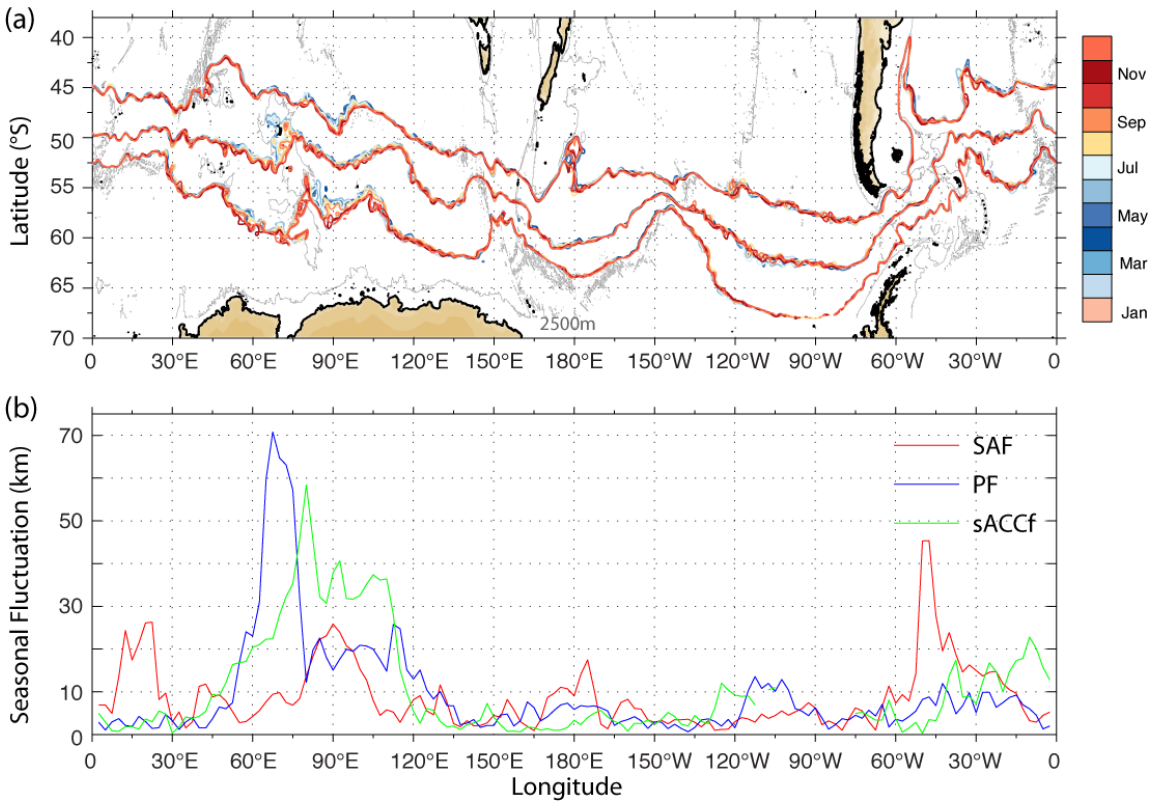

Figure 5. 7. (a) Monthly mean paths of the SAF, PF, and sACCf during 1993 and 2010 and the (b) amplitude of seasonal oscillations calculated using the Fast Fourier Transform analysis.

Since a −SLPa extends to mid latitudes in the Pacific sector, it renders a quite asymmetric SLP field that induces anomalous meridional circulation. If a +SAMa occurs in addition to the –SLPa, the latter will remain centered at 100°W, a configuration that leads to anomalous equatorward (poleward) winds on the western (eastern) side, i.e. between 140°W–100°W (100°W–75°W). Simultaneously, a weak +SLPa remains fixed in the Indian Ocean, leading to anomalous poleward (equatorward) winds in the eastern (western) sector.

An example of anomalous atmospheric circulations associated with SAM (red line in Figure 5.8) are the equatorward (poleward) winds to the west (east) of a −SLPa that deflect the ACC fronts to the north (south) in the eastern Pacific sector. Anomalous poleward (equatorward) winds found to west (east) of the +SLPa; i.e. between 30°E and 60°E (150°E–165°W), lead to the observed southward (northward) bend of the local paths of the PF and sACCf. The SAF is less responsive to the +SLPa in the Indian and in the west Pacific sectors than the other ACC fronts, thus also more insensitive to interannual variability in large-scale atmospheric forcing, because it extends side by side to the Indian-Atlantic supergyre.

Frontal location variability associated with ENSO variability is highly localized in the central Pacific sector. Here a +SLPa, similar to that seen during a −SAM, induces a southward (northward) drift of ACC fronts in the southwest Pacific (Drake Passage). The higher correlation between frontal fluctuations and the ENSO index, compared to SAM's, suggests a more dominant role in the south Pacific. ENSO strongly influences the position of the PF, but there is a sharp correlation drop near 140°W, where the passage of the PF through the Udintsev Fracture Zone is more strongly controlled by the prominent local bottom topography. Weak ACC frontal responses are also found over other fracture zones, plateaus, and ridges.

A closer inspection of the patterns shown in Figures 5.5b and 5.8 reveals that the poleward drift of ACC fronts downstream of the KP (70°E–150°E) have relatively low to insignificant correlations with atmospheric forcing. This indicates that at least in this region the observed oceanic response cannot be induced solely by atmospheric

variability. In contrast, the central Pacific sector (150°W–60°W) shows considerable frontal vacillation, right where the most noticeable oceanic responses (SLPa and SSTa) to atmospheric forcing are found.

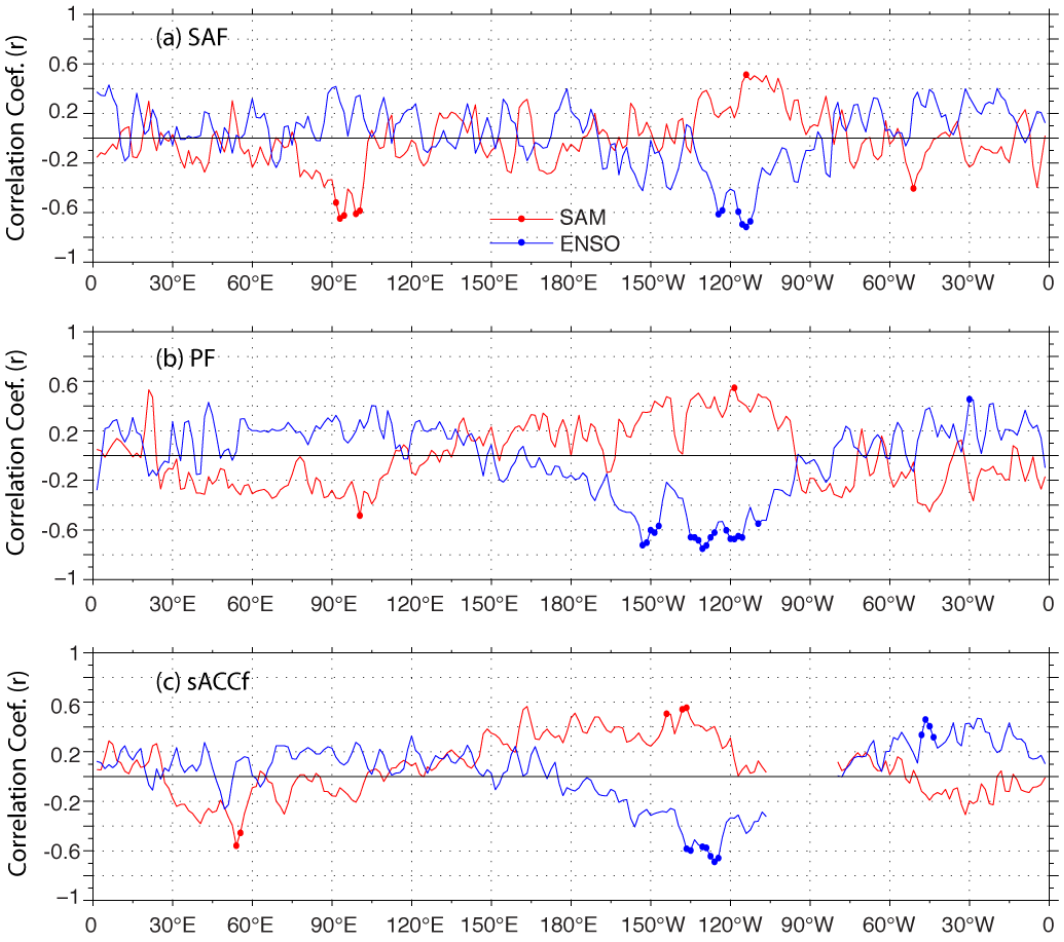

Figure 5.8. Zonal distribution of correlation coefficients between meridional fluctuations (1-year low-pass filtered) of ACC fronts with SAM (red) and ENSO (blue) indices; large dots indicate values statistically significant above the 95% confidence level using a student t-test; positive (negative) correlation indicates northward (southward) displacement of fronts in response to interannual atmospheric variability forcing.

CHAPTER VI

MESOSCALE EDDY FIELDS IN THE SOUTHERN OCEAN

6.1 Introduction

The great importance of mesoscale rings in the Southern Ocean has been revisited in recent studies of their role in the ACC cross-frontal exchange of subtropical and subpolar regime waters [*Morrow et al.,* 2004], and as in the transfer of wind-induced momentum to the ocean interior. Intensified westerly winds would excite mesoscale activity within the ACC domain; they would also drive a larger divergence (convergence) of Ekman transport to the south (north) of the wind stress maximum, which in turn would result in steeper tilting isopycnals within the interior of the ACC. Such excess in available potential energy could support the generation of more vigorous or more frequent eddy activity with a certain time lag, effectively transferring momentum downward through interfacial form stress [*Meredith and Hogg,* 2006]. Evidence of enhanced eddy activity in the ACC has been reported by a number of recent studies [*Meredith and Hogg*, 2006; *Böning et al*., 2008; *Screen et al.*, 2009; *Liu and Curry*, 2010].

By analyzing hydrographic data from the past 40 years, *Böning et al*. [2008] could not find any significant increase in the meridional slope of ACC isopycnals, suggesting that enhanced Ekman transport is sufficient to compensate for the larger eddy flux of momentum from the winds, and therefore bear little effect on the total volume transport of an eddy saturated ACC regime [*Meredith and Hogg,* 2004]. Recent

numerical simulations [*Karpechko et al*., 2009; *Screen et al*., 2009; *Spence et al.,* 2010] have also accentuated the importance of resolving mesoscale eddies by reducing model grid spacing: higher-resolution models were able to release the stored potential energy by producing eddies rather than enhancing the ACC transport, as coarse-resolution model tend to do (e.g., *Hallberg and Gnanadesikan*, 2006; *Russell et al.,* 2006; *Farnetti et al.*, 2010; *Gent et al.*, 2011).

Steeper isopycnals, through the geostrophic relationship, would lead to an increase in the total volume transport of the ACC. Volume transport estimates through Drake Passage based on direct bottom pressure measurements [*Hughes et al.,* 1999*; Meredith et al.,* 2004] and low-resolution climate models [*Hall and Visbeck*, 2002; *Fyfe and Saenko*, 2005; *Saenko et al.*, 2005; *Sen Gupta and England*, 2006] suggest a linear relationship to the wind stress, therefore predicting an increase in the ACC transport as a result of the recent upward trend in the SAM index. This is the typical response to wind anomalies by a buoyancy-dominant Southern Ocean regime. Curiously, studies of the Simple Ocean Data Assimilation (SODA) reanalysis dataset by *Yang et al.* [2007] found a significant correlation between ACC transport and the SAM index, but with no linear trend.

In this chapter, I discuss the spatial distribution and temporal variability of mesoscale eddies in the Southern Ocean, and their relationship to variability in the atmospheric forcing.

6.2 Method

To identify individual mesoscale eddies in the 19 years of SLA data (1992−2011), I used a simple threshold criteria of ±20 cm SSH anomalies, thus only selecting long-lifetime and energetic rings and disregarding noise signals. This threshold method has been successfully applied in the Drake Passage [*Joyce et al.,* 1981*; Sprintall,* 2003*; Barré et al.,* 2011], and in the Southeast Indian [*Morrow et al.,* 2004; *Swart et al.,* 2008a], albeit with some limitations due to significant seasonal fluctuations and linear trends in SLA. A larger number (fewer) of anticyclonic (cyclonic) eddies with SLA > 20 cm (<−20 cm) are identified as time progresses and Southern Ocean sea level rises at a rate of 3.1 mm/yr. Similarly, the seasonality in SLA increases (decreases) the number of anticyclonic (cyclonic) eddies during the summer (winter) months. The long-term trend and annual cycle calculated using FFT analysis are removed from the SLA data to minimize these biases, prior to the ±20 cm threshold used to identify rings with at least ~30 km radius.

Figure 6.1 shows processed SLA data for the days when an extreme number of particular types of mesoscale eddies were identified. The maps with the most abundant warm (17 December 1997) and cold (27 October 2010) rings readily illustrate that the most energetic (EKE) regions of the Southern Ocean are well represented by detected mesoscale rings using a 20 cm threshold in SLA. Automatic ring-tracking techniques, although useful to study the behavior of individual rings, are beyond the scope of this study.

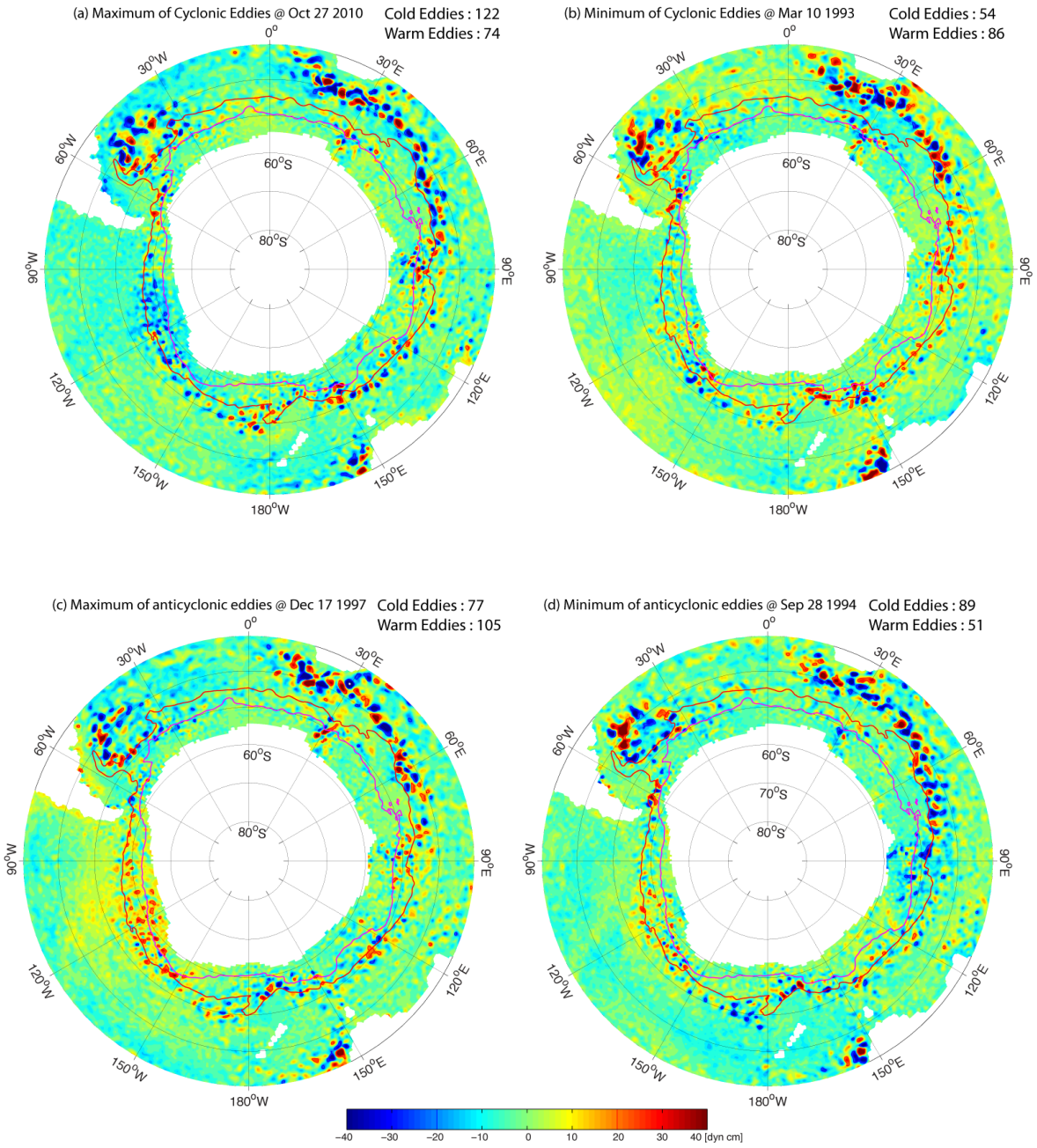

Figure 6.1. Maps of SSH on days with a particular extreme number of mesoscale rings, (a) 27 October 2010 and (b) 10 March 1993 with the maximum and minimum number of cold cyclones, and (c) 17 December 1997 and (d) 28 September 1994 with the maximum and minimum number of warm anticyclones; the total number of each type of rings are shown for each panel. The red and magenta circumpolar contours represent the climatological altimetry-based distribution of the SAF and PF.

6.3 Results

6.3.1 Spatial distribution of mesoscale eddies

On average between 1992 and 2011, a daily total of 79 warm anticyclones and 88 cold cyclones were identified south of 30°S. The slight dominance of cyclones agrees with *Chelton et al.* [2011] results based on detection methods independent of SSH thresholds. Maps of mesoscale eddy reoccurrence (Figure 6.2) reveal regions with the highest frequency of rings, both cold and warm types, mainly along and downstream of the three subtropical western boundary current systems. The Agulhas Retroflection region, in particular, showed mesoscale eddied during up to 30% of the total altimeter measurements period. Within the domain of the ACC, regions of high reoccurrence of rings are to concentrate downstream of large topographic features.

Regional excess of baroclinic energy is gained from non-zonal surface motions, e.g. large meanders develop when ACC fronts interact with prominent topographic features, and release to the ocean interior through localized generation and pinching off rings. Therefore these areas are pivotal conduits for mid to high latitude eddy transport of heat, salt, and nutrients across the ACC. The most notorious conduits are found immediately downstream of: the 30°E gap in the Southwest Indian Ridge, the Kerguelen Plateau (80°–100°E), the gap between the Tasmania Rise and Southeast Indian Ridge (145°E), the Macquarie Ridge−Hjort Trench (160°E–175°E), the Eltanin−Udintsev near (145°W–120°W), and the Falkland Ridge near 25°W (Figures 6.2−6.3). E.g. the triangular-shaped area (Figure 6.2) centered between Del Caño Ridge and Conrad Rise is

well known for its enhanced variance in the SLA [*Swart et al.,* 2008a*; Ansorge and Lutjeharms,* 2003], and the frequent meandering of the SAF and PF. Locally generated cyclonic eddies carry cold, fresh AASW from the Antarctic Zone along the southern flank of Crozet Ridge, and injected it to the subtropical Indian Ocean. Likewise, anticyclonic eddies carry warm, salty SASW southeastward [*Ansorge and Lutjeharms,* 2003], leading to the observed anomalous warming in this region.

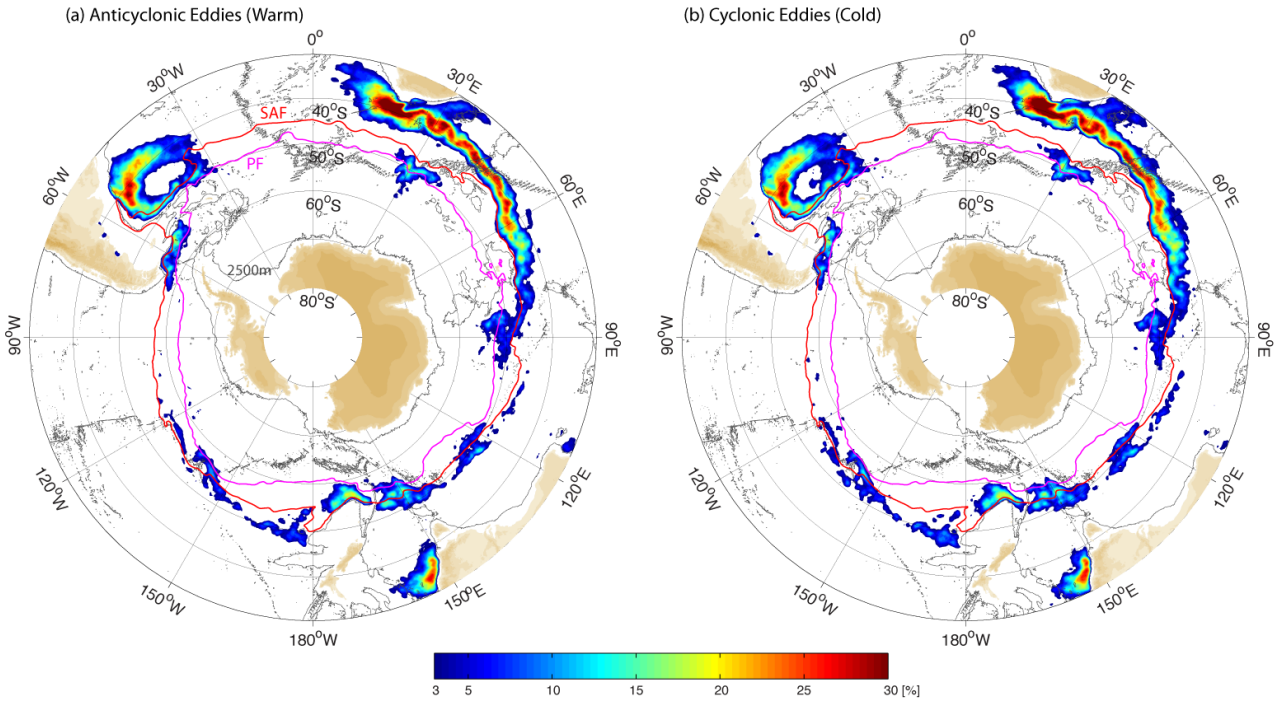

Figure 6.2. Maps of reoccurrence, in percentage of time span, (a) anticyclonic and (b) cyclonic eddies. The red and magenta circumpolar contours represent the climatological altimetry-based distribution of the SAF and PF.

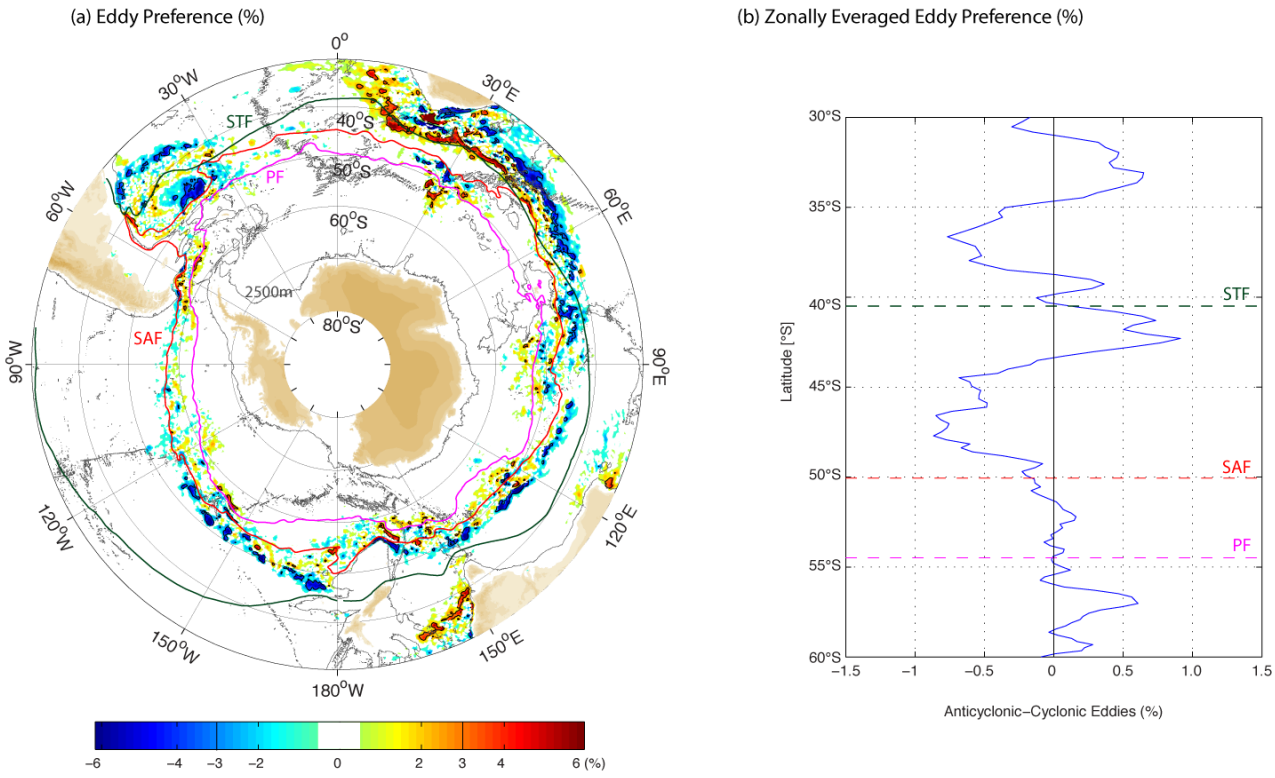

Figure 6.3. (a) Map and (b) zonally averaged profile of eddy type dominance, calculated as the difference between the reoccurrence of anticyclonic and cyclonic eddies. The red and magenta circumpolar contours represent the climatological altimetry-based distribution of the SAF and PF from this study, whereas the green line is the STF trace from *Orsi et al.* [1995].

The band of maximum ring occurrence seen along the Agulhas Return Current (ARC) extends to near 72°E [*Belkin and Gordon*, 1996]. *Lutjeharms and Ansorge,* [2001] suggest that near 66°E–70°E there is a relatively larger number of rings detach from the ARC, thus more effectively transferring heat and salt from the subtropical Indian to the northern ACC [*Sallée et al.,* 2006]. This eddy conduit explains the

observed warming (SSTa), sea level rise trend, and poleward migration of ACC fronts downstream of the KP.

Another well-known area of relatively high eddy activity is near the Falkland Gap [*Whitworth et al.*, 1991], where the SAF and PF converge (Figure 4.8). Cold rings injected to the Argentine Basin at this site propagate northward along the western side of the Zapiola Rise Anticyclone, whereas warm rings from the BMC move southward along the eastern limb [*Fu,* 2006].

Figure 6.3a shows the domains of prevalence for anticyclonic (red) and cyclonic (blue) eddies, as the difference between the corresponding reoccurrence (Figure 6.2). Both, the Subantarctic Zone (SAZ) and the Subtropical Zone (STZ) south of 30°S, reveal the same pattern of alternating eddy prevalence: anticyclonic (warm) rings prevail at the northern band, switching to cyclonic (cold) rings prevalence in the southern band. This pattern is more apparent in the zonally-averaged distribution of Figure 6.3b: these two zones incorporate relatively more anticyclones from the north and cyclones from the south.

The zonal distribution of eddy-type prevalence (Figure 6.4) shows a rather localized nature of cross-frontal exchange. The pattern for the entire region south of 30°S (Figure 6.4a) is almost entirely controlled by exchanges within the band to the north of the SAF (Figure 6.4b), which in turn reflects the influence of the most vigorous and persistent anticyclones generated along the subtropical western boundary currents. Preference for anticyclones (0°–30°E) coincides with the Agulhas Retroflection Current, whereas cyclones associated with the ARC dominate

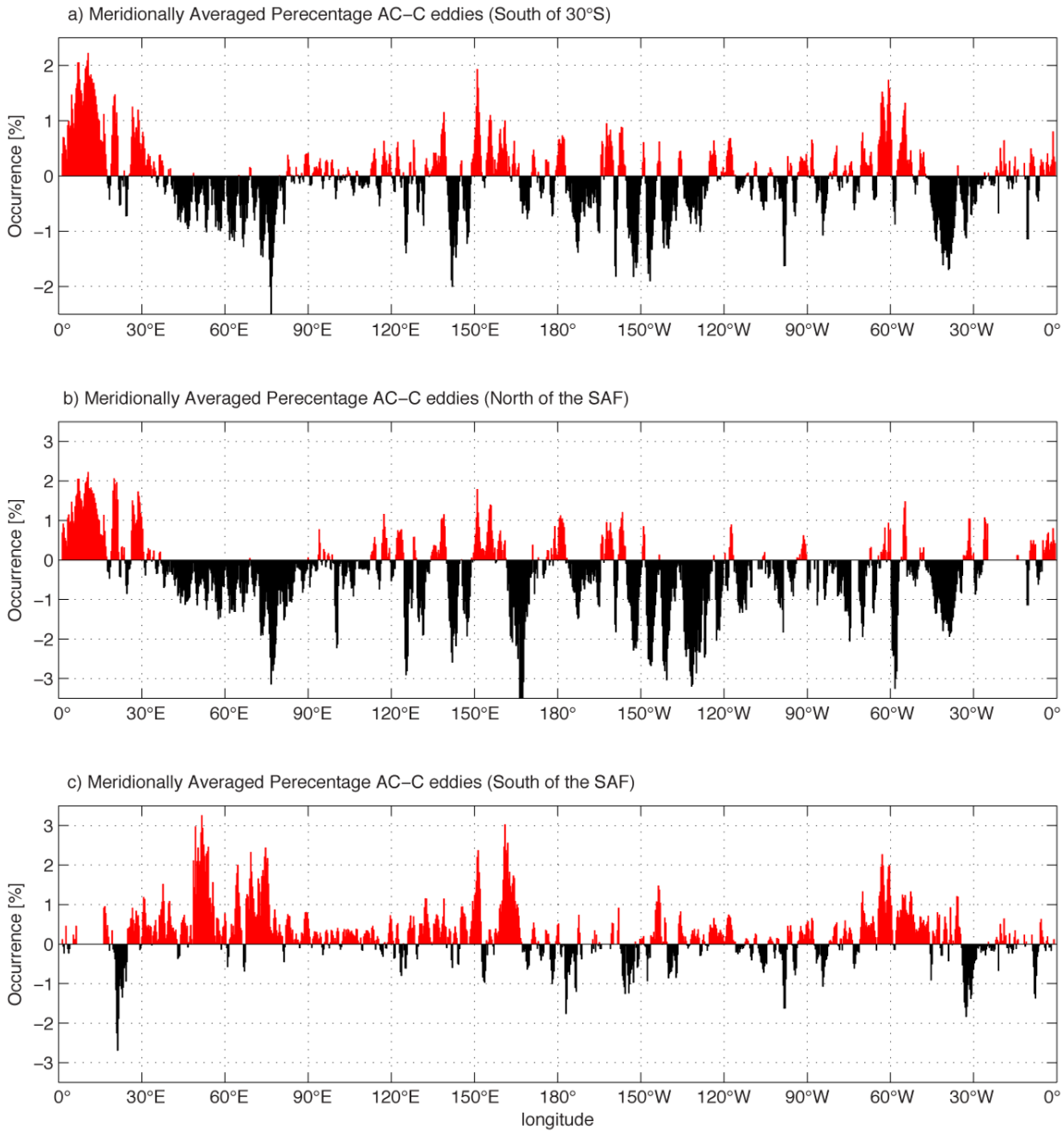

Figure 6.4. Meridionally averaged eddy preference for (a) the Southern Ocean (south of 30°S), (b) the subtropical regions (north of the SAF), and (c) within the ACC (south of the SAF).

between 40°E and 80°E. Anticyclones are predominant in the BMC zone (60°W), whereas cyclones prevail within the Zapiola Anticyclone (40°W).

In general, warm anticyclonic eddies dominate the ACC domain (Figure 6.4c), most likely due to the incorporation of relatively warmer subtropical rings.

6.3.2 Temporal variability in the number of eddies

Since the seasonal cycle and linear trend have been removed from the time series shown in Figure 6.5, the remaining signals are mainly due to interannual variability in the atmospheric forcing. Satistical analysis of the 1-year low-passed filtered data sets reveals links to +SAM with a 21-month lag, an overall correlation coefficient of 0.45, and marginally significant at the 90% confidence levels. It is estimated that a peak in the number of eddies most commonly occurs about 2 years after a peak of +SAM index, consistent with the increase in annual-mean EKE in an eddy-permitting simulation of satellite altimetry data [*Morrow et al., 2010*]. The number of anticyclonic eddies is insensitive to the ENSO index. Enhanced momentum at the sea surface is slowly (~ 2 years) transferred downward through interfacial stress to the ocean floor, where rings are generated by topographic interaction with strong currents [*Meredith and Hogg,* 2006*; Hogg et al.,* 2008*; Screen et al.,* 2009]. A similar but inverse correlation (r= −0.52) between number of cyclonic eddies is found to ENSO with a quasi-instantaneous response (3-month lag). It is hypothesized that if a strong La Niña event occurs after a robust +SAM anomaly, the eddy field is amplified, e.g. there were prominent peaks in

the number of rings identified during 2000 and 2001 and the overall maximum was in 2010.

In the south Pacific, out-of-phase oceanic responses to SAM and ENSO have been found both in SSTa (Figure 3.5) and in frontal locations (Figure 5.8). The extreme population of cyclones (Figure 6.1a,b) within the ACC (150°W–60°W), i.e. the 21 (4) cold rings detected on 27 October 2010 (10 March 1993), points to another pivotal conduit for the exchange of waters between middle and high-latitudes.

Increase in concurrent +SAM anomalies and La Niña events will export more cyclonic eddies to the Subantarctic Zone (SAZ), thus further cooling, freshening, and lightening the SAMW. *Garabato et al.* [2009] conclude that southeast Pacific SAMW has undergone cooling and freshening trends due to the shutdown in production of AAIW during 1998/99, a period that coincides with the estimated rapid increase in both the number of cold rings exported northward and concurrent northward Ekman transport.

In contrast, the population of anticyclonic eddies (Figure 6.5b) increased from 1994 to 2000 and remained relatively constant thereafter, and there is a lack of any significant correlation and weak cross-correlation with the atmospheric indices. Therefore the population of warm eddies seems insensitive to the atmospheric forcing.

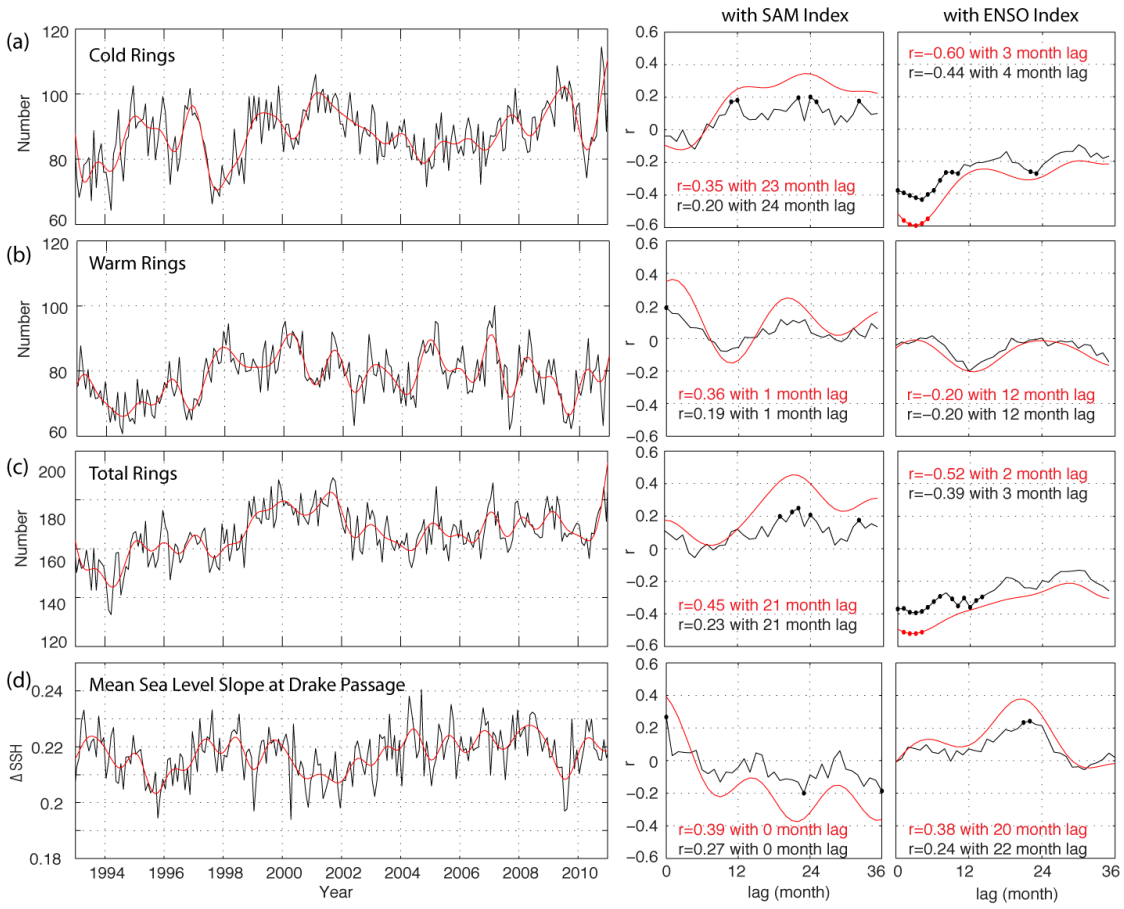

Figure 6.5. Monthly population of (a) cyclonic, (b) anticyclonic, (c) total eddies, and (d) mean sea level slope at Drake Passage over time, with 1-year low-pass filtered time series overlaid (red line); and their corresponding lagged correlation to SAM and ENSO indices are shown on the right. Red (black) dots are correlations above 95% (99%) confidence levels. The highest correlation coefficients (r) are indicated with their corresponding lags.

CHAPTER VII

SUMMARY AND CONCLUSIONS

The goal of this research is to elucidate some aspects of the linkages between dominant atmospheric modes of interannual variability and the observed responses in the Southern Ocean during the past few decades. New estimates and descriptions of the spatial and temporal variability in sea surface properties (SSTa, SLPa), frontal distributions, and mesoscale eddy activity are presented to address these objectives. These oceanic responses time series are analyzed to establish the extent of interdependence with SAM and ENSO variability. Improved understanding of teleconnections between mid-latitude processes and varying Southern Ocean circulation and stratification will render new ground for their accurate representation in global climate models.

7.1 Atmospheric Forcing

Main trends in Southern Hemisphere atmospheric variability over the past five decades have intensified circumpolar westerly winds (+SAM anomaly), and increased the frequency and intensity of anomalous warming in the eastern tropical Pacific (bipolar ENSO events). The Pacific Ocean responses are similar and localized, but with an out-of-phase relationships: amplified (cancelled) during concurrent +SAM anomalies and a La Niña (El Niño) events. This explains, e.g., the extreme La Niña event of 1999/2000,

when high-latitude cooling and poleward drift of ACC fronts were the largest, and the largest increase in eddy population the following year (2000/2001) as a delayed response.

7.2 Oceanic Responses

7.2.1 SST

The persistent mid-latitude trends of SST warming (0.16°C/10yr) and SL rise (3.6 cm/10yr) are in sharp contrast to the highly fluctuating responses in the Southern Ocean, superimposed to only negligible cooling (−0.03°C/10yr) and slower rising (2.2 cm/10yr) trends. Whereas concurrent out-of-phase SSTa and SLPa between high and mid latitudes are induced during +SAM over the past three decades, the 1998/1999 +SAM maximum showed highly fluctuating oceanic responses. Furthermore, the observed warming of subtropical gyres exceeds SAM's regression, and could be partly explained by oceanic processes. A likely candidate mechanism supported by results from this study is the intensification of the Indian-Atlantic 'supergyre' due to anomalously warming at the western boundary current systems.

Southern Ocean SST has progressively cooled during the past three decades, and at a faster rate in recent years. Furthermore, the long-term cooling has not been monotonic either: period of large and rapid SST warming were observed during 1991–1992 and 2000–2001. Both reversals are attributed to the magnified contribution of concurrent –SAM and +ENSO.

The Pacific sector shows the largest cooling rates in the Southern Ocean, whereas warming has been more extreme in the Indian sector. Whereas the former cooling is due

to localized atmospheric forcing in the Pacific, enhanced poleward heat flux in the Indian is attributed to a large number of anticyclonic eddies shed at the ARC that enter the ACC regime downstream of the Kerguelen Plateau, causing the observed SST increase of 0.5°C in the last three decades. Southeast Pacific SSTa and SLPa drift within the ACC and reach Drake Passage two years later, influencing the overall slope of the sea surface and total volume transport across the Passage. The two-year lag between either +ENSO or –SAM, and the positive sea surface slope anomaly at Drake Passage indicates that the Pacific sector is a buoyancy-dominated regime.

7.2.2 ACC fronts

Specific contours of SSH are found to closely follow multiple bands with maxima SSH slope in the southwestern Atlantic Ocean. Inspection of a series of concurrent CTD lines, Argo floats, surface drifters, and results from several recent studies, all confirm their correspondence to the location of ACC fronts, namely the SAF, PF and sACCf, in the southwestern Atlantic Ocean. Further validation of the selected altimeter streamlines as ACC frontal indicators was achieved through the analysis of traditional property indicators and location of currents core.

Overall the global ACC frontal distributions based on altimetric data derived in this study are very similar to the classical maps in previous studies [*Orsi et al.,* 1995*; Sokolov and Rintoul,* 2009a*; Sallée et al.,* 2008]. This indicates that the underlying bottom topography exerts the most influential control on the location of ACC fronts.

Fronts appear to be fixed, sharpened and the associated currents intensified at locations with major bathymetric features.

Additional non-circumpolar current cores are apparent over some regions of the Southern Ocean, in particular where ACC fronts experience complex interactions with adjacent current cores, convergences and divergences, and mesoscale rings. Large discrepancies with previous frontal distributions are commonly observed over abyssal plains, where topographic influence is the least. Other significant differences are noticed over seamounts, where a particular front seems to follow paths on opposite sides or even due to slight changes in atmospheric forcing. The most prominent change in frontal paths found is that for the PF around Kerguelen Island: to the north (south) of the Island during winter (summer) months, and in earlier (most recent) of the 20-year period examined in this study. Abrupt shifting in frontal positions correspond to the frequent splitting of fronts encountering prominent topographic features.

All of the SSH streamlines indicative of ACC frontal locations reveal a seasonal oscillation with northward (southward) winter (summer) migrations. This study also shows that circumpolar-mean frontal positions have monotonically drifted southward since 1992: the sACCf by ~46 km, while both the PF and SAF by ~30 km. Interannual variability in the atmospheric forcing has likely influenced the major southward migration of ACC fronts between 1997 and 1999, but more evident is the different regional responses to the two major modes of interannual atmospheric variability: from a clear poleward drift in the southeastern Indian (70°E−150°E), to a weak drift in the

central Atlantic (30°W−30°E), and no drift but high vacillation in the south Pacific (150°W−75°W) and southwestern Indian (30°E−60°E).

It is postulated in this study that there are two regional mechanisms determining the ACC frontal response to atmospheric interannual variability. One is the large vacillation in frontal locations with no linear trend that results from the interaction between the SAM and ENSO indices. In the Pacific such response is characterized by being out-of-phase. Thus, the main atmospheric forcing controlling factor is the anomalous winds induced by SLPa. Meridional location of fronts is statistically correlated to ENSO and SAM. The second response is the significant poleward drifting of ACC fronts insensitive to atmospheric variability, thus ruled by regional oceanic influences. E.g. high eddy heat flux downstream of the KP drives the major polar drift of ACC fronts in the Indian sector.

7.2.3 Mesoscale eddies

Oceanic response to interannual variability in the atmospheric forcing includes the adjustment of the mesoscale eddy population. The total number of identified rings in the Southern Ocean systematically increased, albeit with a delay of two years, during periods of +SAM,, but it also has decreased on much shorter notice during +ENSO. These results confirm simulations from eddy-resolving numerical model studies [*Meredith and Hogg,* 2006*; Screen et al.,* 2009*; Morrow et al.,* 2010].

The shorter time lag of Southern Ocean response to ENSO related forcing suggests that the mechanism for eddy momentum release is relatively more efficient than

for SAM variability, and most likely due to the main direction of induced wind anomalies. A −SLPa induces northward current in the central Pacific sector, thus increasing its instability and likelihood to generate mesoscale rings.

Time series of mean SSH slope (ΔSSH) and baroclinic transport computed on the SR1 section at Drake Passage [*Swart et al.,* 2008b*; Cunningham and Pavic,* 2007*; Rintoul et al.,* 2000] show high-frequency and inter-annual variability. ΔSSH shows no linear trend and only a weak instantaneous response to SAM (r=0.27 with zero lag). These results point to a Southern Ocean in an eddy saturated state.

Although above 99% significance level, only weak cross-correlations (−0.20) were estimated between monthly ΔSSH with the SAM index with 23-month lag as well as with ENSO (0.24) with 22-month lag. These correlations are slightly higher for the 1-yr low pass filtered time-series than for the monthly time-series, but statistically insignificant. A positive SST/SSH anomaly localized within the central Pacific sector during a strong El Niño, propagated eastward with the ACC and about 2 years later arrived at Drake Passage. The opposite response was inferred from a +SAM anomaly, when decreased tilting of isopycnals associated with smaller transport was found about two years after a positive SAM event. A significant correlation between sea level slope and climate modes suggests that the Pacific sector, including Drake Passage, is buoyancy-dominated.

Specific regions of the Southern Ocean show more frequent energetic rings transporting heat, salt, and nutrients across the ACC domain. Warm anticyclones generated at the ARC are incorporated into the ACC domain downstream of the KP,

where they contribute to the observed three decades of warming (0.5°C) between 60°W and 150°W. Other sectors of the Southern Ocean reveal only negligible cooling responses, e.g. −0.01°C over thirty years. Therefore enhanced eddy poleward heat transport by warm subtropical rings outpaces the initial cooling response to SAM within the Indian sector.

REFERENCES

Alory, G., S. Wijffels, and G. Meyers (2007), Observed temperature trends in the Indian Ocean over 1960–1999 and associated mechanisms, *Geophys. Res. Lett., 34*, L02606, doi:10.1029/2006GL028044.

Ansorge, I. J., and J. R. E. Lutjeharms (2003), Eddies originating at the South-West Indian Ridge, *J. Mar. Sys., 39*, 1−18.

Aoki, S., M. Yoritaka, and A. Masuyama (2003), Multidecadal warming of subsurface temperature in the Indian sector of the Southern Ocean, *J. Geophys. Res., 108*(C4), 8081, doi:10.1029/2000JC000307.

Aoki, S., N. L. Bindoff, and J. A. Church (2005), Interdecadal water mass changes in the Southern Ocean between 30 degrees E and 160 degrees E, *Geophy. Res. Lett.*, *32*(7), doi:10.1029/ 2000JC000307.

Arblaster, J. M., and G. A. Meehl (2006), Contributions of external forcings to Southern Annular Mode trends, *J. Climate, 19*, 2896−2905.

AVISO (2009), SSALTO/DUACS user handbook: (M)SLA and (M)ADT near-real time and delayed time products, Iss 1:10, CLS-DOS-NT-06.034, 1−34.

Barré, N., C. Provost, A. Renault, and N. Sennéchael (2011), Fronts, meanders and eddies in Drake Passage during the ANT-XXIII/3 cruise in January– February 2006: A satellite perspective, *Deep-Sea Res. II*, doi:10.1016/j.dsr2.2011.01.003.

Beal, L. M., W. P. M. de Reijter, A. Biastoch, R. Zahn, and SCOR/WCRP/IAPSO Working Group (2011), On the role of the Agulhas system in ocean circulation and climate, *Nature, 472*(7344), 429–436.

Belkin, I. M., and A. L. Gordon (1996), Southern Ocean fronts from the Greenwich Meridian to Tasmania, *J. Geophys. Res*., 101, 3675−3696, doi:10.1029/95JC02750.

Billany, W., S. Swart, J. Hermes, and C. J. C. Reason (2010), Variability of the Southern Ocean fronts at the Greenwich Meridian, *J. Mar. Sys., 82*, 304−310.

Biastoch, A., C. W. Böning, F. U. Schwarzkopf, and J. R. E. Lutjeharms (2009), Increase in Agulhas leakage due to poleward shift of Southern Hemisphere westerlies, *Nature*, *462*(7272), 495−498, doi:101038/nature08519.

Boehme, L., M. P. Meredith, S. E. Thorpe, M. Biuw, and M. Fedak (2008), Antarctic Circumpolar Current frontal system in the South Atlantic: Monitoring using merged Argo and animal-borne sensor data, *J. Geophys. Res.*, *113*(C9), doi:10.1029/2007JC004647.

Böning, C. W., A. Dispert, M. Visbeck, S. R. Rintoul, and F. U. Schwarzkopf (2008), The response of the Antarctic Circumpolar Current to recent climate change, *Nat. Geosci.*, *1*(12), 864−869, doi:10.1038/ngeo362.

Bower, A. S., H. T. Rossby, and J. L. Lillibridge (1985), The Gulf Stream-barrier or blender?, *J. Phys. Oceanogr.*, *15*, 24−32.

Bretherton, C. S., M. Widmann, V. P. Dymnidov, J. M. Wallace, and I. Blade (1999), The effective number of spatial degrees of freedom of a time-varying field, *J. Climate, 12*, 1990−2009.

Bromwich, D. H., and R. L. Fogt (2004), Strong trends in the skill of the ERA-40 and NCEP-NCAR reanalyses in the high and middle latitudes of the Southern Hemisphere, 1958−2001. *J. Climate*, 17, 4603−4619.

Budillon, G., and S. R. Rintoul (2003), Fronts and upper ocean thermal variability south of New Zealand, *Antarctic Sci., 15*(1), doi:10.1017/S0954102002.

Chambers, D. P., B. D. Tapley, and R. H. Stewart (1997), Long-period ocean heat storage rates and basin-scale heat fluxes from TOPEX, *J. Geophys. Res.*, *102*(C5), 10525−10533.

Chelton, D. B., M. S. Schlax, and R. M. Samelson (2011), Global observations of nonlinear mesoscale eddies, *Prog. Oceanogr., 91*, 167−216.

Chereskin, T. K., K. A. Donohue, D. R. Watts, K. L. Tracey, Y. L. Firing, and A. L. Cutting (2009), Strong bottom currents and cyclongenesis in Drake Passage, *Geophys. Res. Lett.*, *36*, doi:10.1029/2009GL040940.

Cunningham, S. A., S. G. Alderson, B. A. King, and M. A. Brandon (2003), Transport and variability of the Antarctic Circumpolar Current in Drake Passage, *J. Geophys. Res.*, *108*(C5).

Cunningham, S., and M. Pavic (2007), Surface geostrophic currents across the Antarctic circumpolar current in Drake Passage from 1992 to 2004, *Prog. Oceanogr.*, *73*(3−4), 296−310.

Deacon, G. E. R. (1937), The hydrology of the Southern Ocean, *Discov. Rep., 15*, 1−24.

de Ruijter, W. P. M., A. Biastoch, S. S. Drijfhout, J. R. E. Lutjeharms, R. P. Matano, T. Pichevin, P. J. van Leeuwen, and W. Weijer (1999), Indian-Atlantic interocean exchange: Dynamics, estimation and impact, *J. Geophys. Res.*, *104*, 20,885–20,910, doi:10.1029/1998JC900099.

Ding Q., E. J. Steig, D. S. Battisti, and J. M. Wallace (2012), Influence of the tropics on the Southern Annular Mode, *J. Climate*, doi: 10.1175/JCLI-D-11-00523.1, in press.

Dong, S. F., J. Sprintall, and S. T. Gille (2006), Location of the antarctic polar front from AMSR-E satellite sea surface temperature measurements, *J. Phys. Oceanogr.*, *36*(11), 2075−2089.

Ducet, N., and P. Y. Le Traon (2001), A comparison of surface eddy kinetic energy and Reynolds stresses in the Gulf Stream and the Kuroshio Current systems from merged TOPEX/Poseidon and ERS-1/2 altimetric data, *J. Geophys. Res.*, *106*(C8), 16603−16622.

Farneti, R. and T. S. Delworth (2010), The role of mesoscale eddies in the remote oceanic response to altered Southern Hemisphere winds, *J. Phys. Oceanogr., 40*, 2348−2354, doi: 10.1175/2010JPO4480.1.

Fogt, R. L., and D. H. Bromwich (2006), Decadal variability of the ENSO teleconnection to the high-latitude South Pacific governed by coupling with the Southern Annular Mode, *J. Climate, 19*, 979−997.

Fogt, R. L., D. H. Bromwich, and K. M. Hines (2011), Understanding the SAM influence on the South Pacific ENSO teleconnection, *Clim. Dyn., 36*, 1555−1576, doi:10.1007/s00382-010-0905-0.

Fu, L.-U (2006), Pathways of eddies in the South Atlantic Ocean revealed from satellite altimeter observations, *Geophys. Res. Lett., 33* (L14610), doi:10.1029/2006GL026245.

Fukamachi, Y., S. R. Rintoul, J. A. Church, S. Aoki, S. Sokolov, M. A. Rosenberg, and M. Wakatsuchi (2010), Strong export of Antarctic Bottom Water east of the Kerguelen plateau, *Nat. Geosci., 3*, 327−331, doi:10.1038/ngeo842.

Fyfe, J. C., and O. A. Saenko (2005), Human-induced change in the Antarctic Circumpolar Current, *J. Climate*, *18*(15), 3068−3073.

Garabato, A. C. N, E. L. McDonagh, D. P. Stevens, K. J. Heywood, and R. J. Sanders (2002), On the export of Antarctic Bottom Water from the Weddell Sea, *Deep-Sea Res.*, *49*(21), 4715−4742.

Garabato, A. C. N., L. Jullion, D. P. Stevens, K. J. Heywood, and B. A. King (2009), Variability of Subantarctic Mode Water and Antarctic Intermediate Water in the

Drake Passage during the late-twentieth and early-twenty-first centuries, *J. Climate*, *22*(13), 3661−3688.

Garabato, A. C. N., R. Ferrari, and K. L. Polzin (2011), Eddy stirring in the Southern Ocean, *J. Geophys. Res.*, *116*(C09019), doi:10.1029/2010JC006818.

Gent, P. G., G. Danabasoglu, L. J. Donner, M. M. Holland, E. C. Hunke, S. R. Jayne, D. M. Lawrence, R. B. Neale, P. J. Rasch, M. Vertenstein, P. B. Neale, Z. -L. Yang, and M. Zhang (2011), The community climate system model version 4, *J. Climate, 24*, 4973−4991, doi:10.1175/2011JCLI4083.1.

Gille, S. T. (1994), Mean sea surface height of the Antarctic Circumpolar Currnt from Geosat data: Method and application, *J. Geophys. Res., 99*, 18255−18273.

Gille, S. T. (2002), Warming of the Southern Ocean since the 1950s, *Science*, *295*(5558), 1275−1277.

Gille, S. T. (2008), Decadal-scale temperature trends in the Southern Hemisphere ocean, *J. Climate*, *21*(18), 4749−4765.

Gong, D. Y., and S. W. Wang (1999), Definition of Antarctic Oscillation index, *Geophys. Res. Lett.*, *26*, 459–462.

Gordon, A. L. (1975), An Antarctic oceanographic section along 170°E, *Deep-Sea Res.*, 22, 357−377.

Gordon, A. L., E. Molinelli, and T. Baker (1978), Large-scale relative dynamic topography of the Southern Ocean, *J. Geophys. Res., 83*, 3023−3032.

Gordon, A. L., B. Huber, D. McKee, and M. Visbeck (2010), A seasonal cycle in the export of bottom water from the Weddell Sea, *Nature*, DOI:10.1038/NGEO916.

Grinsted, A., J. C. Moore, and S. Jevrejeva (2004), Application of the cross wavelet transform and wavelet coherence to geophysical time series, *Nonlinear Processes Geophys.*, 11, 561–566.

Grodsky, S. A., R. Lumplin, and J. A. Carton (2011), Spurious trends in global surface drifter currents, *Geophy. Res. Lett., 38*, doi:10.1029/2011GL047393.

Hall, A., and M. Visbeck (2002), Synchronous variability in the southern hemisphere atmosphere, sea ice, and ocean resulting from the annular mode, *J. Climate*, *15*(21), 3043−3057.

Hallberg, R., and A. Gnanadesikan (2006), The role of eddies in determining the structure and response of the wind-driven Southern Hemisphere overturing: results from the modeling eddies in the Southern Ocean (MESO) project, *J. Phys. Oceanogr., 36*, 2232−2252.

Hogg, A. M., and J. R. Blundell (2006), Interdecadal variability of the Southern Ocean, *J. Phys. Oceanogr., 36*, 1626−1645.

Hogg, A. M., M. P. Meredith, J. R. Blundell, and C. Wilson (2008), Eddy heat flux in the Southern Ocean: response to variable wind forcing, J. Climate, 21, 608−620, doi: 10.1175/2007JCLI1925.1

Hughes, C. W., M. P. Meredith, and K. Heywood (1999), Wind-driven transport fluctuations through Drake Passage: A Southern Mode, *J. Phys. Oceanogr. 29*(8), 1971–1992.

Jones, J. M., and M.Widmann (2004), Early peak in Antarctic oscillation index, *Nature, 481*, 290−291.

Jones, J. M., R. L. Fogt, M. Widmann, G. J. Marshall, P. D. Jones, and M. Visbeck (2009), Historical SAM variability. Part I: Century-length seasonal reconstructions, *J. Climate, 22*, 5319–5345, doi:10.1175/2009JCLI2785.1.

Joyce, T. M., S. L. Patterson, and R. C. Millard Jr. (1981), Anatomy of a cyclonic ring in the Drake Passage, *Deep-Sea Res.*, *28A(11)*, 1265−1287.

Karpechko, A. Y., N. P. Gillett, G. J. Marshall, and J. A. Screen (2009), Climate impacts of the Southern annular mode simulated by the CMIP3 models, *J. Climate*, *22*(13), 3751−3768.

Kwok, R., and J. C. Comiso (2002), Spatial patterns of variability in Antarctic surface temperature: connections to the Southern Hemisphere Annular Mode and the Southern Oscillation, Geophy. Res. Lett., 29(14), doi: 10.1029/2002GL015415.

Lee, S.-K, W. Park, E. van Sebille, M. O. Baringer, C. Wang, D. B. Enfield, S. G. Yeager, and B. P. Kirtman (2011), What caused the significant increase in Atlantic Ocean heat content since the mid-20th century?, *Geophy. Res. Lett., 38,* doi:10.1029/2011GL048856.

Lenn, Y. D., T. K. Chereskin, J. Sprintall, and E. Firing (2007), Mean jets, mesoscale variability and eddy momentum fluxes in the surface layer of the Antarctic Circumpolar Currnt in Drake Passage, *J. Mar. Res., 65*, 27−58.

Lenn, Y. D., T. K. Chereskin, and J. Sprintall (2008), Improving estimates of the Antarctic Circumpolar Current streamlines in Drake Passage, *J. Phys. Oceanogr.*, *38*(5), 1000−1010.

L'Heureux, M., and D. W. J. Thompson (2006), Observed relationships between the El Niño–Southern Oscillation and the extratropical zonal-mean circulation, *J. Climate, 19*, 276−287.

Liu, J., and J. A. Curry (2010), Accelerated warming of the Southern Ocean and its impacts on the hydrological cycle and sea ice, Proc. *Nat. Acad. Sci.*, doi: 10.1073/pnas.1003336107.

Lutjeharms, J. R. E., and I. J. Ansorge (2001), The Agulhas Return Current, *J. Mar. Sys., 30*, 115−138.

McCartney, M. S. (1976), The interaction of zonal currents with topography with applications to the Southern Ocean, *Deep-See Res.*, 23, 413−427.

Marshall, G. J. (2003), Trends in the Southern Annular Mode from observations and reanalyses, *J. Climate*, 16, 4134−4143.

Marshall, G. J., P. A. Stott, J. Turner, W. M. Connolley, J. C. King, T. A. Lachlan-Cope (2004), Causes of exceptional atmospheric circulation changes in the Southern Hemisphere, *Geophys. Res. Lett.*, *31*, doi:10.1029/2004GL019952.

Matano, R. P, G. G. Simionato, W. P. de Ruijter, P. J. van Leeuween, P. T. Strub, D. B. Chelton, and M. G. Schlax (1998), Seasonal variability in the Agulhas Retroflection region, *Geophys. Res. Lett., 25*, 4361−4364.

Meredith, M. P., J. L. Watkins, E. J. Murphy, N. J. Cunningham, A. G. Wood, R. Korb, M. J. Whitehouse, S. E. Thorpe, and F. Vivier (2003), An anticyclonic circulation above the Northwest Georgia Rise, Southern Ocean, *Geophys. Res. Lett., 30(20)*, 2061, doi:10.1029/2003GL018039

Meredith, M. P., P. L. Woodworth, C. W. Hughes, and V. Stepanov (2004), Changes in the ocean transport through Drake Passage during the 1980s and 1990s, forced by changes in the Southern Annular Mode, *Geophy. Res. Lett.*, *31*(21), doi:10.1029/2004GL021169.

Meredith, M. P., and A. M. Hogg (2006), Circumpolar response of Southern Ocean eddy activity to a change in the Southern Annular Mode, *Geophy. Res. Lett.*, *33*(16), doi:10.1029/2006GL026499.

Meredith, M. P., A. C. N. Garabato, A. L. Gordon, and G. C. Johnson (2008), Evolution of the deep and bottom waters of the Scotia Sea, Southern Ocean, during 1995−2005, *J. Climate*, *21*(13), 3327−3343.

Miranda, A. P., and B. Barnier (1999), On the dynamics of the Zapiola Anticyclone, *J. Geophy. Res., 104*, 21,137−21,149.

Moore, J. K., M. R. Abbott, and J. G. Richman (1997), Variability in the location of the Antarctic polar front (90°−20°W) from satellite sea surface temperature data, *J. Geophy. Res.*, *102*, 27825−27833.

Moore, J. K., M. R. Abbott, and J. G. Richman (1999), Location and dynamics of the Antarctic polar front from satellite sea surface temperature data, *J. Geophys. Res., 104*, 3059−3073.

Moore, J. C., A. Grinsted, and S. Jevrejeva (2005), New Tools for analyszing time series relationships and trends, *EOS*, *86*(24), 226−232.

Morrow, R., J. Church, R. Coleman, D. Chelton, and N. White (1992), Eddy momuntum flux and its contrinbution to the Southern Ocean momentum balance, *Nature, 357*, 482−484.

Morrow, R., and F. Birol (2004), Divergent pathways of cyclonic and anti-cyclonic ocean eddies, *Geophys. Res. Lett., 31*(L24311), doi:10.1029/2004GL020974.

Morrow, R., G. Valladeau, and J. B. Sallée (2008), Observed subsurface signature of Southern Ocean sea level rise, *Prog. Oceanogr.*, *77*(4), 351−366.

Morrow, R., M. L. Ward, A. M. Hogg, and S. Pasquet (2010), Eddy response to Southern Ocean climate modes, *J. Geophys. Res., 115*(C10030), doi:10.1029/2009JC005894.

Nowlin, W. D., J., T. Whitworth III, and R. D. Pilsbury (1977), Structure and transport of the Antarctic Circumpoalr Current at Drake Passage from short-term measurements, *J. Phys. Oceanogr., 7*, 788−802.

Nowlin, W. D. Jr., and M. Clifford (1982), The kinematic and thermohaline zonation of the Antarctic Circumpolar Current at Drake Passage, *J. Mar. Res*., *40*, 481−507.

Orsi, A. H., T. Whitworth III, and W. D. Nowlin Jr. (1995), On the Meridional Extent and Fronts of the Antarctic Circumpolar Current, *Deep-Sea Res.*, *42*(5), 641−673.

Orsi, A. H., G. C. Johnson, and J. L. Bullister (1999), Circulation, mixing, and production of Antarctic Bottom Water, *Prog. Oceanogr., 43*, 55−109.

Park, J. J., K. Kim,, B. A. King, and S. C. Riser (2005), An advanced method to estimate deep currents from profiling floats, *J. Atmos. Ocean. Technol., 22*, 1294–1304.

Park, Y.-H, F. Vivier, F. Roquet, and E. Kestenare (2009), Direct observations of the ACC transport across the Kerguelen Platea, *Geophys. Res. Lett*., *36*(L18603), doi:10.1029/2009GL039617.

Peterson, R. G., and T. Whitworth III (1989), The Subantarctic and Polar Fronts in relation to deep water masses through the Southwestern Atlantic, *J. Geophys. Res., 15*, 10,817−10,838.

Reynolds, R. W., T. M. Smith, C. Liu, D. B. Chelton, K. S. Casey, and M. G. Schlax (2007), Daily high-resolution blended analyses for sea surface temperature, *J. Climate*, *20*, 5473−5496, doi: 10.1175/2007JCLI1824.1.

Ridgway, K. R., J. R. Dunn, and J. L. Wilkin (2007), Observational evidence for a Southern Hemisphere oceanic supergyre, *Geophy. Res. Lett.*, *34*, L13612, doi:10.1029/2007GL030392.

Rintoul, S. R., and S. Sokolov (2001), Baroclinic transport variability of the Antarctic Circumpolar Current south of Australia (WOCE repeat section SR3), *J. Geophys. Res., 106*, 2795–2814.

Rintoul, S. R., S. Sokolov, and J. Church (2002), A 6 year record of baroclinic transport variability of the Antarctic Circumpolar Current at 140°E derived from expendable bathythermograph and altimeter measurements, *J. Geophys. Res*., *107*(C10), 3155, doi:10.1029/2001JC000787.

Rintoul, S. R., S. Sokolov, and R. A. Massom (2008), Rapid development and persistence of a massive Antarctic sea ice tongue, *J. Geophys. Res.*, *113*, C07045, doi:10.1029/2007JC004541.

Rio, M.-H., P. Schaeffer, G. Moreaux, J.-M. Lemoine, and E. Bronner (2009), A new mean dynamic topography computed over the global ocean from GRACE data, altimetry and in-situ measurements, *OceanObs09*, 21−25.

Rodman, M. R., and A. L. Gordon (1982), Southern Ocean bottom water of the Australian-New Zealand sector, *J. Geophys. Res., 87*(C8), 5771−5778.

Roquet, F., Y.-H Park, C. Guinet, F. Bailleul, and J.-B. Charrassin (2009), Observations of the Fawn Trough Current over the Kerguelen Plateau from instrumented elephant seals, *J. Mar. Sys., 78,* 377−393, doi:10.1016/j.jmarsys.2008.11.017.

Rouault, M., P. Penven, and B. Pohl (2009), Warming in the Agulhas Current system since the 1980's, *Geophy. Res. Lett., 36,* doi:10.1029/2009GL037987.

Russell, J. L., K. W. Dixon, A. Gnanadesikan, R. J. Stouffer, and J. R. Toggweiler (2006), The Southern Hemisphere westerlies in a warming world: Propping open the door to the deep ocean, *J. Climate, 19*, 6382 – 6390.

Saenko, O. A., J. C. Fyfe, and M. H. England (2005), On the response of the oceanic wind-driven circulation to atmospheric CO2 increase, *Clim. Dynam.*, *25*(4), 415−426.

Sallée, J. B., N. Wienders, K. Speer, and R. Morrow (2006), Formation of subantarctic mode water in the southeastern Indian Ocean, *Ocean Dynam.*, *56*, 525−542, doi:10.1007/s10236-005-0054-x.

Sallée, J. B., K. Speer, and R. Morrow (2008), Response of the Antarctic Circumpolar Current to atmospheric variability, *J. Climate*, *21*(12), 3020−3039.

Sallée, J. B., K. Speer, and S. R. Rintoul (2010), Zonally asymmetric response of the Southern Ocean mixed-layer depth to the Southern Annular Mode, *Nat. Geosci., 3*, doi:10.1038/NGEO812.

Screen, J. A., N. P. Gillett, D. P. Stevens, G. J. Marshall, and H. K. Roscoe (2009), The Role of Eddies in the Southern Ocean Temperature Response to the Southern Annular Mode, *J. Climate*, *22*(3), 806−818.

Sen Gupta, A., and M. H. England (2006), Coupled ocean–atmosphere–ice response to variations in the Southern Annular Mode, *J. Climate, 19*(18), 4457–4486

Sloyan, B. M., and S. R. Rintoul (2001), The Southern Ocean limb of the global deep overturning circulation, *J. Phys. Oceanogr.*, *31*(1), 143−173.

Smith, W. H. F., and D. T. Sandwell (1997), Global seafloor topography from satellite altimetry and ship depth soundings, *Science*, *277*, 1957−1962.

Smith, C. A. and P. Sardeshmukh (2000), The effect of ENSO on the intraseasonal variance of surface temperature in winter, *Int. J. Climatol.*, *20*, 1543−1557.

Sokolov, S., and S. R. Rintoul (2002), Structure of Southern Ocean fronts at 140 degrees E, *J. Mar. Sys.*, *37*, 151−184.

Sokolov, S., and S. R. Rintoul (2007a), Multiple jets of the Antarctic circumpolar current South of Australia, *J. Phys. Oceanogr.*, *37*(5), 1394−1412.

Sokolov, S., and S. R. Rintoul (2007b), On the relationship between fronts of the Antarctic Circumpolar Current and surface chlorophyll concentrations in the Southern Ocean, *J. Geophys. Res., 112*(C07030), doi:10.1029/2006JC004072.

Sokolov, S., and S. R. Rintoul (2009a), Circumpolar structure and distribution of the Antarctic Circumpolar Current fronts: 1. Mean circumpolar paths, *J. Geophys. Res.*, *114*, doi:10.1029/2008JC005108.

Sokolov, S., and S. R. Rintoul (2009b), Circumpolar structure and distribution of the Antarctic Circumpolar Current fronts: 2. Variability and relationship to sea surface height, *J. Geophys. Res.*, *114*, doi:10.1029/2008JC005248.

Sparrow, M. D., K. J. Heywood, J. Brown, and D. P. Stevens (1996), Current structure of the south Indian Ocean*, J. Geophys. Res*., *101*, 6377−6391, doi:10.1029/95JC03750.

Spence, P., J. C. Fyfe, A. Montenegro, and A. J. Weaver (2010), Southern Ocean response to strengthening winds in an eddy-permitting global climate model, *J. Climate, 23*, 5332−5343, DOI: 10.1175/2010JCLI3098.1.

Speich, S., B. Blanke, and W. Cai (2007), Atlantic meridional overturning circulation and the Southern Hemisphere supergyre, *Geophy. Res. Lett.*, *34*(L23614), doi:10.1029/2007GL031583.

Sprintall, J. (2003), Subsurface structure of interannual temperature anomalies in the Australian sector of the Southern Ocean, *J. Geophys. Res., 108*(C9*)*, doi:10.1029/2002JC001494.

Sprintall, J. (2008), Long-term trends and interannual variability of temperature in Drake Passage, *Prog. Oceanogr., 77*, 316–330.

Stammerjohn, S. E., D. G. Martinson, R. C. Smith, X. Yuan, and D. Rind (2008), Trends in Antarctic annual sea ice retreat and advance and their relation to El Niño-Southern Oscillation and Southern Annular Mode variability, *J. Geophys. Res., 113*(C03S90), doi:10.1028/2007JC004269.

Sura, P., and S. T. Gille (2010), Stochastic dynamics of sea surface height variability, *J. Phys. Oceanogr*., *40*, 1582−1596.

Swart, N. C., I. J. Ansorge, and J. R. E. Lutijeharms (2008a), Detailed characterization of a cold Antarctic eddy, *J. Geophys. Res.,113*(C01009), doi:10.1029/2007JC004190.

Swart, S., S. Speich, I. J. Ansorge, G. J. Goni, S. Gladyshev, and J. R. E. Lutjeharms (2008b), Transport and variability of the Antarctic Circumpolar Current south of Africa, *J. Geophys. Res., 113(*C09014), doi:10.1029/2007JC004223.

Swart, S., S. Speich, I. J. Ansorge, and J. R. E. Lutjeharms (2010), An altimetry-based gravest empirical mode south of Africa: 1. Development and validation, *J. Geophys. Res.*, *115*, doi:10.1029/2009JC005299.

Swart, S., and S. Speich (2010), An altimetry-based gravest empirical mode south of Africa: 2. Dynamic nature of the Antarctic Circumpolar Current fronts, *J. Geophys. Res.*, *115*, doi:10.1029/2009JC005300.

Thompson, D. W. J., and J. M. Wallace (2000), Annular modes in the extratropical circulation. Part 1: Month-to-month variability, *J. Climate, 13*, 1000−1016.

Thompson, D. W. J., and S. Solomon (2002), Interpretation of recent Southern Hemisphere climate change, *Science*, *296*(5569), 895−899.

Thompson, D. W. J., S. Solomon, P. J. Kushner, M. H. England, K. M. Grise, and D. J. Karoly (2011), Signatures of the Antarctic ozone hole in the Southern Hemisphere surface climate change, *Nat. Geosci.*, doi:10.1038/NGEO1296.

Thorpe, S. E., K. J. Heywood, M. A. Brandon, and D. P. Stevens (2002), Variability of the southern Antarctic Circumpolar Current front north of South Georgia, *J. Mar. Syst., 37*, 87−105.

Tilburg, C. E., H. E. Hurlburt, J. J. O'Brien, and J. F. Shriver (2002), Remote topographic forcing of a baroclinic western boundary current: An explanation for the Southland Current and the pathway of the subtropical front east of New Zealand, *J. Phys. Oceanogr.*, *32*, 3216–3232.

Toggweiler, J. R., and J. Russell (2008), Ocean circulation in a warming climate, *Nature*, *451*(7176), 286−288.

Torrence, C., and G. P. Compo (1998), A practical guide to wavelet analysis, *Bull. Amer. Meteor. Soc., 79*, 61−78.

Torrence, C., and P. J. Webster (1999), Interdecadal changes in the ENSO-Monsoon system, *J. Climate, 12*, 2679−2690.

Trathan, P. N., M. A. Brandon, E. J. Murphy, and S. E. Thorpe (2000), Transport and structure within the Antarctic Circumpolar Current to the north of South Georgia, *Geophy. Res. Lett.*, *27*(12), 1727−1730.

Turner, J. (2004), The El Niño-Southern Oscillation and Antarctica, *Int. J. Climatol., 23*, 1−31, doi:10.1002/joc.965.

Uddstrom, M. L., and N. A. Oien (1999), On the use of high-resolution satellite data to describe the spatial and temporal variability of sea surface temperature in the New Zealand region, *J. Geophys. Res.*, *104*, 20729−20751.

Verdy, A., J. Marshall, and A. Czaja (2006), Sea surface temperature variability along the path of the Antarctic Circumpolar Current, *J. Phys. Oceanogr.*, 36, 1317–1331.

Volkov, D. L., and L. L. Fu (2008), The role of vorticity fluxes in the dynamics of the Zapiola Anticyclone, *J. Geophys. Res., 113*, doi:10.1029/2008JC004841.

Watts, D. R., C. Sun, and S. Rintoul (2001), A two-dimensional gravest empirical mode determined from hydrographic observations in the subantarctic front, *J. Phys. Oceanogr.*, *31*(8), 2186−2209.

Wilkin, J. L., and R. A. Morrow (1994), Eddy kinetic energy and momentum flux in the Southern Ocean: Comparisons of a global eddy-resolving model with altimeter, drifter and current-meter data. *J. Geophys. Res.*, *99*, 7903–7916.

Whitworth III, T., W. D. Nowlin Jr., R. D. Pillsbury, M. I. Moore, and R. F. Weiss (1991), observations of the Antarctic Circumpolar Current and deep boundary current in the Southwest Atlantic, *J. Geophys. Res., 96*(C8), 15105−15118.

Wu, L., W. Cai, L. Zhang, H. Nakamura, A. Timmermann, T. Joyce, M. J. McPhaden, M. Alexander, B. Qiu, M. Visbeck, P. Chang, and B. Giese (2012), Enhanced warming over the global subtropical western boundary currents, *Nat. Clim. Change*, *2*, 161−166, doi:10.1038/NCLIMATE1353.

Yang, X. Y., D. X. Wang, J. Wang, and R. X. Huang (2007), Connection between the decadal variality in the Southern Ocean circulation and the Southern Annular Mode, *Geophy. Res. Lett.*, *34*(16), doi:10.1029/2007GL030526.

Yuan, X., and D. G. Martinson (2000), Antarctic sea ice extent variability and its global connectivity, *J. Climate*, *13*, 1697−1717.

Yuan, X. (2004), ENSO-related impacts on Antarctic sea ice: a synthesis of phenomenon and mechanisms, *Antarct. Sci.*, *16*(4), 415−425.